

**SOLAR ELECTROLYZER COUPLING VIA LOAD-MATCHING
AND
DOPING IN CADMIUM TELLURIDE SOLAR CELLS
TO OVERCOME VOLTAGE LIMITATIONS**

by

Gowri Manasa Sriramagiri

A thesis submitted to the Faculty of the University of Delaware in partial fulfillment of the requirements for the degree of Doctor of Philosophy in Electrical and Computer Engineering

Winter 2019

© 2018 Gowri M. Sriramagiri
All Rights Reserved

**SOLAR ELECTROLYZER COUPLING VIA LOAD-MATCHING
AND
DOPING IN CADMIUM TELLURIDE SOLAR CELLS
TO OVERCOME VOLTAGE LIMITATIONS**

by

Gowri Manasa Sriramagiri

Approved: _____
Kenneth E. Barner, Ph.D.
Chair of the Department of Electrical and Computer Engineering

Approved: _____
Levi T. Thompson, Ph.D.
Dean of the College of Engineering

Approved: _____
Douglas J. Doren, Ph.D.
Interim Vice Provost for Graduate & Professional Education

I certify that I have read this dissertation and that in my opinion it meets the academic and professional standard required by the University as a dissertation for the degree of Doctor of Philosophy.

Approved: _____
Steven S. Hegedus, Ph.D.
Professor in charge of dissertation

I certify that I have read this dissertation and that in my opinion it meets the academic and professional standard required by the University as a dissertation for the degree of Doctor of Philosophy.

Approved: _____
Kevin D. Dobson, Ph.D.
Member of dissertation committee

I certify that I have read this dissertation and that in my opinion it meets the academic and professional standard required by the University as a dissertation for the degree of Doctor of Philosophy.

Approved: _____
Brian E. McCandless, B.S.
Member of dissertation committee

I certify that I have read this dissertation and that in my opinion it meets the academic and professional standard required by the University as a dissertation for the degree of Doctor of Philosophy.

Approved: _____
James S. Kolodzey, Ph.D.
Member of dissertation committee

I certify that I have read this dissertation and that in my opinion it meets the academic and professional standard required by the University as a dissertation for the degree of Doctor of Philosophy.

Approved: _____
Robert L. Opila, Ph.D.
Member of dissertation committee

ACKNOWLEDGMENTS

I owe my humblest gratitude to my advisor Prof. Steve Hegedus for believing in me, hiring me and encouraging my ideas and endeavors leading to the completion of this dissertation. The work comprised in this thesis would not have been possible without the continuous support and guidance of Dr. Kevin Dobson with every crucial task including experimentation to documentation. Working with a dynamic researcher like Brian McCandless was exciting as he offered a lot to learn - ranging fundamental theory to experimental technique. Thanks also to: my committee members: Prof. James Kolodzey, Prof. Bob Opila for providing me with excellent guidance and advice to improve the quality and content of this dissertation; to Chris Thompson for guiding me with the different aspects of device characterization and for the insightful discussions; to Prof. Robert Birkmire, Prof. Juejun Hu, Dr. Ujjwal Das, Prof. Feng Jiao and Prof. William Shafarman their guidance through the different projects that contributed to this dissertation. A special thanks to Dr. Kathy Ayers from ProtonOnsite[®] for her invaluable support in understanding practical aspects of H₂ electrolyzers and providing data for the modeling. The supporting staff Wayne Buchanan and Kevin Hart, and the administrative staff Sherry Stewart and Paula Newton deserve special thanks because without them day-to-day experiments and operations would not have been nearly as smooth and efficient.

On the personal front, everything I have achieved so far would not have been possible without the support, strength and motivation provided by my parents Venkateswara Rao & Padma Sreeramagiri who encouraged me to pursue science and to

have pushed me for academic excellence. My uncle Mahesh Kavaturu and my aunt Madhavi G. Kavaturu have provided an immense supply of support and inspiration and have guided me through everything from career choices to daily sustenance since my first day in the U.S., treating me as one of their own. Thanks especially to my husband Andrew Wright, who has been my backbone, bolstering me through the ups and downs of my academic and personal life on a daily basis, much of my achievements would not have been possible without his unparalleled encouragement. My friend Nupur Bhargava deserves special gratitude for being my role model and my trusted advisor with every decision, sharing my times of happiness and adversity. My brother Praveen Sreeramagiri, cousins Shriram and Shria Kavaturu, friends Srimoyee Dasgupta, Divya Vannala, Mounika Vendoti, Sunethra Thimmapuram, Rajeev Sathyanarayana, Madhu Adiki, Ramakanth Annam, and Esther & David Grund have all provided me with a family away from home.

Lastly, I would like to extend my thanks to all my fellow graduate students of IEC for having made it an exciting and friendly place to work: Nuha Ahmed and Mike Lloyd specifically for offering all that you have to teach and share - you have been great colleagues and amazing friends; Uwadiae Obahiagbon, Curtis Walkons, Sina Soltanmohammed, Lei Chen, Doug Bishop, Stella Liu, Lei Zhang, Nick Valdes, Austin Kuba, Alex Harding, Sergio Sepulveda and Brent Shu; and my friends from the dept. of ECE: Saptharshi Sinha for lending me his text books and his guidance even before my arrival at UD, Anagha Kulkarni, Anupama Puthur Venkataraman, Sherin Mathews, Abhishek Iyer and Anish Soman. Many thanks also to Wesley Luc from the dept. of Chemical and Biomolecular Engineering for being a patient and sporting partner in the solar fuel project.

None of this goes without thanking the funding agencies without whose financial capital the work comprised in this dissertation would not have been possible: the U.S. Dept. of Energy and the University of Delaware Energy Institute.

TABLE OF CONTENTS

LIST OF TABLES	xii
LIST OF FIGURES	xv
ABSTRACT	xxii

Chapter

1	INTRODUCTION: SOLAR FUELS AND CADMIUM TELLURIDE SOLAR CELL DOPING	1
1.1	Solar Fuels	1
1.1.1	Motivation	1
1.1.2	Device Architectures	3
1.1.3	Water and carbon dioxide electrolysis	5
1.1.4	Figure of Merit:	7
1.1.4.1	SFE of PV-EC devices	8
1.1.5	Literature Review	10
1.1.6	Thesis statement for PV-EC Aspect	11
1.2	Cadmium Telluride Solar Cells	13
1.2.1	Introduction to thin film CdTe Photovoltaics.....	13
1.2.1.1	History of CdTe Photovoltaics	13
1.2.1.2	CdTe Toxicity.....	14
1.2.2	Low cost manufacturability of CdTe modules:	15
1.2.3	Device Structure, Performance Metrics	16
1.2.4	Trend of increasing CdTe solar cell efficiencies	21
1.2.5	V _{OC} Enhancement.....	21
1.2.6	Thesis statement relating to CdTe doping:	26
1.2.7	Dissertation Outline.....	27
2	MODELING AND IMPLEMENTATION OF LARGE-AREA CARBON DIOXIDE PV-EC	29
2.1	Description of Jiao Group's CO ₂ Electrolyzer	30
2.2	Designing the Photovoltaic Power Source	31
2.3	Solar Simulator Construction for Illumination Source.....	32
2.4	System Operation	33

2.5	System Design	34
2.6	Using Modeling to Determine Solar Array Configuration	38
2.6.1	PV configuration with 6 or more cells in series	44
2.7	Measured PV-EC Performance	46
2.8	Comparing Calculated and Measured Results:.....	52
2.9	Summary of Proposed Optimization Procedure:.....	55
2.10	Potential for High SFE's with Multijunction Tandem Solar Cells Under Concentration:	56
3	ANNUAL GENERATION MODEL FOR SOLAR ELECTROLYZER FIELD PERFORMANCE, APPLICATION TO CO ₂ PV-EC	59
3.1	Figure of Merit for Practical Consideration of PV-EC's:	60
3.2	Power Conditioning Devices as a Coupling Strategy.....	60
3.3	Model Development	63
3.3.1	Annual generation model- parameters incorporated	63
3.4	Annual Generation Model for Lab-Scale PV-EC.....	68
3.5	Summary.....	72
4	APPLICATION OF YEARLY MODEL TO A CONJECTURAL H ₂ O PV- EC	73
4.1	Advantage of Indirect Coupling in <i>Sub-Optimally</i> Matched PV-EC's ...	80
4.2	Incorporating Series Resistance Losses.....	83
4.3	Summary.....	86
5	ANTIMONY-DOPED CADMIUM TELLURIDE SOLAR CELLS.....	89
5.1	Sb as the Dopant of Choice	89
5.2	Fabrication Sequence of Diagnostic CdTe:Sb Devices.....	91
5.2.1	Window (front contact) layer stack deposition	92
5.2.2	Chemical bath deposition of CdS	92
5.2.3	CdTe:Sb Growth by Vapor Transport Deposition (VTD).....	93
5.2.3.1	Dopant incorporation in VTD-deposited films.....	94
5.3	Annealing Treatments	95
5.3.1	Cd-vapor anneal to facilitate Sb incorporation in CdTe lattice ...	96
5.3.2	Device anneal treatment to improve overall device behavior	97

5.3.3	Back (p-type) contact deposition.....	98
5.3.4	Front (n-Type) Contact Deposition:	99
5.3.5	Variability in similar devices.....	100
5.4	Applied Device Model	101
5.5	Suite of Device Measurement Techniques Used.....	103
5.5.1	JV measurement	103
5.5.2	Capacitance-Voltage Sweep	103
5.5.2.1	Limitation to capacitance measurement	104
5.5.3	Admittance Spectroscopy	106
5.5.4	JV(T).....	109
5.5.4.1	JV(T) Light.....	110
5.5.4.2	JV(T) Dark.....	111
5.5.5	Quantum efficiency:	114
5.5.6	JV(Illumination-G)/ Suns V_{OC} :	115
5.6	Summary.....	117
6	ANALYSIS OF ANTIMONY-DOPED DEVICES AND EVALUATING DEVICE TREATMENT TECHNIQUES	118
6.1	Evaluation of Devices from Anneal Matrix with JV and CV Measurements.....	121
6.1.1	Interpreting results from device measurements.....	125
6.1.1.1	Effect of Cd-vapor treatment.....	126
6.1.1.2	Effect of O_2 in the device anneal ambient	126
6.1.1.3	Effect of $CdCl_2$ in device anneal ambient	127
6.1.1.4	A combination of $CdCl_2$ and O_2 in the ambient	127
6.2	Quantitative Analysis of Performance Deficit	128
6.2.1	J_{SC} losses.....	128
6.2.2	V_{OC} losses	129
6.2.2.1	V_{OC} deficit as a function of defect density	132
6.2.3	Blocking contact and its effect on FF deficit.....	134
6.2.4	Performance estimation of extrinsically doped solar cells	137

6.3	Best Sb-Doped Device Processed at IEC	138
6.4	Discussion and Summary	140
7	CONCLUSION AND FUTURE WORK.....	142
7.1	Decoupled PV-EC Architecture for Efficiency and Practicality	142
7.1.1	Conclusion of experimental and simulation results.....	142
7.1.2	Future work	143
7.2	Sb-doped CdTe Photovoltaics for Increased Voltage Output	144
7.2.1	Summary of results from device analysis.....	144
7.2.2	Future work	145
	REFERENCES	148
	Appendix	
A	DERIVATION OF V_{OC} DEPENDENCE ON DOPING USING CURRENT CONTINUITY EQUATIONS.....	151
A.1	Current transport model for CdTe devices of this study	151
A.1	Derivation of light-generated current for a semi-infinite absorber case	152
A.2	Dark saturation current	154
A.3	Derivation of V_{OC}	154
B	A DETAILED DESCRIPTION OF PV-EC LOAD-MATCHING MODEL ...	155
B.1	Model Input	155
B.2	Model Output.....	155
B.3	Model assumptions.....	156
B.4	Model Algorithm	156
B.4.1	Load-matching for large-scale PV-EC systems	157
B.5	Load-Matching for Small-Scale PV-EC's.....	158
B.5.1	Correcting for parasitic resistances:	160
A.4	Implementing Load-Matching Model Using <i>Origin</i> [®] Analysis Template	161
C	A DETAILED DESCRIPTION OF PV-EC ANNUAL GENERATION MODEL.....	167

C.1	Model Input	167
C.2	Model Output.....	167
C.3	Model Assumptions.....	168
C.4	Computing PV Array Output Using PV ‘Translation’ Equations	168
C.5	Incorporating Wiring Resistance	170
C.6	Calculating PV-EC Operating Point.....	170
	C.6.1 Direct coupling	170
	C.6.2 DC power optimizer coupling	171
	C.6.3 Inverter Coupling.....	171
C.7	Implementing Annual Generation Model for Direct-, Power Optimizer- and Inverter- Coupling Using <i>Origin</i> [®]	173
D	COPYRIGHT FOR PREVIOUSLY PUBLISHED MATERIAL	186
	D.1 MRS Advances copyright form pertaining to the article in ref. [59]: ...	187
	D.2 ACS Sustainable Chemistry and Engineering Copyright form for the article in ref. [60]:.....	188
	D.3 Sustainable Energy and Fuels permissions note pertaining to article in ref. [61]:.....	189

LIST OF TABLES

Table 2-1: Results from modeling 5-cell configuration PV array. The values in red highlight the configuration giving best predicted SFE: J'_{OP} is the operating current density of individual cells	43
Table 2-2: Experimental matrix involving solar cell illumination areas	48
Table 2-3: Summary of experimental results, V_{PV} is the voltage at the PV module, V_{EC} is the voltage at the electrolyzer, ΔV is the difference between the PV voltage and the electrolyzer voltage, R is the resistance calculated from the differences in voltage between PV and electrolyzer/ operating current I_{OP} , J'_{OP} is the operating current density <i>per cell</i> and J_{OP} is the overall operating current density and actual value used in calculating SFE, $CO FE$ is FE of the reaction	50
Table 2-4: Average values of SFE predicted from modeling when corrected for measured parasitic circuit resistive losses. $\Delta SFE(\%abs)$ is the difference between the modeled and predicted SFE given in absolute percentage points, $\Delta SFE (\% rel.)$ is the same parameter gives as a relative percentage.....	55
Table 2-5: SFE's calculated for a PV-EC designed using the flow cell electrolyzer discussed in this work with high efficiency multijunction tandem cells under 42x concentration, as reported in reference [3].....	57
Table 3-1: Final numerical results from annual model calculations for lab-scale CO_2 PV-EC device with demonstrated 7.6% SFE at STC. H_2 production calculated as competing reaction during CO_2 electrolysis....	71
Table 4-1: Electrolyzer and solar module electrical specifications required for PV-EC design	74
Table 4-2: Tabulated annual results from hydrogen generation model applied to 2.1 MW H_2O PV-EC for different coupling strategies: optimally matched direct coupling-1, power optimizer coupling with 100% coupling efficiency, DC-AC-DC coupling with 95% DC-AC conversion efficiency	79
Table 4-3: Solar array layout and electrical specifications for the two directly coupled PV-EC configurations.....	81

Table 4-4: Tabulated annual results from hydrogen generation model applied to 2.1 MW H ₂ O PV-EC for ‘Direct Coupling-2’, compared with those of ‘Direct Coupling-1’, power optimizer coupling with 100% power conversion efficiency, and DC-AC-DC coupling with 95% DC-AC conversion efficiency, reproduced here from Table 4-2 for comparison.	82
Table 4-5: Tabulated calculation showing wiring design and wiring loss estimation for directly-connected PV-EC	85
Table 4-6: Tabulated results from the annual generation model for 2 MW H ₂ O electrolysis system.....	86
Table 5-1: JV and CV parameters of devices made on a VTD-grown CdTe:Sb coupon (shown in the photograph of Figure 5-8) to demonstrate variability in devices studied in this work. From the table on that right, it is apparent that the maximum variability is seen in the device J _{SC} by ~10% error.....	101
Table 6-1: Expected benefits from post-deposition treatments	120
Table 6-2: The anneal matrix used to evaluate the effect of CdCl ₂ and Air in the anneal ambient on CdTe:Sb diagnostic devices.	120
Table 6-3: JV and CV Parameters of devices from the anneal matrix. Voc, Jsc, FF and η are from illuminated JV measurements at STC. N _{CV} is obtained from CV measurements at 0.5 MHz.....	123
Table 6-4: Schottky barrier potentials of the rear CdTe:Sb/C contacts extracted for all the devices in the anneal matrix from JV(T)- <i>Dark</i> measurements, compared with the activation energies of charge response extracted from their admittance spectroscopy measurements.....	135
Table 6-5: FF limit calculated as a function of Voc, assuming no blocking contact, series or shunt resistances.....	137
Table 6-6: JV parameters of the best Sb-doped device as measured (‘Air+CdCl ₂ coat’), compared to hypothetical devices: one with improved τ _n = 10 ns, and another with N _{CV} =[Sb]=5x10 ¹⁶ cm ⁻³ , to demonstrate the potential of efficiency gain from successful extrinsic doping in CdTe.	138

Table B-1: A tabulated account of the *Origin*[®] template used to implement the load matching model for a PV-EC combination. The *Origin*[®] columns are transposed here as the table rows, along with information about its contents: the parameter, its units, the function used to perform operations. Comments given here provide a more detailed description of the parameter, and the equation column provides the corresponding equation pertaining to the *Origin*[®] function used, where applicable 163

Table .C-1: A tabulated account of the *Origin*[®] template used to implement the annual generation model for a PV-EC combination with direct-, dc power optimizer-, and inverter-coupling. The *Origin*[®] columns are transposed here as the table rows, and information about its contents are given as adjacent table columns. The ‘parameter’ column gives the name of the variable, the ‘units’ column gives the respective units, the ‘function’ column shows the exact function as used in the *Origin*[®] template to perform respective column operations. Comments given here provide a more detailed description of the parameter, and the equation column provides the corresponding equation pertaining to the *Origin*[®] function used, where applicable..... 174

LIST OF FIGURES

Figure 1-1:	Energy densities for different storage mechanisms- note that the horizontal axis is shown in log scale	3
Figure 1-2:	Schematic depicting (a) an integrated photoelectrochemical cell (PEC) device architecture where the photoactive component is immersed in the electrolyte and (b) a decoupled PV-EC device architecture with an independently designed photovoltaic device powering an independently designed electrochemical cell.	4
Figure 1-3:	Block diagram of a PV-EC to illustrate derivation of its SFE	9
Figure 1-4:	Device architecture of a state-of-the-art superstrate CdTe solar cell	16
Figure 1-5:	Equivalent circuit diagram of a CdTe solar cell under illumination, with the pn junction between the emitter CdS and the absorber CdTe is given on the right as the primary diode on the left and the blocking contact is depicted as Schottky contact diode on the right.....	18
Figure 1-6:	(a) Current density vs. voltage curves for a solar cell in dark and under illumination with voltage bias sweep (b) current-density and power vs. voltage curve of a solar cell under illumination in source configuration, showing the peaking of the output power and the maximum power points (MPP)	19
Figure 1-7:	Chronological record of thin-film CdTe solar cell record efficiency device parameters, compared with the theoretical Shockley-Queisser (S-Q) limit as a function of the bandgap of the corresponding absorber (shown as a dashed line in each of the plots). The yellow point shown in the V_{OC} graph is the V_{OC} possible with $5 \times 10^{16} \text{ cm}^{-3}$ doping. The theoretical limits for the η , J_{SC} , and V_{OC} of the latest record efficiency device (reported in 2016) are different since its absorber ($\text{CdTe}_x\text{Se}_{1-x}$) has a slightly lower bandgap (E_g) of $\sim 1.42 \text{ eV}$, compared to the previous devices whose CdTe absorbers have $\sim 1.45 \text{ eV}$. The corresponding disparity in absorber bandgap does not account for a considerable disparity in device FF is comparatively small.....	23
Figure 2-1:	Schematic of integrated photovoltaic and CO_2 electrochemical setup. I_{OP} and V_{OP} measurement meters not shown.....	30
Figure 2-2:	Measured I-V curves of c-Si solar cells under OAI [®] solar simulator at IEC.....	31

Figure 2-3: A picture of the large-area solar simulator constructed for illuminating the solar array from the bottom. The halogen light bulbs on the top are calibrated to provide 1000 W/m^2 light intensity. The fan on the right is used to cool the samples down to 25°C operating temperature..... 33

Figure 2-4: Linear voltammogram of the CO_2 electrolyzer, data measured and provided by Wesley Luc of Prof. Feng Jiao’s group at UD 36

Figure 2-5: I-V curves calculated for 5-, 6- and 7-cell module configuration and the electrolyzer for comparison. The current is plotted against the left axis and the FE is plotted against the right axis, with respect to voltage. The point of intersection between a solar array I-V curve and the electrolyzer I-V predicts the operating point for the respective configuration and is compared with the solar array maximum power point. In all these configurations that use a full cell area, the maximum power current is $\sim 3 \text{ A}$, much higher than the electrolyzer current of $\sim 1 \text{ A}$ at peak FE..... 38

Figure 2-6: Modeled I-V curves of the 5-cell PV array under different solar illumination areas and linear voltammogram curve of CO_2 electrolyzer with Nafion XL cathode. The intersection points give the I_{OP} and V_{OP} for the device setup. The black diamond on each I-V curve highlights the PV array maximum power point 40

Figure 2-7: Resulting J_{OP} and V_{OP} values for configurations with varying PV cell area. J_{OP} (given as the red curve) can be seen to decrease with increasing cell area whereas V_{OP} increases with increasing cell area 42

Figure 2-8: Extrapolated FE and calculated SFE for the illuminated cell areas (A) considered. Note that SFE vs. solar cell area curve follows the FE vs. solar cell area curve very closely. 43

Figure 2-9: Modeled IV curves for a 6-cell array configuration with CO_2 electrolyzer linear voltammogram..... 45

Figure 2-10: Calculated V_{OP} and I_{OP} with cell area for 6 cell PV array 45

Figure 2-11: SFE and FE with cell area for 6 cell PV array..... 46

Figure 2-12: Practical experimental setup showing PV module array illuminated by the solar simulator 47

Figure 2-13: Practical experimental setup showing the CO_2 electrolyzer in the fume hood, being run by the solar simulator 47

Figure 2-14: Measured I_{OP} vs. time for the configurations listed in Table 2 with different PV illumination areas in 5-cell configuration.....	48
Figure 2-15: J_{OP} and V_{OP} vs. cell area. Cell area obtained from results of practical demonstration of PV-driven CO_2 electrolyzer using 5-cell array. Note that the qualitative shape of this curve agrees well with that of the predicted J_{OP} and V_{OP} vs. solar cell area, given in Figure 2-7.....	49
Figure 2-16: Measured FE_{CO} vs. time for the configurations listed in Table 2 with different PV illumination areas in 5-cell configuration.....	51
Figure 2-17: Measured FE and the corresponding SFE plotted against solar cell illumination area.....	51
Figure 2-18: Comparison of solar-array I-V curves generated from the load-matching model, with those measured under the home-made solar simulator.....	53
Figure 2-19: Comparison of solar-array I-V curves generated from the load-matching model, with those measured under the home-made solar simulator. Here, the x-axis is expanded to emphasize the difference in the curvature of each of the plots. This shows that the model used in this work is reliable, when empirical losses are incorporated.....	54
Figure 3-1: Schematic of a PV-EC system showing the different coupling strategies possible. P_{IN} is the input power generated at the solar array at voltage V_{IN} , and current I_{IN} and P_{OUT} is the power delivered to the electrochemical cell at voltage V_{OUT} and current I_{OUT} , with a coupling efficiency $\eta_{coupling}$	62
Figure 3-2: (a) Power vs. voltage curves of the PV array of an example PV-EC system for changing insolation during a day, overlaid with the power vs. voltage curve of its electrolyzer load. The MPP points are indicated by blue diamonds at peak of each curve. (b) Graphical representation of the performance of a power optimizer device comprising MPPT and a voltage regulator. The red dot represents the operating point (power and voltage) for a directly connected PV-EC, while the green dot represents the operating point in a PV-EC coupled with a DC power optimizer.	67

Figure 3-3: (a) FE curve of CO ₂ electrolyzer used for the model. (b) Calculated SFE plotted against solar irradiation for directly-connected and power-optimizer-coupled PV-ECs (c) A plot of operating voltage against solar irradiance, showing a near-linear dependence between the parameters, allowing for a qualitative comparison of the FE (V) and SFE (Irradiance) plots (a) and (b).....	70
Figure 3-4: Annual gas output from the DC power optimizer configuration as a function of its power conversion (coupling) efficiency.	72
Figure 4-1: (a) Single-cell I-V curve of a PEM water electrolysis cell, (b) I-V curve of a single SunPower [®] SPE20-435 module used to power the PEM electrolyzer, with MPP indicated.	74
Figure 4-2: I-V curves of 2.1 MW PEM electrolyzer overlaid with the STC I-V curves of the solar array designed the optimally matched ‘Direct Coupling-1’ configuration with MPP indicated.	76
Figure 4-3: Power vs. Voltage—P(V)—curves of 2.1 MW PEM electrolyzer overlaid with the STC I-V curves of the solar array designed for ‘Direct Coupling-1’, optimally matched with MPP indicated.	76
Figure 4-4: Hourly efficiency profile shown for a typical sunny day in August of the model year, (a) in comparison to hourly irradiation and (b) module temperature	77
Figure 4-5: Hourly efficiency profile shown for a typical cloudy day in August of the model year, (a) in comparison to hourly irradiation and (b) module temperature	78
Figure 4-6: Annual gas yield of power optimizer coupled PV-EC as a function of the coupling electronics power conversion efficiency. Annual gas output from Direct Coupling1 are shown without power coupling. The red line with symbols is for a system using power optimizer with variable power conversion efficiency.....	79
Figure 4-7: I-V curves of 2.1 MW PEM electrolyzer overlaid with the STC I-V curves of the two solar arrays designed for direct coupling—one optimally matched (‘Direct Coupling-1’) and one slightly offset from it (‘Direct Coupling-2’), with MPPs indicated. The PV array in Direct Coupling-2 is designed to have a 25% voltage mismatch relative to Direct Coupling-1, discussed in Section 4.1.	81

Figure 4-8: Power vs. Voltage—P(V)—curves of 2.1 MW PEM electrolyzer overlaid with the STC I-V curves of the two solar arrays designed for direct coupling—one optimally matched (‘Direct Coupling-1’) and one slightly offset from it (‘Direct Coupling-2’), with MPPs indicated. The PV array in Direct Coupling-2 is designed to have a 25% voltage mismatch from that of Direct Coupling-1, discussed in Section 4.1.....	82
Figure 4-9: Annual gas yield of power optimizer coupled PV-EC as a function of the coupling electronics power conversion efficiency. Results from both well matched (Direct Coupling1) and mismatched (Direct Coupling 2) are shown without power coupling. The red line with symbols is for either system using power optimizer.	83
Figure 5-1: (a) Calculated transition energy levels of group V elements in CdTe lattice by Wei <i>et al.</i> [56] in CdTe band gap (b) atomic radii and defect formation enthalpies in relation to their suitability as p-type dopants in CdTe	90
Figure 5-2: Device structure of diagnostic CdTe:Sb solar cells.....	92
Figure 5-3: Schematic of the VTD reactor at the Institute of Energy Conversion, employed to deposit Sb-doped CdTe layer	94
Figure 5-4: Sb incorporation shown in CdTe:Sb film deposited using VTD at the IEC, measured using SIMS at Evans analytic group, taken from ref. [58]	95
Figure 5-5: Picture of an ampoule receiving Cd-vapor treatment. Shown here are 3 CdTe:Sb film coupons placed at multiple locations strategically to expose each of these samples to different temperature, dependent on their location in the ampoule with respect to the heat source.	96
Figure 5-6: Schematic of CdCl ₂ anneal by (a) CdCl ₂ coat method and (b) CdCl ₂ vapor method.....	98
Figure 5-7: A photograph showing finished diagnostic CdTe:Sb devices made on glass substrates (a) from the top and (b) from the bottom. Note that the carbon contacts define the area of the solar cell. The substrate in the picture was ~1 x 1 cm ² and the graphite cell contact is approximately 3 mm in diameter.....	99
Figure 5-8: Photograph of a coupon (measuring ~1” long) processed with 4 devices of ~8 mm ² area	100

Figure 5-9: Equivalent circuit model of diagnostic CdTe:Sb devices..... 102

Figure 5-10: A qualitative representation (distance and energy axes are not to scale) of equilibrium band diagram (dark, no applied bias) of diagnostic devices corresponding to the CdS/CdTe/C stack. The junction between CdTe and the p-type contact (CdTe/C) is expected to be a blocking barrier since Cu-doping was not performed on these diagnostic devices to ameliorate the. $\Phi_{BI} > \Phi_C$ in real devices. 102

Figure 5-11: Equivalent circuit mode of the device under test (solar cell) provided to the LCR instrument for capacitance measurement 105

Figure 5-12: (a) Raw C(V) data and (b) corresponding carrier density profiles of a sample set containing CdTe:Sb diagnostic devices made from CdTe films (i) as-deposited, (ii) with Cd vapor treatment, and (iii) with both Cd-vapor treatment and CdCl₂ device anneal. 106

Figure 5-13: (a) Raw data of admittance spectroscopy taken at 0V dc bias. This consists of capacitance vs. frequency measured at different temperatures from -140°C to +30°C in ~10°C step size (b) a plot of the derivative of capacitance vs. frequency to find the inflection capacitance as a peak of this curve (c) Arrhenius plot of the inflection frequencies, whose slope gives an activation energy of the charge response, that can be potentially attributed to multiple factors. These include a recombination center in the absorber material, the barrier height of a blocking contact, if applicable, or carrier freezeout [97], as dictated by equation (5-4)..... 109

Figure 5-14: A plot of measured V_{OC} as a function of temperature, shown here being used to extrapolate V_{OC} (0K)..... 111

Figure 5-15: (a) JV(T), Dark raw data of a device given for demonstration of barrier potential extraction (b) a plot of dV/dJ vs. 1/J for series resistance extraction from large forward biases. [77] Using this, the contact resistance (R_C) is calculated for different temperatures (c) Arrhenius plot of R_C for estimation of an activation energy that serves as an estimate of the blocking barrier potential [100] 113

Figure 5-16: (a) QE data for two Sb-doped devices: with and without device anneal treatment. (b) dQE/dE_λ plots to extract absorber bandgap for these two devices 115

Figure 5-17: (a) A plot of V_{OC} as a function of solar intensity ('Suns'), (b) plotted as $\ln(J_{SC})$ vs. qV_{OC}/KT to extract ideality factor n and reverse saturation current density, J_0 , using equation (5-12). 116

Figure 6-1: JV curves of devices from the anneal matrix, with an apparent S-shape for all the devices indicating the presence of a blocking contact. The dashed and the blue curves can be directly compared as they have received similar device anneal treatments ('Air+CdCl₂ vapor'). It can be seen that Sb-doped ('Air+CdCl₂ vapor') device has a severe 'S'-shape, indicating the presence of a leaky blocking contact. It also exhibits a lower V_{OC} , J_{SC} and FF than the baseline device. 122

Figure 6-2: Tabulated JV and CV parameters of CdTe:Sb devices from the anneal matrix shown pictorially for comparison 124

Figure 6-3: Measured V_{OC} 's of devices from anneal matrix, compared with expected V_{OC} 's, calculated using equations (6-8) and (6-6) as a function their measured N_{CV} , for 10 ns τ_n and a maximum J_{SC} of 28 mA/cm². The note on the right is attributing this deficit to recombination in the devices. 132

Figure 6-4: Plot showing (a) V_{OC} , and (b) corresponding TRPL lifetime extracted from the empirical relationship given in equation (6-11), as a function of ΔN_{CV} , with the exception of the very-low doping ('CdCl₂ coat only) device on the left whose absorber layer is likely depleted of charge carriers. The remaining devices from the anneal matrix show that their V_{OC} and expected τ_{PL} are limited by defect density, given by ΔN_{CV} 134

Figure 6-5: (a) JV curve of the best Sb-doped device processed at IEC and its (b) tabulated device parameters 139

Figure 7-1: Band diagram of CdTe:Sb devices illustrating the unknown nature of defects contributing to deficit in performance. 146

ABSTRACT

This dissertation comprises two discrete topics concerning photovoltaics, both detailed below: analyzing solar electrolyzer design and operation towards optimizing their performance under realistic conditions; and characterizing extrinsic p-type doping in thin-film CdTe solar cells using Sb for improved voltage output.

Solar fuel generation, i.e. production of H₂ via electrochemical reduction of water, has witnessed considerable growth since the identification of photocatalysis four decades ago. More recently, photoelectrochemical cell (PEC) reduction of CO₂ to CO as a precursor to other fuels, i.e. ethanol, has been demonstrated. Numerous photovoltaic electrochemical cells (PV-ECs) and photoelectrochemical cells (PECs) with efficiencies reaching 30% for H₂O reduction and 10% for CO₂ reduction have been reported. However, the scalability of such devices, specifically for solar CO₂ reduction has still not reached promising maturity. In this work, a high efficiency PV-EC is implemented, using silicon solar cells and a flow-cell CO₂ electrolyzer of 25 cm² electrode area, larger than that of any CO₂ electrolysis device hitherto reported in literature. The Si array was carefully configured to match the operating characteristic of the flow cell electrolyzer. We then developed a model to optimize the design of such devices under generalized operating conditions. Realistic losses due to temperature, irradiance, and ohmic losses are incorporated allowing the model to simulate and scale the annual outdoor field performance. The benefit of using power electronic devices with decoupled PV-ECs was also explored using this model, which showed that an improvement in annual gas yield of >5% is possible in optimally matched configurations. This benefit can be much higher if the solar and electrolyzer cells are not optimally matched.

Polycrystalline thin-film CdTe/CdS heterojunction solar cells are the leading commercial competitor to c-Si solar modules. While having demonstrated good performance at low cost and large scale, they still have immense potential for efficiency improvement through enhanced open circuit voltage (V_{OC})—from its current ~ 0.85 V to the near-ideal 1.1 V— if carrier concentrations exceeding $5 \times 10^{16} \text{ cm}^{-3}$ can be achieved simultaneously with sufficient minority carrier lifetimes of 1-10 ns. State-of-the-art intrinsic CdTe solar cells, wherein n- or p-type doping is achieved through native point defect (V_{Cd}) control during film growth, are limited to acceptor concentration levels of $< 10^{15} \text{ cm}^{-3}$. Aiming to bridge this V_{OC} gap through extrinsic doping of polycrystalline CdTe films with Sb during their growth using vapor transport deposition technique will be examined in this work. Specifically, this work focuses on using device characterization and analysis techniques to evaluate different post-growth device treatments for realizing the high V_{OC} in these devices and to analyze the loss mechanisms in Sb-doped solar cells.

Chapter 1

INTRODUCTION: SOLAR FUELS AND CADMIUM TELLURIDE SOLAR CELL DOPING

This dissertation comprises two discrete topics concerning photovoltaics: optimizing solar electrolyzer performance by modeling and evaluating their holistic field performance, discussed in Section 1.1 and enhancing p-type doping in thin-film CdTe solar cells for improved voltage output, in Section 1.2.

1.1 Solar Fuels

1.1.1 Motivation

The critical need to reduce carbon intensity in global energy usage to avoid the worst effects of climate change cannot be overstated. There are two parallel paths to achieve this: 1) increasing use of low-carbon renewable energy sources; and 2) removing or sequestering carbon from the atmosphere. For low-carbon renewable sources of electric power generation like solar, wind and hydro to meet the 30% renewable energy target by 2025 in the United States [1], they will need to be augmented with reliable storage systems. While substantial reforestation efforts help to curb the incessant greenhouse emissions, a more rapid and efficient approach to reverse the process is needed.

One solution capable of addressing the above challenges lies in the development of efficient, stable, and cost-effective artificial photosynthesis systems, capable of generating solar fuels. The term ‘solar fuels’ refers to renewable generation of fuels

using solar energy, specifically utilizing the photovoltaic effect for electrolysis of common compounds to manufacture chemicals for energy generation. It is well known that hydrogen gas can be produced through water electrolysis. Similarly, several types of hydrocarbons, and carbon monoxide (a precursor for producing hydrocarbons), can be produced from carbon dioxide electrolysis. Significant advancements were witnessed in the past half century in photovoltaics (PV) and electrochemistry. Most research has focused on the science of the electrochemistry or the technology of their physical integration while there has been relatively little work looking at the efficient electrical coupling of these two systems for solar fuel generation.

Another promising aspect of solar fuels lies in their application as energy storage mechanisms. When compared to other forms of storage such as batteries, fuels—specifically liquid hydrogen and hydrocarbons—hold enormous potential due to their significantly higher energy densities, as shown in Figure 1-1. It is apparent from this figure that electrochemical energy stored in the form of fuels as liquid hydrogen and hydrocarbons has enormous storage potential. This is evident in their orders-of-magnitude higher energy densities compared to traditional storage mechanisms such as li-ion batteries. Additionally, they also provide easy dispatch in the form of liquid fuels or compressed gases, and do not call for a significant change from present day energy infrastructure.

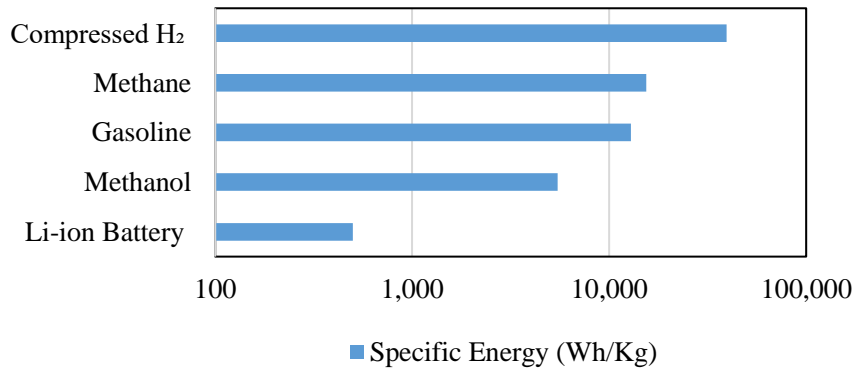


Figure 1-1: Energy densities for different storage mechanisms- note that the horizontal axis is shown in log scale

1.1.2 Device Architectures

Solar fuel generation devices can be broadly categorized into two architectures: (1) photoelectrochemical cell (PEC) (ii) photovoltaic electrochemical device (PV-EC). The device schematics of these two types of systems are given in Figure 1-2. PECs consist of a photoactive material immersed in the solution containing the reacting electrolyte and the potential to drive the electrolysis reaction is typically obtained under illumination at the electrode-electrolyte junction. A PV-EC on the other hand is an entirely decoupled device, where a photovoltaic system drives an independently designed electrolyzer to produce the desired gas product. Other device strategies between these two extremes are also possible and their taxonomy is discussed well in the literature. [2]

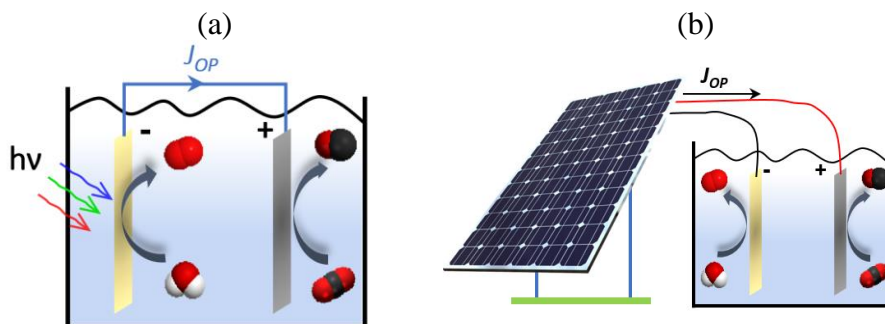


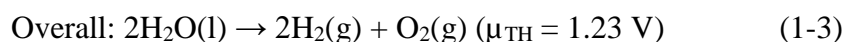
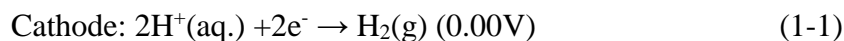
Figure 1-2: Schematic depicting (a) an integrated photoelectrochemical cell (PEC) device architecture where the photoactive component is immersed in the electrolyte and (b) a decoupled PV-EC device architecture with an independently designed photovoltaic device powering an independently designed electrochemical cell.

PEC-type devices have been under development for over 45 years and have many well-documented disadvantages [2]: (i) limitations in obtaining photovoltages large enough to drive desired reactions from a single-junction device; (ii) material compatibility of photoactive component in potentially corrosive electrolyte solution which complicates device design and manufacturability, requiring the use of protective layers and/or compatible electrocatalysts, and (iii) optical losses due to inherent design and fabrication which limits the materials selection available for device application, and (iv) compatibility of materials processing with device structure. Most reported PECs have employed multi-junction III-V solar cells in order to achieve the required high voltages of >1.23 V for water splitting and >1.34 V for carbon dioxide splitting. [3], [4], [5] Such III-V devices are difficult to manufacture, very expensive and are not yet commercially available.

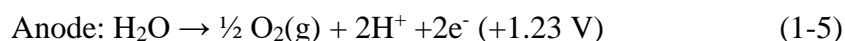
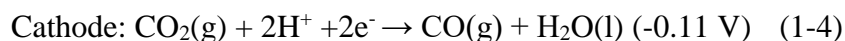
PV-EC device design, however, offers many advantages over PECs since the separation of the optical and electrical components allows a greater selection of materials and eliminates concerns of processing compatibilities and solution stability of the light active components, as well as allowing the use of the high quality electrocatalysts and commercially available components that can easily be incorporated into its design. Low-cost and reliable silicon-based and thin film PV cells and modules are already widely available and can be easily configured to provide the needed current and voltage independently. Series-connected solar cells to obtain sufficient photovoltages to drive the electrolytic reactions have recently been demonstrated for both H₂O splitting and CO₂ reduction. [6] Parallel-connected cells or modules increases the current density available independent of the electrolyzer area. PV-EC architecture thus allows for series-connected solar array configurations, resulting in suitably high voltages to be obtained that is otherwise impossible for PEC approaches with single junction photoactive components. A PV-EC system with suitable electrocatalysts thus has the promise for efficient and practical solar driven manufacture of different species, including fuels and other industrially-relevant chemicals.

1.1.3 Water and carbon dioxide electrolysis

In the case of water electrolysis, two protons accept an electron each to make a H₂ molecule at the cathode; while two OH⁻ ions lose two electrons each to make an oxygen molecule and two protons at the anode. The electrode reactions are given below with their standard electrode potentials:



μ_{th} being the thermodynamic voltage for the overall reaction of water electrolysis to hydrogen and oxygen. The electrolytic reduction of carbon dioxide to carbon monoxide is the focus of the experimental portion of this work, where carbon monoxide is generated at the anode, along with a competing hydrogen evolution reaction, and oxygen is produced at the cathode, as given below.



It can be seen from the above reactions that the overall potential required to split water to produce hydrogen, μ_{th} , is 1.23 V, while reducing carbon dioxide to carbon monoxide is 1.34 V. Considering that most single junction photovoltaic devices yield open circuit voltages under 1V, it is not possible to achieve these high splitting voltages using single junction photoelectrodes in PEC configuration.

Many aspects of H₂ generation by water electrolysis have been extensively studied and optimized—from electrode materials to scaling and technology integration—and much of this knowledge can be transferred to the design of CO₂ reduction devices.

While H₂ produced from water electrolysis can be readily applied as a fuel or for industrial usage, carbon dioxide electrolysis can be employed to either produce hydrocarbons directly, or to produce carbon monoxide which would then be a precursor gas for producing hydrocarbons. The Fischer-Tropsch (F-T) process can be used to produce synthetic gasoline and/or diesel fuel using H₂ and CO precursors. [7] This route is more desirable compared to the direct electrolytic production of hydrocarbons from CO₂ for multiple reasons: the electrolytic reduction potential of CO₂ to CO is the

relatively small, the selectivity (against H₂ production) is relatively high, and the collection of product gases is relatively easy as CO and H₂ are the only two products at the cathode. Further discussion on the details regarding the design of the electrochemical devices and the electrochemistry of the reactions of interest—other than their electrical behavior—are beyond the scope of this dissertation (although they are accessible through the cited references).

1.1.4 Figure of Merit:

Like other energy conversion devices, the efficiency of solar fuel generation devices is calculated as a ratio of the energy output to the input energy. In the case of solar fuel devices, it is measured as the electrochemical energy content of the product gas divided by the input solar intensity. This generally accepted figure of merit for solar fuels systems is called ‘solar to fuel efficiency, given as:

$$SFE = J_{OP} \times \frac{\mu_{TH}}{P_{IN}} \times FE \quad (1-7)$$

where FE is Faradaic efficiency which is the ratio of the charge converted to desired product to that of the total charge transferred to the electrochemical cell over the period of operation, μ_{TH} is thermodynamic voltage for electrolyzing the reactants to products, which for H₂O to H₂ is 1.23 V and CO₂ to CO is 1.34 V, J_{OP} is operating current density, P_{IN} is the input solar insolation. J_{OP} for an integrated PEC device is not necessarily the same as the photoelectrode’s maximum current density, J_{MP} , and for this reason such a device configuration does not allow for maximum energy delivered for electrochemical reaction. This is the primary advantage of a decoupled PV-EC architecture, which allows for independent control of J_{OP} . The derivation of the above equation in the

context of decoupled PV-ECs is explained below although the same applies to PEC devices as well.

The SFE of solar fuel devices is reported for PV performance under what are known as ‘standard testing conditions’ (STC) at an irradiance of 100 mW/cm^2 (known as ‘1-sun’) with a specific spectral distribution (Air Mass 1.5 (AM1.5)) and 25°C operating temperature. While this offers a standardized and universally accepted figure of merit for comparing and testing devices, this metric does not capture its sensitive dependence on illumination and temperature, specifically for decoupled PV-EC devices. Considering that most PV-EC devices are designed for STC operation, their real-life performance varies significantly due to the suboptimal matching of their current-voltage curves at non-STC conditions. This subject is poorly explored for solar fuel devices in the literature.

1.1.4.1 SFE of PV-EC devices

Let us consider the PV-EC device to be a system comprising three components—the PV source, the coupling device and the electrochemical load as given in Figure 1-3. In addition to a direct connection of the PV ‘source’ and the electrochemical ‘load’, this particular PV-EC architecture also offers the benefit of employing a ‘coupling device’ which facilitates an efficient transfer of power between the source and the load.

The efficiency for such a system can be given as a product of the efficiencies of individual components, given by equation 1-8. The PV efficiency given in equation 1-9 will be discussed in the section 1.2.3 in more detail. The overall electrochemical reaction in every electrochemical cell typically requires a higher operating potential than the thermodynamic potential to account for non-idealities in the electrolyte arising from

mass transport, electrode and electrolyte resistances, etc. This excess voltage is called ‘overvoltage’ or ‘overpotential’. FE is a measure of the electrochemical cell electrocatalyst selectivity to the desired product gas as mentioned in the earlier section. The total voltage supplied to the electrochemical cell which is the same as its operating voltage is termed V_{OP} , and the current at this voltage is termed operating current, I_{OP} . The efficiency of the electrochemical cell is, therefore, measured as the ratio of the electrochemical energy stored in the product gas—a product of the thermodynamic potential of reduction and the FE—to that of the overall electrochemical potential supplied to it, as given in equation 1-10. It can approach 100% for today’s low-loss power electronic devices. The efficiency of the coupling device is again the ratio of the power it receives from the PV source to the power it delivers to the electrochemical cell, as given in equation 1-11. The efficiency of the entire system for solar fuel conversion, η_{SF} , can be thus be calculated as given in equation 1-12.

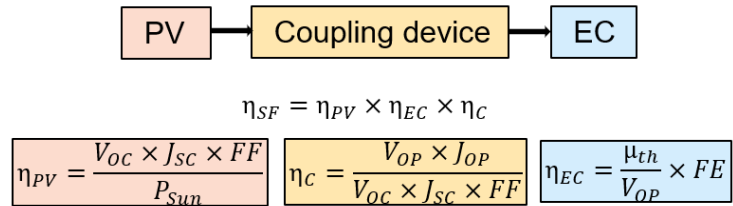


Figure 1-3: Block diagram of a PV-EC to illustrate derivation of its SFE

$$\eta_{SF} = \eta_{PV} \times \eta_C \times \eta_{EC} \quad (1-8)$$

$$\eta_{PV} = \frac{V_{MP} \times I_{MP}}{P_{Sun}} \quad (1-9)$$

$$\eta_{EC} = \frac{\mu_{th}}{V_{OP}} \times FE \quad (1-10)$$

$$\eta_C = \frac{P_{OUT}}{P_{In}} = \frac{P_{EC}}{P_{PV}} = \frac{V_{OP} \times J_{OP}}{V_{MP} \times I_{MP}} \quad (1-11)$$

$$\eta_{SF} = \eta_{PV} \times \eta_C \times \eta_{EC} = \frac{\mu_{th} \times J_{OP} \times FE}{P_{Sun}} \quad (1-12)$$

In the following section, the history of the progress of solar fuel research will be discussed with a review of literature.

1.1.5 Literature Review

Solar water electrolysis began with the first discovery of catalyzed splitting of water on illuminated TiO₂ and Pt electrodes in 1972. [8] A demand for cheap and sustainably sourced fuels following the oil crisis of 1973 intensified solar fuel research and significant advancements were made in the field in the decades to follow. A >12% solar water electrolysis device was reported by NREL in 1998 [9]. The highest efficiency reported to-date for water electrolysis devices is 30% [10] for a PV-EC type device with a tandem solar cell under high solar concentration driving an independently designed water electrolyzer.

While electrochemical conversion of CO₂ has been studied for over 100 years [11], its potential for carbon capture and sustainable sourcing of fuels was only realized through photoelectrochemical reduction in the past few decades [12]. Such an approach where the photovoltaic effect is used to drive electrolysis of carbon dioxide is termed ‘artificial photosynthesis’ [13]. Earliest reports of photocatalytic reduction of CO₂ date back to 1978 when methane formation on strontium titanate coated with platinum catalyst under UV light illumination was reported by Hemminger *et al.* [14], while

formation of formic acid, formaldehyde and methanol evolution was reported by Halmann *et al.* on p-type gallium phosphide photoelectrode [15]. Panasonic claimed the record for formic acid conversion of 0.2% [6] in 2012. Recently, decoupled solar electrolysis of CO₂ to CO with 6.5% SFE was reported by Schrier *et al.*, employing a perovskite solar cell array [16]. The highest efficiency reported for CO₂-reduction thus far is 10%, reported by Zhou *et al.* where a bipolar membrane was used with separated electrolytes for CO₂ reduction reactions and oxygen evolution reactions (OER), using a multijunction photoabsorber of small electrode area [17]. It is to be noted the above two record-efficiency devices achieve high efficiencies using diminishingly small electrode areas of <0.1 cm², and therefore do not address their scalability. The evolution of record-efficiency solar fuel devices for water and CO₂ electrolysis using several approaches up until 2014 has been thoroughly reviewed by Ronge *et al.* [18] It is evident that most of current research is focused on catalysis materials discovery, characterization, and processing of multijunction photoelectrodes to provide sufficient voltage. All PECs reported in the literature are not only made with very expensive multijunction solar cells as photoelectrodes but are also made on extremely small device areas. This limits their scalability beyond lab scale devices, made for the purpose of reporting high SFEs. In this work, we explore: the decoupled PV-EC architecture using commercially available but high efficiency Si solar cells or modules as a route to enable larger-scale devices; the practical aspects such as calculating the PV-EC system annual field performance; and optimally configuring PV arrays for maximum power delivery and fuel production.

1.1.6 Thesis statement for PV-EC Aspect

This work seeks to employ the decoupled architecture for solar electrolysis devices to exploit the several advantages they offer. We explore the practical aspects of

these devices beyond just designing them by fabricating and characterizing them to maximize their standard performance metrics. This work seeks to put forth an analytical framework for optimal coupling of PV-EC devices by applying load matching techniques to systems composed of existing photovoltaic and electrochemical devices and to study their realistic performance by developing and applying an annual generation model.

1.2 Cadmium Telluride Solar Cells

1.2.1 Introduction to thin film CdTe Photovoltaics

Polycrystalline cadmium telluride (CdTe) thin-film solar cells are the second most common photovoltaic technology after crystalline silicon (c-Si), although only representing 5% of the world market share in 2016. Due to the direct bandgap of polycrystalline CdTe material, $E_g = 1.45$ eV, it is optimally matched to the solar spectrum for photovoltaic conversion. Its high absorptivity, $>10^5$ cm⁻¹, leads to a high quantum yield over a wide spectral range, resulting in >99% absorption of the solar spectrum within 2 μ m of the material thickness. This makes it well-suited to efficiently convert AM 1.5 sunlight to photocarriers, making it nearly optimal for single junction photovoltaic conversion. This chapter will discuss the history of the growth of thin film CdTe photovoltaics, its state-of-the art device structure and equivalent circuit configuration, performance metrics and the routes to enhance their performance.

1.2.1.1 History of CdTe Photovoltaics

Since its emergence as a new electronic material in 1947 [19], CdTe was first proposed for use in photovoltaic solar energy conversion in 1956 [20]. As methods for controlling p-type and n-type conductivity of the material were established subsequently by 1960, single crystal homojunction CdTe solar cells were studied initially [21], [22], reaching >10% energy conversion efficiency. [23]. Following the initial single crystal solar cell reports, p-n heterojunction solar cells were widely investigated since 1960 for n-type and p-type CdTe absorbers. With n-type single crystals having a thin film CdTe/Cu₂Te heterojunction structure, similar to Cu₂Te solar cells, >7% efficiency was reached by the early 1970s [24]. Following studies on single-crystal p-type CdTe with evaporated n-type CdS in the mid-1960s, [25], [26], [27] focus finally converged on

heterojunction solar cells made with evaporated p-type CdTe thin film absorber layers and n-type CdS film emitter layers in *substrate* and *superstrate* configurations to take advantage of the higher carrier mobility of electrons compared to holes in CdTe thin film material.

Superstrate configuration CdTe solar cells were first demonstrated in 1969 by Adirovich *et al.* with efficiency >2% [28]. Subsequent enhancements in device efficiencies were gained by employing several fundamental studies and empirical process refinements including: thinning the CdS layer and improving TCO increased for J_{SC} enhancement, understanding and reducing the back-contact barrier to increase the fill factor (FF), postdeposition treatment techniques and optimizing device design for improving the V_{OC} . The need for postdeposition exposure of the CdTe/CdS films to $CdCl_2$ and O_2 have remained enigmatically crucial for the device behavior. A controlled $CdCl_2$ device treatment was essential to enhance the device performance through various routes including: increased grain size, grain-boundary passivation, increased CdS/CdTe interface alloying which is known to reduce lattice mismatch between CdS and CdTe layers [29]. In recent years, adopting new emitter buffer layers such as magnesium zinc oxide (MZO), coupled with alloy grading with CdSe at the emitter-base interface (causing a slight reduction in bandgap), has led to J_{SC} enhancement. The best reported lab-scale CdTe device today has an efficiency of 22.1% and the best module efficiency of 18.6%, both reported by First Solar[®] in 2016. [30]

1.2.1.2 CdTe Toxicity

Toxicity issues related to CdTe modules have been studied and contested since the beginning of CdTe technology for large-area solar cell application. Even though this has led to the eventual abandonment of CdTe technology in Japan and other countries,

CdTe PV research and implementation of CdTe solar arrays is present in the rest of the world. In Europe, PV modules are currently exempted from ‘Restriction on Hazardous Substances (RoHS)’ standard, for stationary and professionally installed systems. Considering that a vast amount of cadmium comes as a waste by-product from zinc mining [31], concentrating cadmium in solar modules is contended to be less hazardous environmentally, when used in a closed cycle [32] [33]. The most toxic component, Cd, is contained between the glass and the encapsulant in the solar panel, and the mass ratio of CdTe to glass contained in a solar panel is <0.005 . It was experimentally demonstrated that 99.5–99.96% of Cd remains encapsulated in the molten glass during residential fires [34].

1.2.2 Low cost manufacturability of CdTe modules:

Due to CdTe having high absorptivity, almost all of incident light is absorbed within a couple of microns of thickness of this material. This means only a couple of microns of CdTe are needed in order to harvest available photons in PV structures. Additionally, all the other film deposition processes can be performed using high rate, low cost equipment, and materials (such as CdS, CdTe, CdSe on commercially available glass) with lower capital costs than needed for other semiconductor devices or c-Si solar cells. Once all the layers of a CdTe module are deposited, the contacts can be made using industrial laser patterning, eliminating need for slow and expensive lithographic patterning techniques. As such, polycrystalline thin film CdTe photovoltaic technology offers significant potential for the manufacture and implementation of efficient yet cost effective photovoltaics.

1.2.3 Device Structure, Performance Metrics

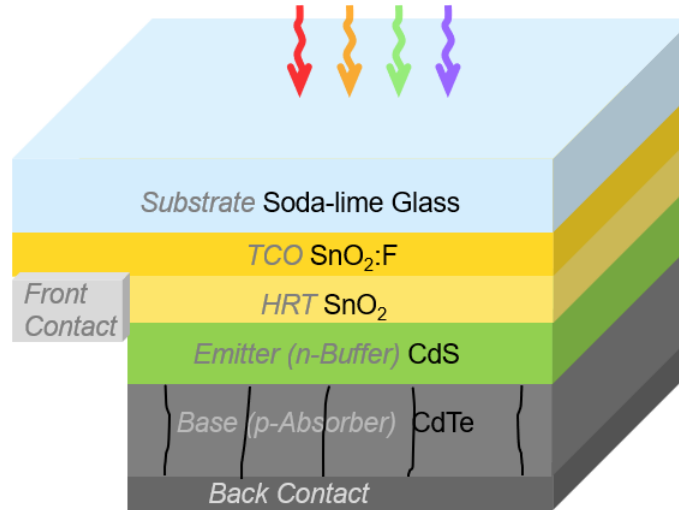


Figure 1-4: Device architecture of a state-of-the-art superstrate CdTe solar cell

The state-of-the-art CdTe device is a front wall superstrate configuration solar cell, given in Figure 1-4, illuminated from its top surface, through the glass. The glass is coated with a low resistance transparent conductive oxide (TCO) to enable lateral transport of carriers to the front contact and to enhance light transmission to the absorber layer by minimizing reflection due to its having an index of refraction midway between glass and CdTe. This is followed by a thin high resistance transparent (HRT) buffer layer employed to prevent junction formation of CdTe with the TCO in event of pinholes in the CdS. The TCO and HRT layers are collectively referred to as ‘window layers’ and can be formed from the same material (doped and undoped SnO₂) or as a bilayer of two transparent oxides. In the typical CdTe solar cell, the pn heterojunction is formed between the subsequent CdS n-type emitter layer and the CdTe p-type absorber layer.

The CdS needs to be extremely thin (5-30 nm) to minimize absorption losses. In newer generation cells, the pn junction is formed between an MZO emitter and an alloyed p-type Cd(TeSe) absorber.

In order to discuss the current-voltage (J-V) behavior of a solar cell, in which J is the current density and V is the voltage, it helps to consider the equivalent circuit of a solar cell under illumination, given in 1-5, for a typical CdTe solar cell with a slightly blocking contact at the back (explained below). With the solar cell under illumination generating a constant current density, the corresponding electrical circuit comprises a constant current source in parallel with the main pn junction diode in the dark. Other non-idealities such as the shunt conductance through and the series resistance across the device are accounted for as lumped circuit resistors— R_{Sh} and R_S , respectively. It is difficult to make an ohmic contact with CdTe since the work functions of most metals are smaller than the electron affinity of CdTe (χ_{CdTe})—4.28 eV. Several methods to alleviate this barrier have been developed, [35] with one solution comprised of Cu-doped CdTe towards the back surface, there can still be a slight barrier to current collection especially in non-optimized experimental structures as being discussed here. To account for this Schottky barrier in the back, a diode of reverse polarity with that of CdTe is placed in series with the main pn junction in the equivalent circuit along with a shunt conductance across this layer, $R_{Sh, back\ contact}$. Using this equivalent circuit, J-V behavior of this device can be accurately written [36]. For the sake of simplicity in the explanation of basic J-V behavior in this chapter, consideration of the back diode is omitted. We note that the back diode primarily influences the J-V behavior in far forward bias and at low temperature. The *two-diode model* is dealt with in greater detail in Section 5.4.

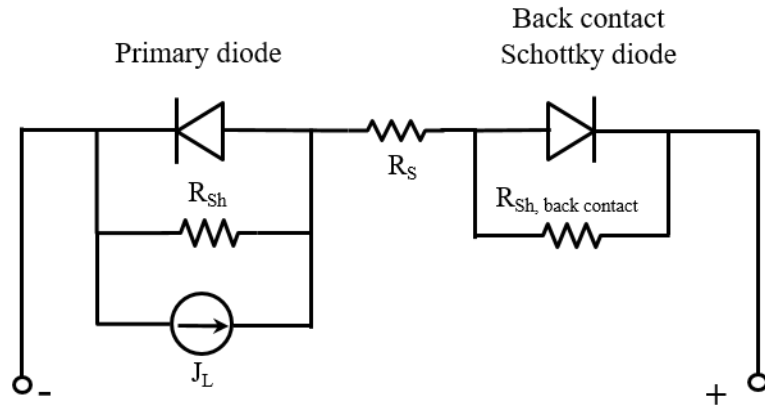


Figure 1-5: Equivalent circuit diagram of a CdTe solar cell under illumination, with the pn junction between the emitter CdS and the absorber CdTe is given on the right as the primary diode on the left and the blocking contact is depicted as Schottky contact diode on the right

Consequently, the current (density)- voltage equation of a solar cell is given in equation 1-13:

$$J(V) = J_{pn}(V) - J_L = J_0 \exp\left(\frac{qV}{AkT} - 1\right) - J_L \quad (1-13)$$

where $J_{pn}(V)$ is the voltage-dependent dark current of a pn-junction diode, J_0 is the reverse saturation current of the diode, A is the diode ideality factor, k is Boltzmann constant, T is the temperature. Only single-diode model is discussed in this chapter for the sake of introduction, the full 2-diode model will be discussed in later chapters. The resulting J-V curve of a typical solar cell in the dark and in the light, is given in Figure 1-6. This data is measured of a solar cell in standard testing conditions of 1-sun illumination intensity and spectrum, and 25°C operating temperature.

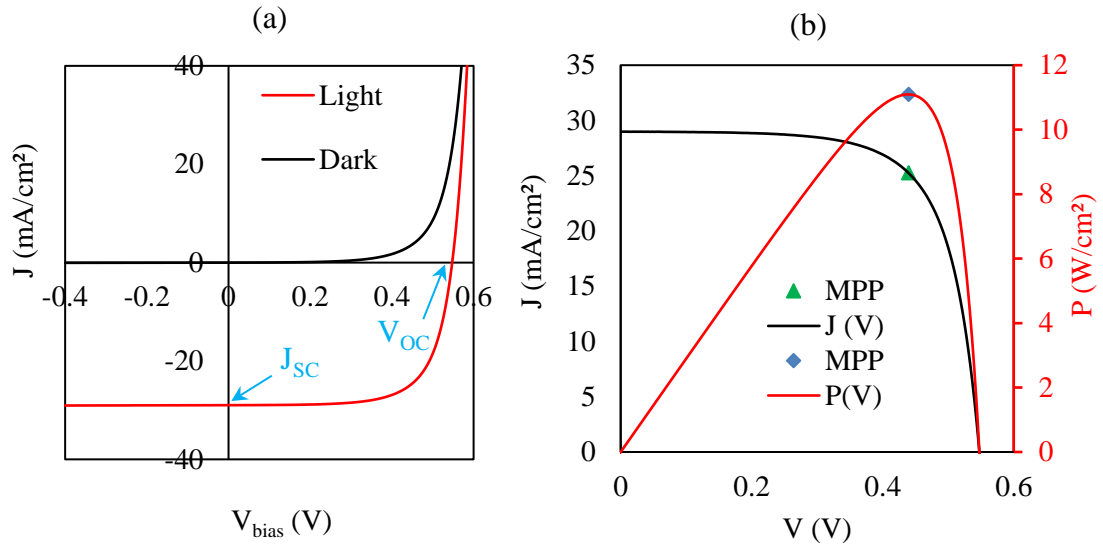


Figure 1-6: (a) Current density vs. voltage curves for a solar cell in dark and under illumination with voltage bias sweep (b) current-density and power vs. voltage curve of a solar cell under illumination in source configuration, showing the peaking of the output power and the maximum power points (MPP)

However, considering the other lumped circuit elements added to account for the series resistance across- and shunt conductance through the device, the complete current-voltage equation now becomes:

$$J(V) = J_0 \exp \left[\frac{q(V - JR_S)}{AKT} - 1 \right] + G_{SH}(V - JR_S) - J_L \quad (1-14)$$

where R_S is the effective series resistance per unit area in Ohm-cm², G_{SH} is the effective shunt conductance across the device in Siemens/cm².

The figure of merit for a solar photovoltaic device is measured as a ratio of output electric power from the device to input solar intensity. On the power versus voltage curve of a solar cell, there is only one voltage and current point at which the power peaks for the device and this is called the maximum power point. The power at

this voltage and current is the maximum output power produced by the device, P_{MAX} , and V_{MP} and I_{MP} are the voltage and current at this point. The power conversion efficiency of this device, η_{PV} , is, therefore, given as the ratio of the maximum power output P_{MAX} to the input solar insolation, P_{IN} , given by the equation 1-15:

$$\eta_{PV} = \frac{P_{MAX}}{P_{IN}} = \frac{V_{MP} \times I_{MP}}{P_{IN}} = \frac{I_{SC} \times V_{OC} \times FF}{P_{IN}} \quad (1-15)$$

where, I_{SC} is the total current at short circuit and V_{OC} is the voltage at open circuit under illumination, P_{IN} is the input solar intensity, FF is the fill factor—a measure of roundedness of the J-V curve given as the ratio of the maximum power output from the device to the product of the short circuit current and open circuit voltage.

Using equation 1-14 on the measured data of a solar cell, its individual lumped circuit parameters— R_s , G_{sh} , A and J_0 – can be extracted if its device structure can be approximated to a single-diode model. J_{SC} is directly affected by the light absorbed by the device and so is relatively easier to improve linearly by engineering the different optical properties of a solar cell. V_{OC} is dependent on the material quality of the device since it is a function of the dark saturation current. For this reason, the effective minority carrier lifetime, dictated by recombination at different device regions—bulk, interfaces, grain boundaries, surfaces—affect the device V_{OC} . The origins of losses in FF, on the other hand, are much harder to identify and improve. FF can be affected by several factors including, but not limited to: series and shunt resistances, recombination, voltage-dependent current collection (arising from a blocking contact or Auger recombination, etc.), photoconductance in the TCO or emitter layer, etc., making it a device metric whose improvement can only be realized through a holistic enhancement in the device, minimizing all these possible non-idealities.

1.2.4 Trend of increasing CdTe solar cell efficiencies

This section discusses the chronological record of reported highest efficiency devices in the last two decades. For lab-scale devices after 1990, a 15.8% efficiency cell was reported by Britt and Ferekides [37] in 1993, after which in 1997, Matsushita reported a 16% efficiency [38]. NREL reported 16.4% [39] and a 16.7% efficiency device both in 2001 by applying a cadmium stannate TCO [40]. After this, First Solar reported a 17.3% efficiency device in 2011 and GE reported 18.3% efficiency in 2012 [41]. In 2013, First Solar devices reached an efficiency of 19%, who also reported a 22% device in 2014 [42]. A graphical representation of the record efficiency device parameters is given in Figure 1-7.

During the period between 2001 to 2011, the market presence of CdTe has increased substantially with GE, First Solar and Matsushita active in the thin film CdTe market, despite the slow growth in reported device efficiencies. Scaling up the device performance to large area module efficiencies for CdTe technology was minimally limited by the compositional nonuniformities unlike the commercialization of other solar technologies. Graded bandgap CdTe for increased absorption along with improved window layers [43] were among the few techniques employed successfully at First Solar[®] leading up to their improved efficiencies. It holds the current record for both device and module efficiencies at 22% and 16% respectively. Although the device current density and fill factor saw significant enhancement over the last two decades, the device V_{OC} has fallen short of expectations to reach a predicted 1.1 V [44].

1.2.5 V_{OC} Enhancement

The radiative-limited Shockley-Queisser limit of efficiency for 1.45 eV bandgap CdTe solar cells is 32% with a V_{OC} of 1.2V, J_{SC} of 30 mA/cm², fill factor of 89.7% [45].

On the other hand, consider the record efficiency cell reported by First Solar in 2016, with an efficiency of 22%, V_{OC} of 0.88 V, J_{SC} of 30.25 mA/cm² and a FF of 79.4%. [46] From the chronological record of device parameters in Figure 1-7, it is apparent that the current density and the fill factor of the record efficiency lab cell are close to the radiative limit by 90% and 85% respectively, there is still significant room for improvement with V_{OC} , which is only 80% that of the ideal value. Of the 3 parameters (V_{OC} , J_{SC} , FF) it is commonly observed that V_{OC} will have the largest deficit relative to the S-Q limit, indicating that V_{OC} losses are difficult to identify and overcome.

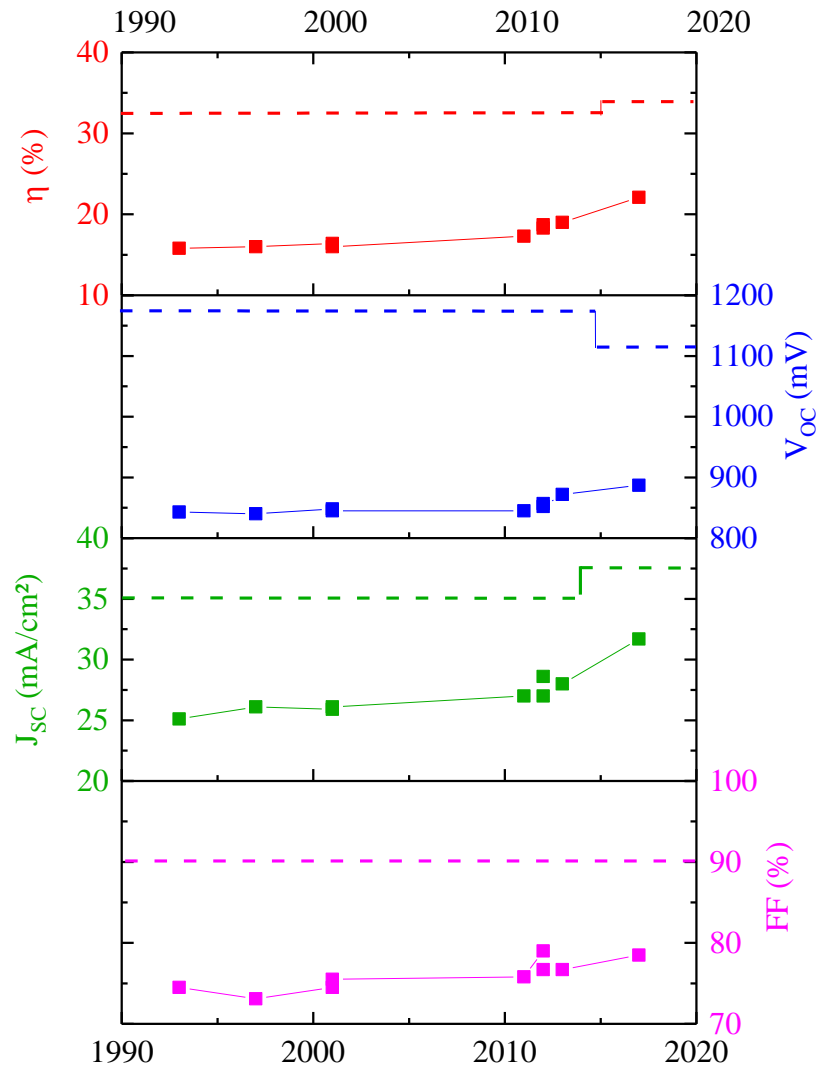


Figure 1-7: Chronological record of thin-film CdTe solar cell record efficiency device parameters, compared with the theoretical Shockley-Queisser (S-Q) limit as a function of the bandgap of the corresponding absorber (shown as a dashed line in each of the plots). The yellow point shown in the V_{OC} graph is the V_{OC} possible with $5 \times 10^{16} \text{ cm}^{-3}$ doping. The theoretical limits for the η , J_{SC} , and V_{OC} of the latest record efficiency device (reported in 2016) are different since its absorber ($\text{CdTe}_x\text{Se}_{1-x}$) has a slightly lower bandgap (E_g) of $\sim 1.42 \text{ eV}$, compared to the previous devices whose CdTe absorbers have $\sim 1.45 \text{ eV}$. The corresponding disparity in absorber bandgap does not account for a considerable disparity in device FF is comparatively small.

State-of-the-art CdTe device technology has relied on intrinsic doping of the CdTe layer with Cd vacancies (V_{Cd}), which are poorly understood and difficult to control. These vacancies form neutral or singly charged acceptor-type defects $N_A^{0/-}$ depending on the lattice site. CdTe film growth is engineered to thermodynamically enable the formation of these Cd vacancies. This technique, however, limits the charge carrier concentration to $<5 \times 10^{14} \text{ cm}^{-3}$. For a direct-bandgap absorber material like CdTe, open-circuit voltages of $>1 \text{ V}$ are possible if every aspect relating to the potential can be ideally optimized. This is mathematically evident from the equations given below regarding open circuit voltage. For an n^+p junction solar cell made on a p-type absorber (base) material with dopant density N_A , the voltage generated depends on the separation of fermi levels on the p- and the n-side of the junction under illumination, given by the carrier concentrations as: [47]

$$qV_{OC} = E_{Fn,1} - E_{Fp,2} \quad (1-16)$$

$$\therefore V_{OC} = \frac{kT}{q} \left[\ln\left(\frac{n_p}{n_{p0}}\right) + \ln\left(\frac{p_n}{p_{n0}}\right) \right] \quad (1-17)$$

Considering negligible absorption in the thin wide-band-gap n-type CdS emitter layer:

$$p_n = p_{n0} \quad (1-18)$$

$$kT \ln\left(\frac{p_n}{p_{n0}}\right) = 0 \quad (1-19)$$

$$n_{p0} = \frac{n_i^2}{N_A} \quad (1-20)$$

And $n_p \cong \Delta n_p$, light generated carriers

$$V_{OC} = \frac{kT}{q} \ln\left[\frac{N_A \Delta n_p}{n_i^2}\right] \quad (1-21)$$

These equations show that the open circuit voltage is dictated by the fermi-level splitting across the junctions and can be increased by either increasing the CdTe doping

N_A or the excess minority carrier density Δn e.g. through increasing the minority carrier lifetime. Thus, the challenge from a technological or materials processing perspective is to increase the doping while maintaining sufficiently high carrier lifetimes.

From the above set of equations, it can be said that the photovoltaic device open circuit voltage, V_{OC} , can be optimized by improving any of the several aspects routinely encountered in real devices, specifically for polycrystalline thin film solar cells such as:

1. low minority carrier lifetime (τ) arising from low material quality comprised of bulk defects
2. recombination at the different interfaces: (low surface recombination velocity)
 - i. between CdTe/CdS
 - ii. between CdTe/back contact
 - iii. between CdS/TCO
3. non-ohmic contacts (front and/or back)
4. lack of detailed understanding of grain boundary carrier transport (primarily in CdTe)
5. low majority carrier concentration, i.e., low doping

Several methods have been employed in CdTe technology over the last decade to push device V_{OC} to meet predicted limits—reducing the thickness of CdTe layer to reduce the recombination volume [45], exploring alternative contacts to reduce the blocking barrier at the back, [45], [48], [49] studying the carrier transport across grain boundaries [50], [51]. Extrinsic doping in CdTe single crystals has been studied extensively over many decades and is discussed in detail in the reports by Zanio [52], Kröger [53] and Strauss [54]. To achieve doping, incorporation of group III and V elements to substitute for Te and Cd respectively in single crystal CdTe during crystal

growth were studied. Indium and gallium have yielded up to $2 \times 10^{18} \text{ cm}^{-3}$ [54]. Shallow acceptor level densities of up to $6 \times 10^{17} \text{ cm}^{-3}$ were reported for phosphorus doping for vertical Bridgman growth [55]. With concerns of challenges regarding lack of adequate control in polycrystalline material growth, and compensation from oppositely charged grain boundaries, extrinsic doping in thin film polycrystalline CdTe has been relatively unexplored thus far [35].

Elemental doping has been demonstrated in epitaxial and single crystal CdTe before, through *in-situ* growth incorporation (of group I and V elements), coevaporation (of P and As) and *ex-situ* diffusion into polished wafers, as discussed in Section 1.2.4. However, these methods are achieved using ultra-high purity materials at very slow rates using expensive equipment, not suitable for PV manufacturing. Polycrystalline CdTe devices were only studied theoretically for extrinsic p-type doping, reported by Wei *et al.* in 2002 [56]. This suggests Sb_{Te} defect formation enthalpies to be as high as 1.72 eV, which were, however, not experimentally validated. A 1 V V_{OC} on p-type CdTe single crystals was recently demonstrated using extrinsic doping with group V elements [57].

1.2.6 Thesis statement relating to CdTe doping:

This work is based on exploring *in-situ* extrinsic doping of polycrystalline CdTe with group V elements for cadmium substitution (X_{Cd}) to improve the carrier concentration as a route to realizing the potential for improvement in device V_{OC} . Specifically, this dissertation seeks to employ electrical characterization techniques of photovoltaic devices processed with antimony and other group V elements as dopants, as a means to understand the device behavior and explore their defect profiles. Using group V elements including N, P, As and Sb for thin film CdTe solar cells was reported

by McCandless *et al.* [58], and Colgrove *et al* [89] laying a theoretical and practical foundation to the work presented in this dissertation. Sb was down-selected as a promising candidate for substitutional doping with an expectation for high doping efficiency (discussed in detail in Chapter 5) following an initial survey of the aforementioned group V elements. High doping efficiencies can be translated to a low fraction of unwanted species that may contribute to trapping defects and scattering sites, limiting bulk minority carrier lifetime.

1.2.7 Dissertation Outline

Chapter 2 discusses development of a model to efficiently couple a PV source with an electrochemical load and presents the experimental results from the implementation of a large-area CO₂ PV-EC in collaboration with Prof. Feng Jiao's group from UDel Center for Catalytic Science and Technology. Chapters 3 and 4 discuss the extension of this model to simulate the field performance of PV-EC devices, which is used to explore the benefit of employing power electronic devices with PV-EC's. While Chapter 3 discusses the application of this annual generation model to the CO₂ PV-EC discussed in Chapter 2, Chapter 4 presents the results of this model applied to a hypothetical MW-scale H₂O PV-EC made using commercial c-Si solar cells and proton exchange membrane (PEM) water electrolyzers.

Chapter 5 details the process sequence of making Sb-doped polycrystalline CdTe thin-film solar cells, along with different device characterization techniques used to analyze devices. Chapter 6 discusses different activation treatments employed on Sb-doped devices to explore their effect on device performance and the results from the device characterization and analysis techniques employed to understand the loss mechanisms in these devices.

Chapter 7 presents a discussion of all the results from this work pertaining to PV-EC devices and CdTe:Sb solar cells, and proposes routes for future work. The results presented in this work, and to other contributions not directly pertaining to the studies reported here, are also available as scholarly articles given below: [59], [60], [61], [58], [62]

58. Sriramagiri, G.M., Ahmed, N., Luc, W., Dobson, K.D., Hegedus, S.S. and Jiao, F., 2017. "Toward a Practical Solar-Driven CO₂ Flow Cell Electrolyzer: Design and Optimization." *ACS Sust. Chem. & Eng.*, 5(11), pp.10959-10966.
59. Sriramagiri, G.M., Ahmed, N., Luc, W., Dobson, K., Hegedus, S.S., Jiao, F. and Birkmire, R.W., 2017. "Design and Implementation of High Voltage Photovoltaic Electrolysis System for Solar Fuel Production from CO₂." *MRS Advances*, 2(55), pp.3359-3364.
60. Sriramagiri, G.M., Luc, W., Jiao, F., Ayers, K.E., Dobson, K.D. and Hegedus, S., 2019. Computation and assessment of solar electrolyzer field performance: comparing coupling strategies. *Sustainable Energy & Fuels*, Oct 2018
61. McCandless, B.E., Buchanan, W.A., Thompson, C., Sriramagiri, G., Lovelett, R., Duenow, J., Albin, D., Colegrove, E., Moseley, J., Moutinho, H., Harvey, S., AlJassim, M., Metzger, W., "Overcoming Carrier Concentration Limits in Polycrystalline CdTe Thin Films with In-situ Doping" *Scientific Reports*, Oct 2018
62. Ahmed, N., Zhang, L., Sriramagiri, G., Das, U., & Hegedus, S. "Electroluminescence analysis for spatial characterization of parasitic optical losses in silicon heterojunction solar cells". *Journal of Applied Physics*, 123(14), 143103.

Chapter 2

MODELING AND IMPLEMENTATION OF LARGE-AREA CARBON DIOXIDE PV-EC

This chapter discusses the design and implementation of a solar assisted carbon dioxide electrolyzer made using a flow-cell CO₂ electrolyzer from Prof. Feng Jiao's group at University of Delaware's Chemical and Biomolecular Engineering Catalysis Center. This CO₂ flow-cell electrolyzer was independently designed and optimized by Wesley Luc *et al.* for operation using a DC power supply. As discussed in the previous chapter, many reported PV electrolysis and PEC devices employ extremely small area electrodes and/or expensive multijunction photoelectrodes, neglecting the practicality aspect. Realizing the potential of making a practical, large-area, closed-loop PV electrolysis system for CO₂ reduction using this electrolyzer with commercially available high-efficiency solar cells, an optimization procedure was proposed to maximize the power transfer, treating the electrochemical cell as an electric load to a PV array. In this chapter, this optimization procedure will be discussed in brief detail, along with the individual components used and the results obtained from implementation of this circuit. A more detailed description of the load-matching procedure and its implementation is provided in Appendix B.

Figure 2-1 shows a schematic of the proposed PV-electrolysis system, where an independently operating custom-built solar array drives a directly-connected flow-cell electrolyzer. The following sections describe the individual components of the PV-electrolyzer device.

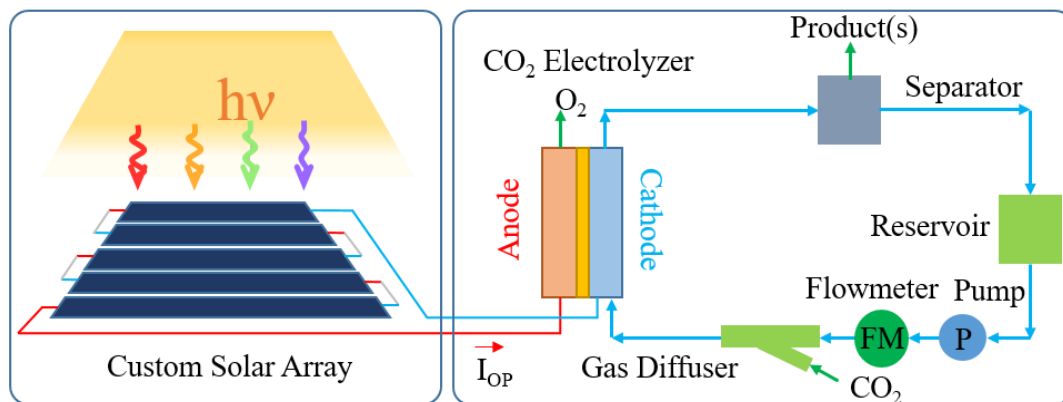


Figure 2-1: Schematic of integrated photovoltaic and CO₂ electrochemical setup. I_{OP} and V_{OP} measurement meters not shown

2.1 Description of Jiao Group's CO₂ Electrolyzer

This section describes in brief detail the flow cell CO₂ electrolyzer prepared by Wesley Luc *et al.* from Dr. Jiao group. The electrolyzer employed in this work is a sandwich-type flow-cell reactor comprising a large-area 25 cm² nanoporous silver (np-Ag) cathode and an iridium-coated catalyst membrane (Ir-CCM) anode as described in [63], synthesized using a modified de-alloying procedure. [64] The full cell is operated between 2.4 to 3.0 V in different configurations, including all the voltage losses *within* the device due to internal resistance, transport and kinetic limitations. The advantage of using nano-structured surfaces for catalysts to facilitate efficient electrocatalytic conversion of CO₂ is well-studied in literature. [65] Consequently, the porous structure of the cathode used here is expected to significantly enhance the surface area for the catalytic reaction, while the curved internal surface helps in generating a large number of highly active step sites for CO₂ conversion.[64] The iridium anode was selected for its capability of operating at near-neutral pH conditions in aqueous solution.

2.2 Designing the Photovoltaic Power Source

Commercially available, ~20% efficiency, SunPower® Maxeon C60™ half-sized (~70 cm²) crystalline silicon photovoltaic (PV) cells were chosen for the power source. Rated at 40 mA/cm² under standard sunlight (100 mW/cm²), these interdigitated back contact (IBC) commercial silicon solar cells have the highest current density (J_{SC}) and efficiency of those available on the market for terrestrial deployment. Since all contacts are processed on the rear of the device, the current generated is maximized by eliminating shading-associated optical losses on the front. The cells were connected in series using commercial tabbing methods. The number of cells in series was determined by analysis described in Section 2.5. Each cell was measured individually for its I-V behavior after tabbing, measured using OAI® solar simulator at IEC, under standard testing conditions, given in Figure 2-2. A small increase in series resistance (R_S) which occurred due to the tabbing interconnection was characterized and addressed in the model. Details about implementing this in the model are given in Section B.5.1.

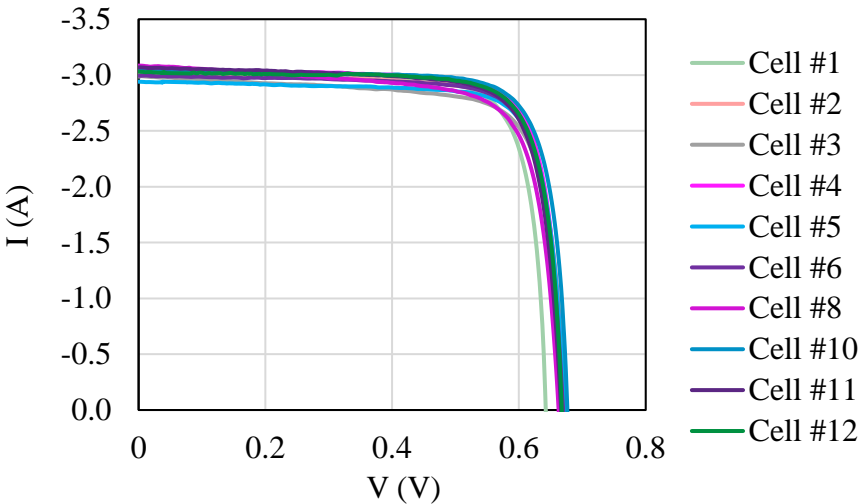


Figure 2-2: Measured I-V curves of c-Si solar cells under OAI® solar simulator at IEC

2.3 Solar Simulator Construction for Illumination Source

The solar cells were characterized individually under a calibrated AM1.5G class AAA simulator made by OAI, that illuminated up to 15x15 cm² area. However, to achieve larger area illumination of the array, a home-made solar simulator, incorporating eight 150 W GE halogen light bulbs, was constructed, shown in Figure 2-3. All the lamps are connected to a rheostat to control the input power and, hence, the light intensity output. Four lamps were attached to a rigid rail that could be raised to a desired height to adjust the light intensity variation and uniformity. The light intensity calibration is achieved by tuning the input power to the system to obtain the required short circuit current (I_{SC}) output of the array based on the simulator value of I_{SC} . For an array made with 5 solar cells of known I-V characteristics, the power to the four lamps was adjusted to achieve an array I_{SC} equal to the lowest I_{SC} of the individual cells in series. The bulbs rapidly heat the cells, so a cooling system comprising a fan and a heat-sink under the stage was employed. However, there was still significant radiative heating, which heated the cells to around 40°C, beyond the standard solar cell test conditions of 25°C. This resulted in a voltage loss of 130 mV for the array which is a closer approximation to outdoor operation conditions, where the cells would typically operate at around 50°C. Since I_{SC} is relatively insensitive to temperature, no correction was made to the I_{SC} used for lamp calibration. A photograph of this solar simulator setup is given in Figure 2-3 below.

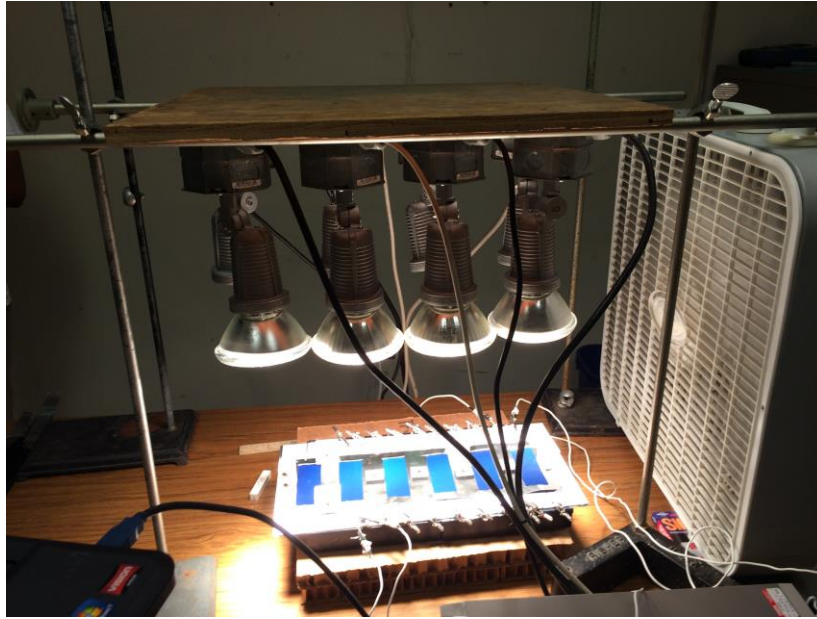


Figure 2-3: A picture of the large-area solar simulator constructed for illuminating the solar array from the bottom. The halogen light bulbs on the top are calibrated to provide 1000 W/m^2 light intensity. The fan on the right is used to cool the samples down to 25°C operating temperature

2.4 System Operation

Voltage can be adjusted in quanta of V_{MP} (the voltage at maximum power) of cells in series while current can be adjusted by reducing the illuminated cell area. Conversely for arrays with larger power rating, designed for higher current output, the output current can be adjusted by means of the number of strings connected in parallel. Experiments were designed to verify the model results and their dependence on cell area in a 5-cell configuration. The solar cell illumination area was adjusted using stainless steel adjustable-area shadow masks on each solar cell, since using masks was easier and more reversible than cutting cells into smaller areas. It is noted that using masks for area reduction did decrease measured cell efficiency due to an increasing ratio of dark to illuminated surface with small-area illumination, leading to a relative increase in dark

current, hence lower V_{OC} and fill-factor. For this reason, lower efficiencies for masked small cell areas are expected, compared to those predicted from modeling. However, this loss would not occur in a dedicated PV module design for EC applications.

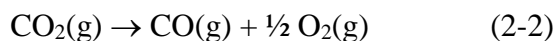
The experimental matrix was designed to include solar cell illumination areas larger and smaller than the area predicted to give the best SFE through modeling, as a proof-of-concept demonstration of the dependency of key parameters with the illumination area. In each experimental configuration (described below), the array was set up for the desired cell area using the shadow masks and connected to the electrolyzer via a Keithley 2440™ Source Meter Unit in 2-wire mode as an ammeter in series. Voltage readings were taken every ten minutes at the electrolyzer, every fifteen minutes at the PV module terminal, and the operating current (I_{OP}) was logged at 1-minute intervals. Gas products from the gas/liquid separator were fed every 15 minutes into a 1 mL sample loop of a gas chromatograph (*Shimadzu, GC- 2010*) equipped with *PLOT Mol Sieve 5A* and *Q-bond PLOT* columns to confirm and separate the CO and H₂ products.

2.5 System Design

As described in Chapter 1, the relation governing SFE, PV and electrolyzer operational parameters is key to the analysis, given here again as equation 2-1:

$$SFE = J_{OP} \times \frac{\mu_{TH}}{P_{IN}} \times FE \quad (2-1)$$

where FE is Faradaic efficiency, J_{OP} is operating current density, P_{IN} is the input solar power density with standard 1-Sun illumination of 100 mW/cm², μ_{TH} is thermodynamic voltage for CO₂ electrochemical reduction to CO, 1.34 V, for the overall reaction,



where CO and O₂ gases will be formed at the cathode and anode, respectively. The electrochemical reaction is carried out at near neutral pH to minimize competitive electrochemical formation of H₂(g) in acid and to avoid formation of stable carbonates in alkaline conditions. FE is a non-linear function of V_{OP} in electrochemical cells, representing the efficiency with which charge converts reactants into desired products—in this case, CO formed at the cathode, compared to products of competing reactions—as given in Figure 2-4. For CO₂ reduction, such competing reactions include H₂ generation at the cathode. The operating current density is calculated by dividing the measured operating current through the circuit, I_{OP}, by the total solar cell illumination area of all solar cells in series in the circuit—given as a product of the number of solar cells, N_S, and the individual solar cell illumination area, A_{PV}.

$$J_{OP} = \frac{I_{OP}}{A} = \frac{I_{OP}}{N_S \times A_{PV}} \quad (2-3)$$

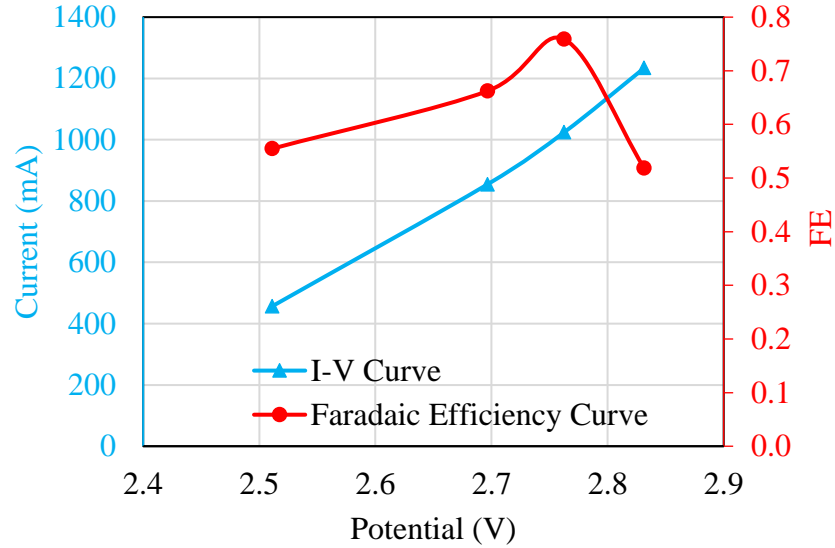


Figure 2-4: Linear voltammogram of the CO₂ electrolyzer, data measured and provided by Wesley Luc of Prof. Feng Jiao's group at UD

The number of cells in series, N_S , is determined based on the maximum power voltage, V_{MP} , of the individual devices and the desired operating voltage, V_{OP} , of the electrolyzer. When connected in series, V_{MP} of the individual devices are added to provide the overall voltage output of the array. To operate the array near its maximum power point and overcome voltage losses within the PV-electrolyzer device, a suitable over-potential must be applied in order for the electrochemical reaction to proceed. The electrolyzer used in this study [63] requires 2.75 V to drive the reaction of interest at its maximum faradaic efficiency (Figure 2-4). This voltage may seem high compared to other reported PECs and electrolyzers., but it is noted that the active areas of the electrodes in this device are at least two orders of magnitude larger than other reported

[17] lab-scale devices, justifying their higher voltage requirement. Therefore, the solar array should be designed to provide at least 2.75 V for the electrochemical reduction of CO₂ with this device. For the system used in this study, the V_{MP} of a single cell is ~0.6 V, and the electrolyzer requires at least 2.8 V. This means that the PV array should contain at least 5 cells connected in series. This is depicted in Figure 2-5 where the I-V curves of PV arrays made from 5, 6 and 7 solar cells connected in series are plotted along with the I-V curve of the electrolyzer. However, to account for additional parasitic voltage drops in the final circuit, the solar array was designed to have at least 5 solar cells connected in series, giving V_{MP} > 3.5 V to operate the electrolyzer.

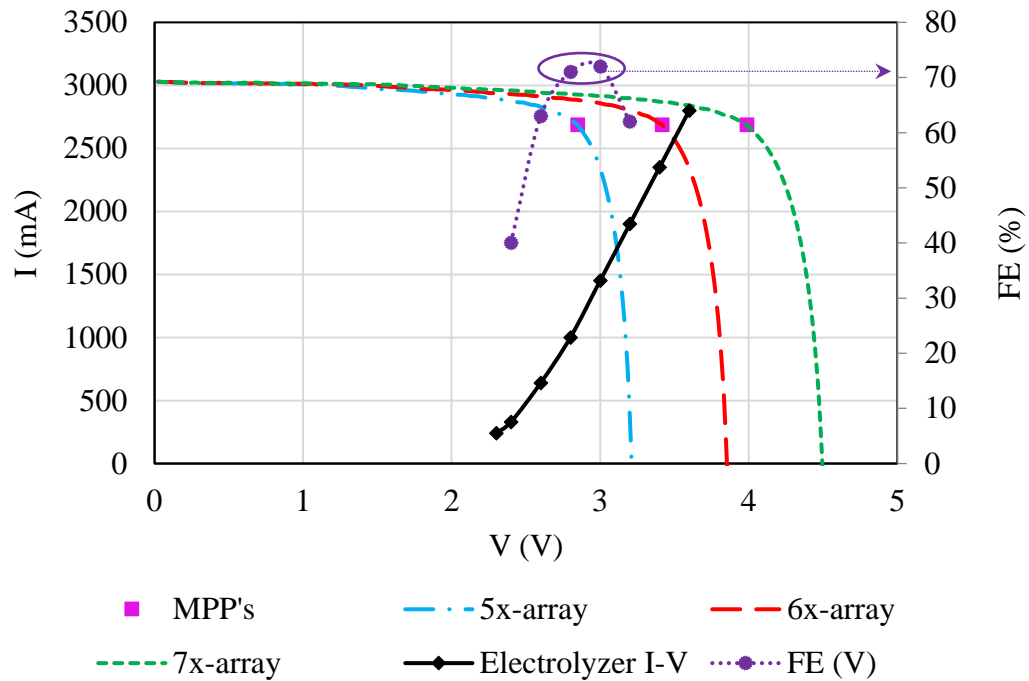


Figure 2-5: I-V curves calculated for 5-, 6- and 7-cell module configuration and the electrolyzer for comparison. The current is plotted against the left axis and the FE is plotted against the right axis, with respect to voltage. The point of intersection between a solar array I-V curve and the electrolyzer I-V predicts the operating point for the respective configuration and is compared with the solar array maximum power point. In all these configurations that use a full cell area, the maximum power current is ~3 A, much higher than the electrolyzer current of ~1A at peak FE.

2.6 Using Modeling to Determine Solar Array Configuration

The PV-EC system performance was modeled to guide the design of the system and to limit the number of experimental configurations where the number of solar cells in series and the illuminated solar cell area were the adjustable parameters. The dependence of the system's operating parameters V_{OP} and J_{OP} , on the number of cells and the illuminated cell area (the independent variables), was evaluated by calculating these dependent variables and the SFE in each case. A detailed description of this model

is provided in Appendix B. To limit the different possible source configurations, only PV arrays comprising 5 or 6 cells in series were modeled as these configurations gave V_{OP} in approximately the right range as discussed above. The I_{SC} of each of the SunPower® solar cells was $\sim 3A$, with the illumination of its total area of $\sim 77 \text{ cm}^2$, (giving a J_{SC} of $\sim 40 \text{ mA/cm}^2$). This is higher than the required operating current for the electrolyzer, which peaks at 2 A for $>3 \text{ V}$.

The measured I-V's of the individual cells were used to model the I-V performance of the array with 5 and 6 cells connected in series. The I-V plots of each of the modules for varying cell areas were constructed by scaling their measured current densities to the illuminated area. Next, the linear voltammogram of the electrolyzer was used to determine the operating point for that configuration, which is the intersection of the I-V curves of the solar module and the electrolyzer. The intersection curves for operating point determination can be seen in Figures 2-6 and 2-9 and for the 5-cell and 6-cell setting respectively. These figures show the intersection of PV and electrolyzer I-V curves, depicting the operating points in each case and the corresponding maximum power point in each of the module configurations. For best device performance, the operating point of the electrolyzer should lie as close as possible to the maximum power point of the PV component.

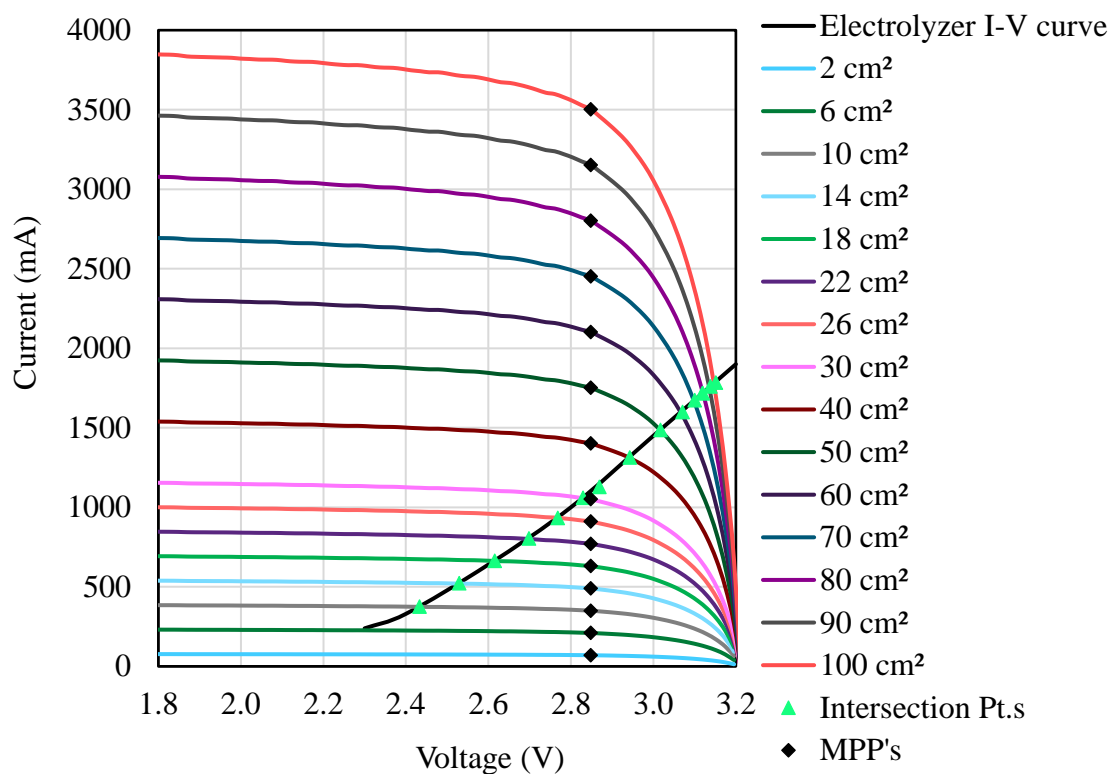


Figure 2-6: Modeled I-V curves of the 5-cell PV array under different solar illumination areas and linear voltammogram curve of CO₂ electrolyzer with Nafion XL cathode. The intersection points give the I_{OP} and V_{OP} for the device setup. The black diamond on each I-V curve highlights the PV array maximum power point

Once voltage and current values were obtained from the intersection point, the model was used similarly to obtain the faradaic efficiency for every configuration. In each of these cases, the SFE is calculated using equations (2-1) and (2-3). Using these results from the model, a plot of operating parameters, J_{OP} and V_{OP}, with varying individual solar cell area, was constructed for the 5-cell (Figures 2-7 and 2-8 respectively). Figure 2-7 shows how J_{OP} decreases and V_{OP} increases with increasing illuminated cell area. As the cell area increases, the electrolyzer curve intersects the I-

V curve at larger voltages, as is apparent in the plot of Figure 2-6, so the operating voltage increases with cell area. The operating current also increases with cell area, however the corresponding J_{OP} , calculated as the ratio of I_{OP} and *total array area*, decreases. The calculated operating voltage and current densities and the corresponding FE and SFE for PV-EC configurations for 10, 14, 25, 33, 77 cm² cell areas are given in Table 2-1. The J_{OP} of 77 cm² configuration is much smaller than the rest of the configurations shown in the table because the electrolyzer curve intersects the solar array I-V curve on the right side of the maximum power point, where the current drops more significantly with voltage. The same is true for all configurations whose solar cell area is larger than 30 cm², resulting in much smaller operating current densities as evident in Figures 2-6 and 2-7. Figure 2-8 shows how SFE—which includes the product of J_{OP} and FE (V)—peaks similar to FE (V). The experimentally determined FE (V) curve containing 4 data points was used with a spline fit to extrapolate the FE values at intermediate voltages for the model. As J_{OP} directly affects SFE, it appears at first that smaller illuminated areas will tend to provide better SFEs. However, despite V_{OP} not directly affecting SFE, it does influence FE. This dependency of SFE on J_{OP} and FE creates a tradeoff between J_{OP} and V_{OP} for identifying the configuration to maximize SFE. Thus, in each PV array configuration, with the same number of series-connected cells, the SFE peaks at a single cell-illumination area.

It is evident from these calculations that (i) directly-coupled PV-electrolyzer systems need to be carefully matched for maximum power transfer between the source and the load, and that (ii) FE (V) must be characterized carefully before experimentation as it is shown to have a major effect on the SFE. Using this modeling with the solar cell and electrolyzer components selected for this project, the best SFE is predicted to

be >7% for the 5-cell array with each PV cell having an illuminated area ~25 cm², (Table 2-1).

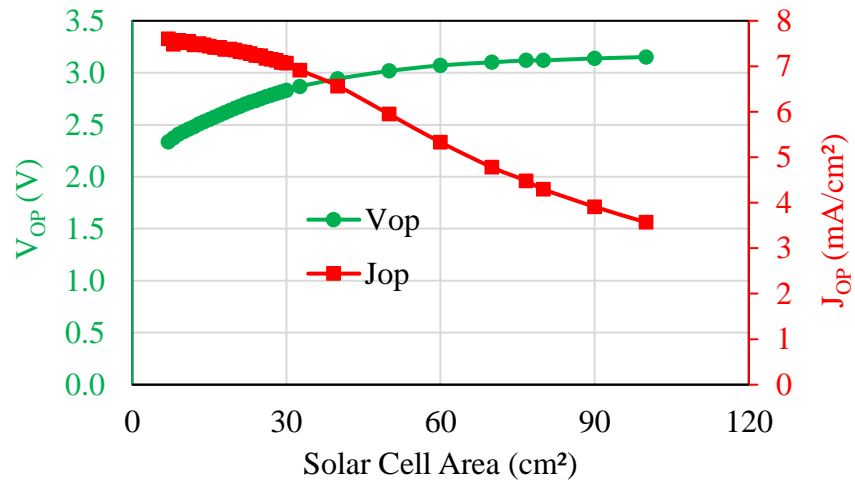


Figure 2-7: Resulting J_{OP} and V_{OP} values for configurations with varying PV cell area. J_{OP} (given as the red curve) can be seen to decrease with increasing cell area whereas V_{OP} increases with increasing cell area

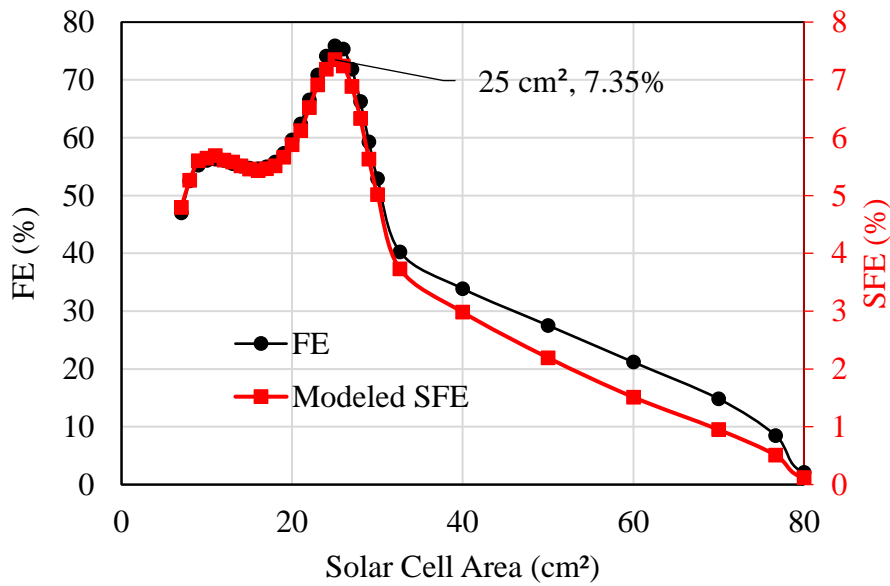


Figure 2-8: Extrapolated FE and calculated SFE for the illuminated cell areas (A) considered. Note that SFE vs. solar cell area curve follows the FE vs. solar cell area curve very closely.

Table 2-1: Results from modeling 5-cell configuration PV array. The values in red highlight the configuration giving best predicted SFE: J'_{OP} is the operating current density of individual cells

A (cm²)	10	14	25	33	77
V_{MP} (V)	2.848	2.848	2.848	2.848	2.848
I_{MP} (mA)	350	490	876	1143	2686
J_{MP} (mA/cm²)	35.03	35.03	35.03	35.03	35.03
V_{OP} (V)	2.433	2.529	2.752	2.869	3.119
I_{OP} (mA)	376	523	903	1129	1719
J'_{OP} (mA/cm²)	37.59	37.34	36.14	34.58	22.41
J_{OP} (mA/cm²)	7.52	7.47	7.23	6.92	4.48
V_{MP}- V_{OP} (V)	0.41	0.32	0.1	-0.02	-0.27
J'_{OP} -J_{MP} (mA/cm²)	2.55	2.31	1.11	-0.45	-12.62
FE (%)	56.06	55.07	75.89	40.24	8.48
SFE (%)	5.65	5.51	7.35	3.73	0.51

2.6.1 PV configuration with 6 or more cells in series

The I-V curves of a 6-cell solar array configuration, overlaid with that of the electrolyzer, are given in Figure 2-9. Figure 2-10 shows a plot of operating voltage and current density as cell area changes, and Figure 2-11 shows the predicted FE and calculated SFEs for the 6-cell configuration. As the output voltages of the solar array are higher in this configuration, the electrolyzer curve now falls on the constant-current region of the solar array I-V curve, well to the left of the array maximum power point. This results in J_{OP} remaining near-constant with varying illuminated area, as seen in Figure 2-10. This means that, in these conditions, only FE, a function of voltage, now affects device SFE, which can be observed as the overlap of the FE and SFE curves in Figure 2-11, when plotted on different linear scales. The maximum possible SFE predicted from modeling with the 6-cell configuration is 5.7%.

The same can be said for an array with 7 or more cells, which would have even higher V_{OC} (~3.5 V and greater), with the electrolyzer curve falling even further to the left, to lower voltages, of the maximum power points. More importantly, it is noted that predicted SFEs in these configurations never exceed those obtained with a 5-cell array under the same conditions. This is because with increasing number of cells in the array, the maximum power point of the PV array moves to larger voltages and further from the electrolyzer intersection point. For this reason, experimental implementation of these configurations was omitted.

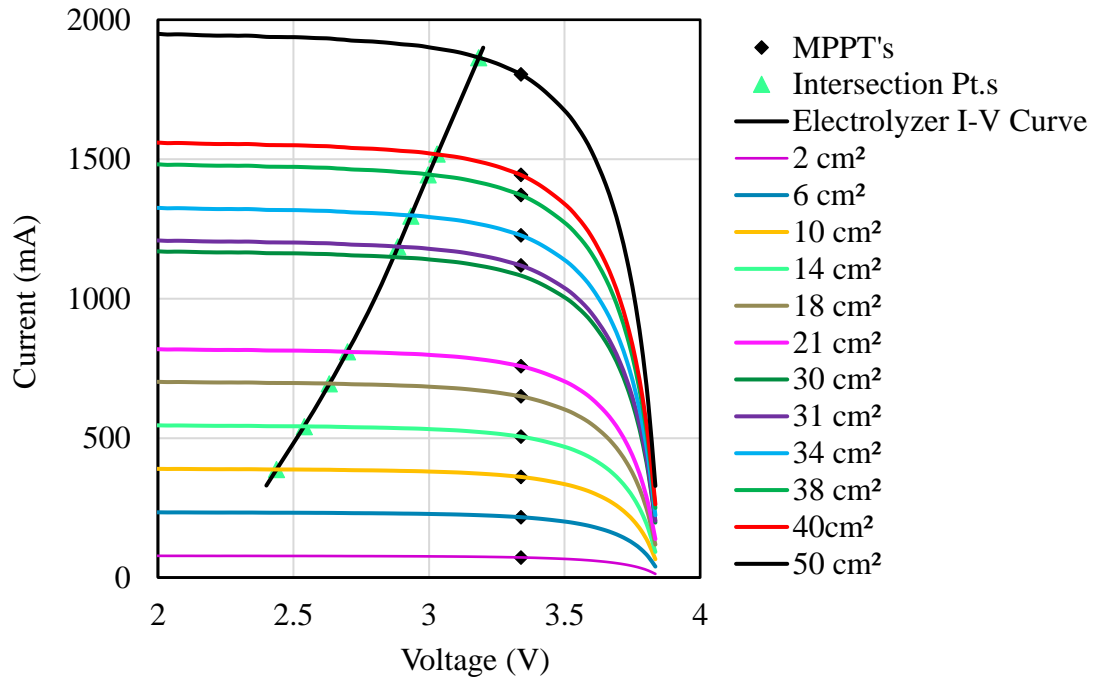


Figure 2-9: Modeled IV curves for a 6-cell array configuration with CO₂ electrolyzer linear voltammogram

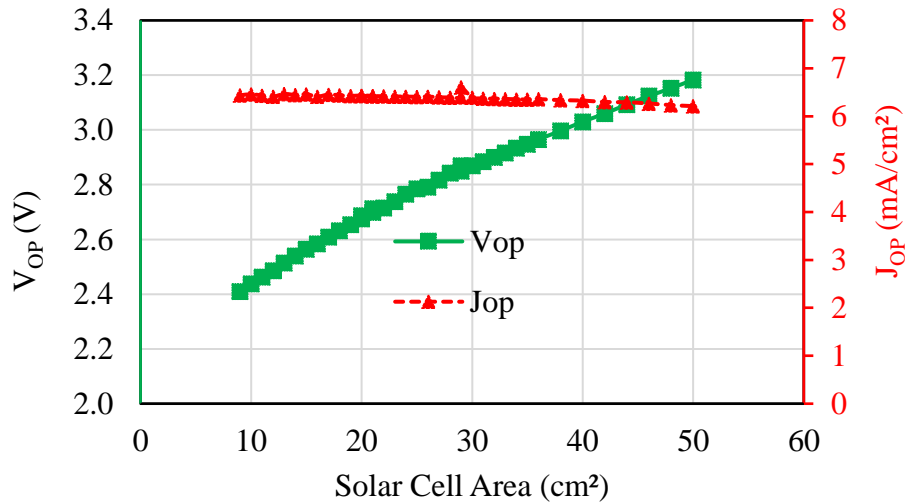


Figure 2-10: Calculated V_{OP} and I_{OP} with cell area for 6 cell PV array

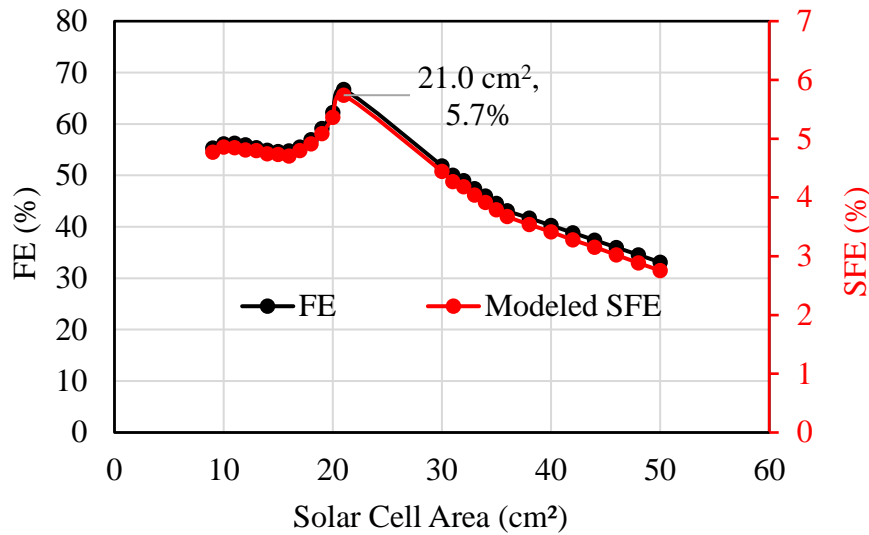


Figure 2-11: SFE and FE with cell area for 6 cell PV array.

2.7 Measured PV-EC Performance

Based on the modeling results, a 5-cell PV-driven electrolyzer setup was implemented to experimentally validate the dependence of SFE on cell illumination area, by varying it from 14 cm² to full area, using adjustable shadow masks. The full experimental setup showing the solar array, illuminated with the home-made mobile large-area solar simulator is shown in the Figure 2-12. The electrolyzer connected to the gas inlet and outlet pipes is shown in Figure 2-13. The conditions of these experiments are shown in Table 2-2: Experimental matrix involving solar cell illumination areas and the results are summarized in Table 2-3. The current readings were logged every minute in each of the configurations and are shown in Figure 2-14. The corresponding J_{OP} and V_{OP} vs. solar cell illumination area is given in Figure 2-15. The plots confirm the performance of the test system and components were stable during experiment indicating the effects of heating of the PV array to be well controlled.

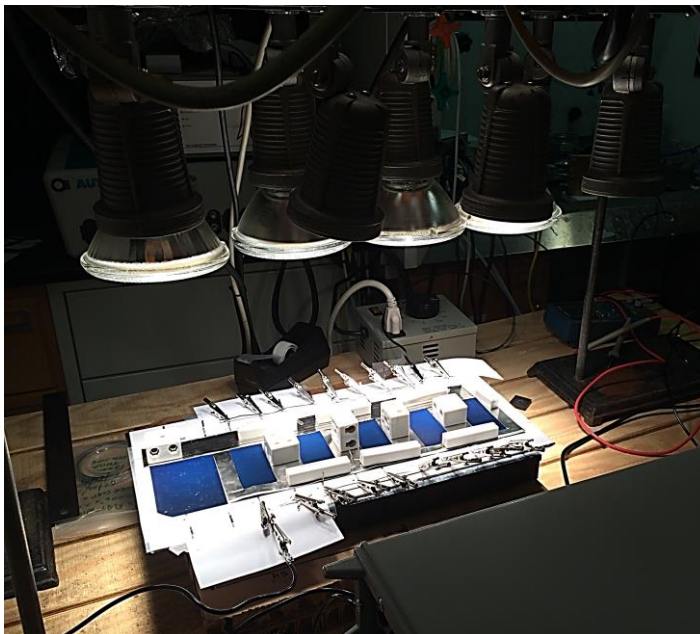


Figure 2-12: Practical experimental setup showing PV module array illuminated by the solar simulator

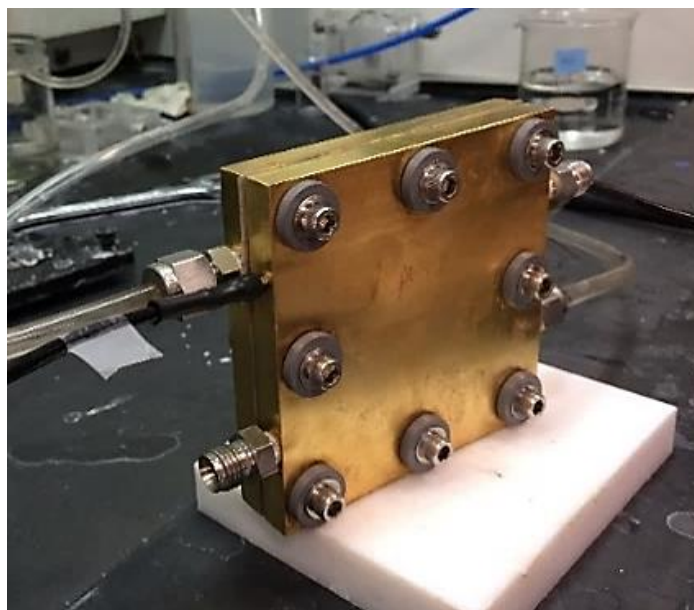


Figure 2-13: Practical experimental setup showing the CO₂ electrolyzer in the fume hood, being run by the solar simulator

Table 2-2: Experimental matrix involving solar cell illumination areas

Configuration	Mask Dimensions	PV Area Illuminated (cm ²)	Expt. Duration (hrs.)	Comment
1	4.1 cm x 3.4 cm	14	1	< Optimal PV Area
2	7.6 cm x 3.4 cm	26	1	= Modelled Optimum
3	9.6 cm x 3.4 cm	33	2	> Optimal PV Area
4	No Mask- Full Area	77	1	> Optimal PV Area

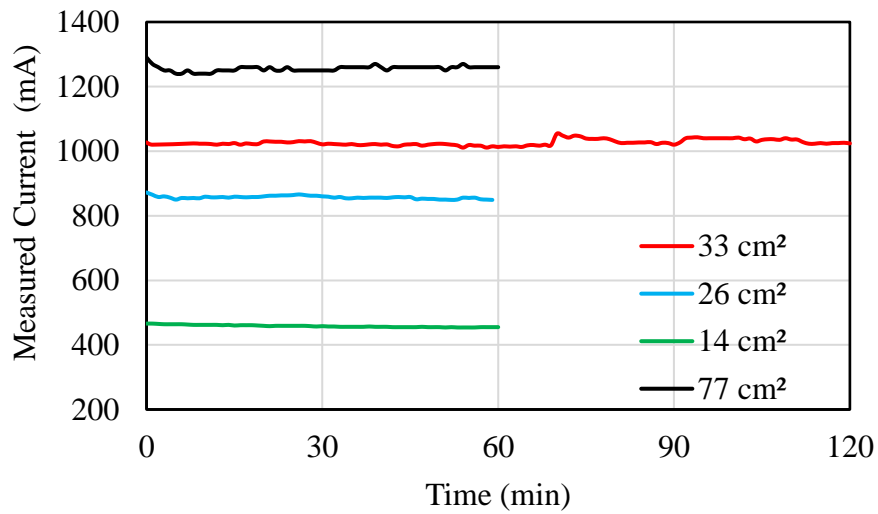


Figure 2-14: Measured I_{OP} vs. time for the configurations listed in Table 2 with different PV illumination areas in 5-cell configuration

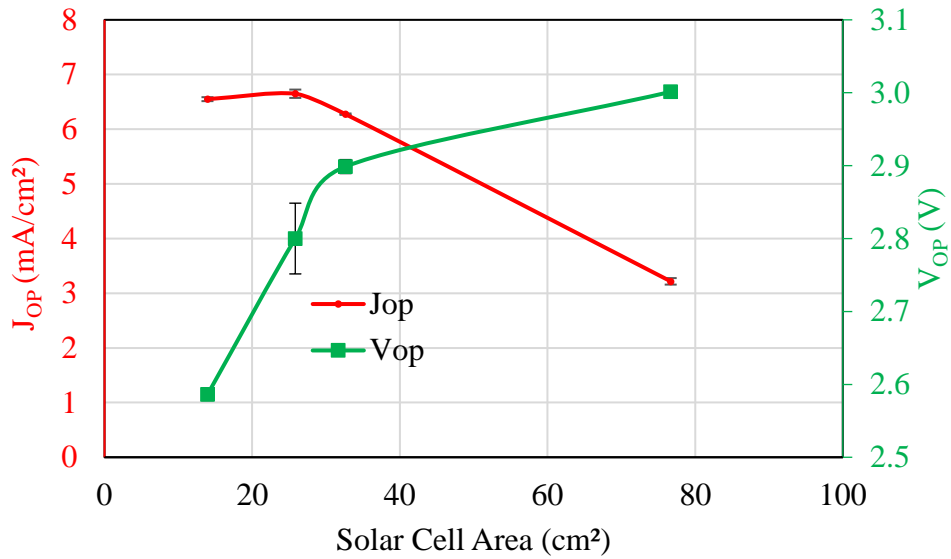


Figure 2-15: J_{OP} and V_{OP} vs. cell area. Cell area obtained from results of practical demonstration of PV-driven CO_2 electrolyzer using 5-cell array. Note that the qualitative shape of this curve agrees well with that of the predicted J_{OP} and V_{OP} vs. solar cell area, given in Figure 2-7

Figure 2-15 shows plots of each value of J_{OP} and V_{OP} measured in the circuit against the cell area, (J_{OP} is determined from measured I_{OP} from equation (2)). FE_{CO} is measured every 15 minutes for each configuration by analyzing the product gas mixture using a gas chromatograph and the average and peak values are listed in Table 2-3 and Figure 2-16 shows FE measured at ~15 min intervals. Figure 2-17 shows the measured FE (peak values) and the resulting SFE of each of the experimental conditions, plotted against the cell illumination area. The measured currents varied from the computed values due to voltage discrepancies between the terminals of the PV array and the electrolyzer. The determined optimum area has shifted from 25 cm² to 33 cm² due to these voltage losses in the circuit. A peak SFE of 6.5% was obtained with the 33 cm² area of illumination in the 5-cell array, approaching the predicted value of 7.3%.

Table 2-3: Summary of experimental results, V_{PV} is the voltage at the PV module, V_{EC} is the voltage at the electrolyzer, ΔV is the difference between the PV voltage and the electrolyzer voltage, R is the resistance calculated from the differences in voltage between PV and electrolyzer/ operating current I_{OP} , J'_{OP} is the operating current density *per cell* and J_{OP} is the overall operating current density and actual value used in calculating SFE, $COFE$ is FE of the reaction

Illuminated PV Area (cm²)	V_{PV} (V)	V_{OP} (V)	$\Delta V = V_{PV} - V_{EC}$ (V)	R (Ω)	I_{OP} (mA)	J'_{OP} (mA/cm²)	J_{OP} (mA/cm²)	CO FE (%)	SFE (%)
Average Values (averaged over the experimental duration)									
14	2.586	2.511	0.075	0.164	457	32.75	6.55	55.46	4.87
26	2.800	2.697	0.103	0.121	855	33.08	6.62	66.24	5.87
33	2.899	2.763	0.137	0.133	1024	31.37	6.27	75.89	6.38
77	3.001	2.832	0.170	0.137	1234	16.09	3.22	51.86	2.24
Peak Values (Corresponding to maximum of all FE values measured over the experimental duration)									
14	2.589	2.510	0.079	0.173	456	32.71	6.54	58.31	5.11
26	2.800	2.690	0.110	0.128	861	33.32	6.66	67.87	6.06
33	2.900	2.770	0.130	0.127	1021	31.28	6.26	78.06	6.54
77	3.001	2.831	0.170	0.137	1240	16.17	3.23	52.72	2.28
Predicted Values from Modeling									
14	2.529	2.529	0	0	522	37.34	7.47	55.46	5.55
26	2.768	2.768	0	0	932	35.86	7.17	75.89	7.29
33	2.869	2.869	0	0	1128	34.58	6.92	51.86	4.81
77	3.005	3.005	0	0	1463	19.08	4.48	51.86	3.11

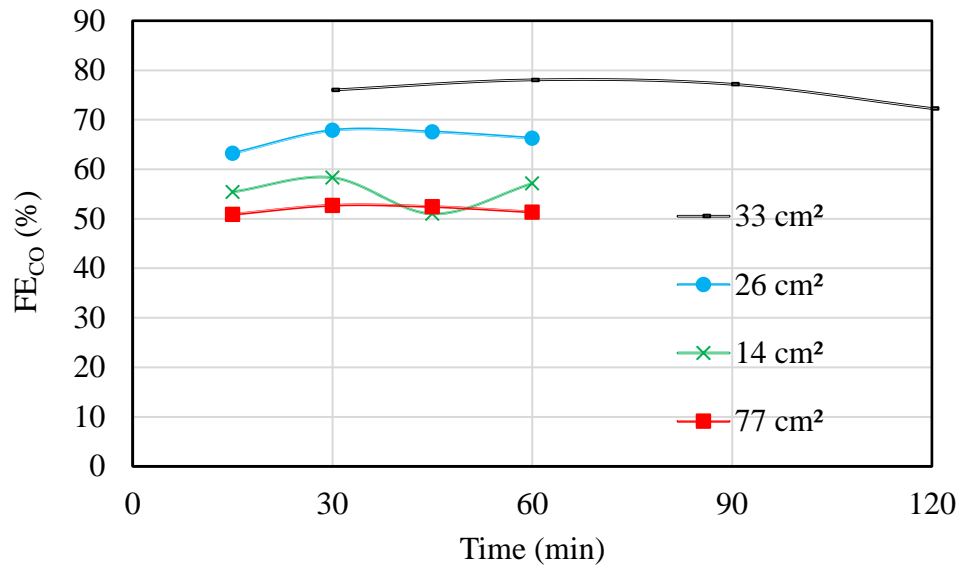


Figure 2-16: Measured FE_{CO} vs. time for the configurations listed in Table 2 with different PV illumination areas in 5-cell configuration

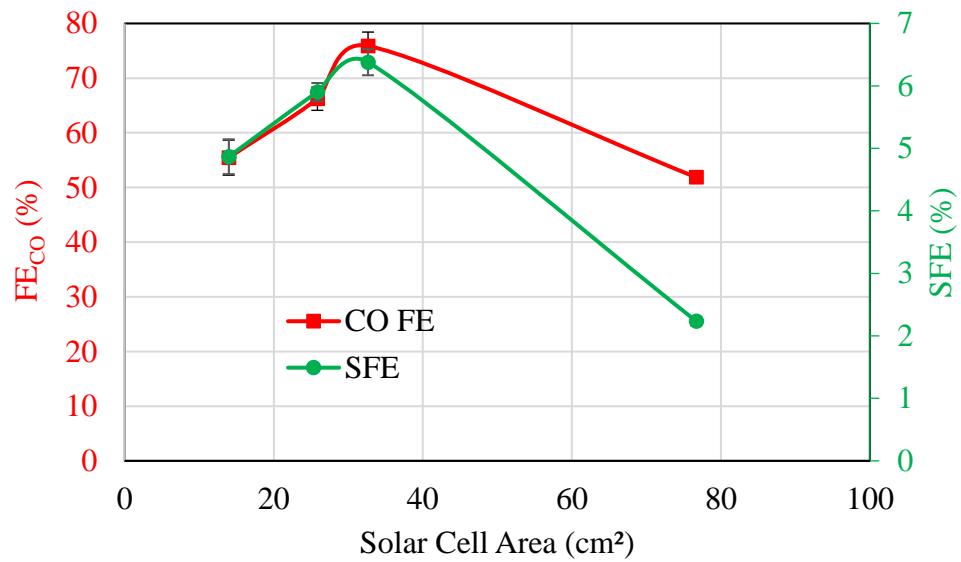


Figure 2-17: Measured FE and the corresponding SFE plotted against solar cell illumination area

2.8 Comparing Calculated and Measured Results:

The solar array I-V curves calculated using our model without additional losses were compared with those measured under the solar simulator, in Figure 2-18, for the case of 33 cm² illumination area. As mentioned in Section 2.3, the measured I-V behavior of the solar array is expected to be slightly inferior to the predicted results, since the array suffers from voltage losses during experiment due to higher cell temperatures under the solar simulator (which leaves the cells working at ~40°C due to radiative heating), and parasitic series resistance (R_s) from wiring and tabbing. Generally good agreement between the as-measured and the modeled I-V curves is apparent in Figure 2-18. But when the x-axis is expanded beyond the inflection point / the maximum power point in Figure 2-19, it can be seen that the measured curve is at times 0.1 V (or ~3%) less than the modeled I-V curve consistent with temperature and R_s losses. Successively correcting for R_s and temperature losses moves the measured curve much closer to the modeled curve. This agreement validates the procedure used here for modeling the solar array I-V curve generation and shows the relative impact of realistic losses.

Additional voltage drops in the circuit incurred due to the electrolyzer set-up, are incorporated back into the model to confirm its accuracy. These drops incurred due to parasitic circuit resistances affected the experimental results more significantly than the I-V curve discrepancies described above. These were incorporated into the analysis by reproducing the load curve with a resistor of the measured circuit resistance in series, and the calculated SFE values were very close, within 3% error, to those measured on the experimental system. A detailed description of incorporating parasitic resistance in the model is provided in Section B.4.1 of Appendix B. The results are summarized in Table 2-4: Average values of SFE predicted from modeling when corrected for

measured parasitic circuit resistive losses and confirm the validity of the developed model.

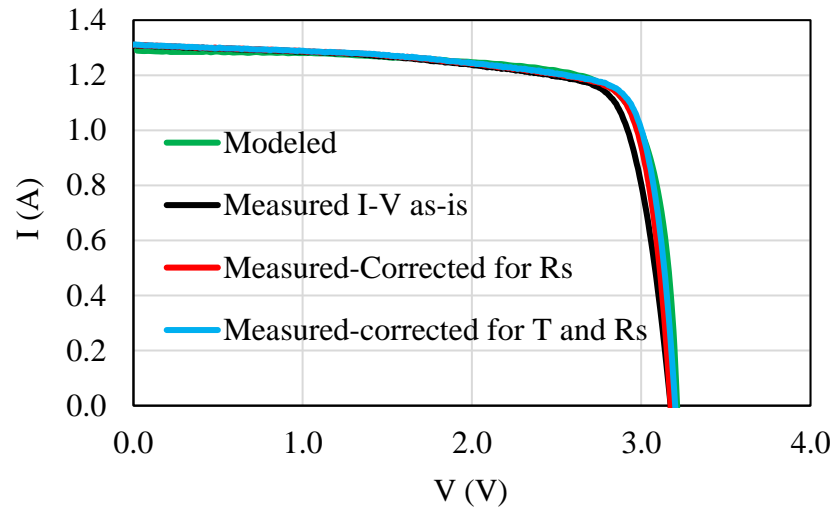


Figure 2-18: Comparison of solar-array I-V curves generated from the load-matching model, with those measured under the home-made solar simulator

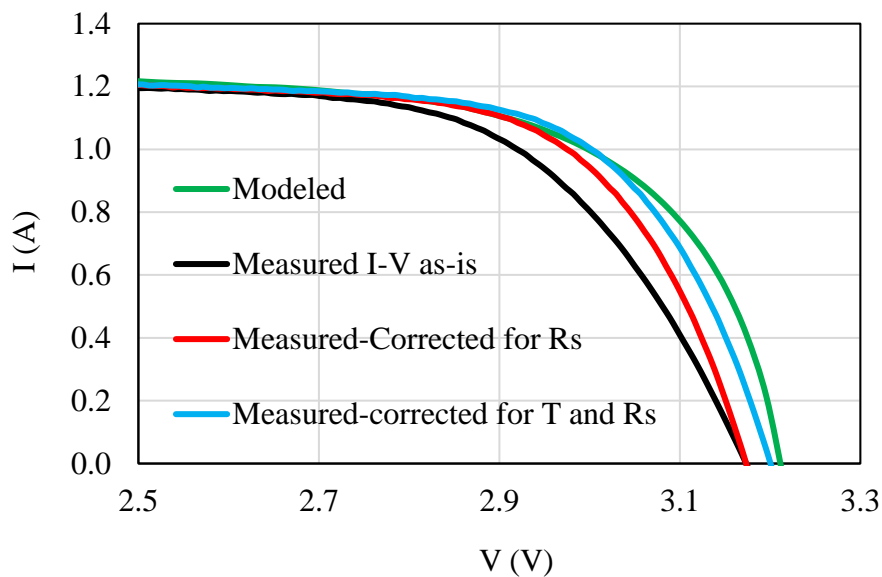


Figure 2-19: Comparison of solar-array I-V curves generated from the load-matching model, with those measured under the home-made solar simulator. Here, the x-axis is expanded to emphasize the difference in the curvature of each of the plots. This shows that the model used in this work is reliable, when empirical losses are incorporated

Although the practical 2-electrode system used in the CO₂ electrolyzer in this work suffers from significant voltage drops due to parasitic circuit resistances, it is noted that this is one of the very few large-area solar electrolyzers to be reported. The single electrode Tafel performance of np-Ag cathode used in the device, is exceptional and comparable to the best electrode technologies in the literature, [64] holding promise for better full-size PV-EC devices in the future.

Table 2-4: Average values of SFE predicted from modeling when corrected for measured parasitic circuit resistive losses. $\Delta\text{SFE}(\% \text{abs})$ is the difference between the modeled and predicted SFE given in absolute percentage points, $\Delta\text{SFE}(\% \text{rel.})$ is the same parameter gives as a relative percentage

Area (cm ²)	Modeled SFE (%) with ΔV correction	Measured SFE (%)	$\Delta\text{SFE}(\% \text{abs.})$	$\Delta\text{SFE}(\% \text{rel.})$
14	5.00	4.87	0.13	2.60
26	5.96	5.87	0.09	1.54
33	6.40	6.38	0.02	0.31
77	2.23	2.24	-0.01	-0.33

2.9 Summary of Proposed Optimization Procedure:

The modeling process performed in this work that led to successful prediction of SFE values, verified through experimentation, can be concisely summarized as follows. To optimize the SFE of a PV-EC system, where an extra degree of freedom is available in terms of the current via the solar cell area, we need to strike a balance between the interaction of J_{OP} , which is a function of cell area, and FE, which is a function of V_{OP} . Based on this competition, the ‘best’ solar cell area is that which produces sufficient voltage, current density and the respective FE whose mutual optimization gives the peak SFE for the system. The falling J_{OP} and rising FE with increasing cell area might set a trade-off, until the FE(V) curve reaches its inflection point, where both the parameters begin to decrease. A converse method can be employed in cases where the solar cell area is fixed but the electrode surface area is adjustable. In that case, if it is safe to assume that the I-V curve of the electrolyzer scales linearly with the surface area, we can balance the trade-off between the J_{OP} (A_{PV}) and FE (V). Voltage drops arising due to several parasitic contact and cable resistances, can

also be incorporated in modeling, after they are measured from initial connection. This has been shown to give accurate predictions of SFE's within 3% relative error.

2.10 Potential for High SFE's with Multijunction Tandem Solar Cells Under Concentration:

A water electrolysis system having the highest-reported SFE of 30%, was recently demonstrated using a InGaP/GaAs/GaInNAsSb triple-junction solar cell under 42x concentration to drive two polymer electrolyte membrane electrolyzers in series. [3] We now show that SFEs as high as 14%, after correcting for resistive losses, are possible for CO₂ electrolysis with the same high efficiency triple junction solar cell technology as in reference [3] but driving the flow-cell electrolyzer described in this work. Using the modeling procedure demonstrated above, the I-V parameters of the resulting system, i.e., the multijunction tandem solar cell under concentration from reference [66] driving the flow-cell electrolyzer described in this work, were modeled for a few cell areas as given in Table 2-5. Calculating the resulting J_{OP} in each case and incorporating the FE (V) of our electrolyzer, the optimum solar cell area for this combination was determined to be 1.4 cm², where the FE peaks to 78% at 2.7 V, giving an SFE of 14.2%. Further improvement of SFE in beyond that predicted here should be possible through independent development of the various components of the electrochemical cells, viz., electrolytes, electrode technologies, ion-separation membranes etc. However, note that the high efficiency III-V concentrator system is significantly more expensive than the commercially available Si cells used here.

Table 2-5: SFE's calculated for a PV-EC designed using the flow cell electrolyzer discussed in this work with high efficiency multijunction tandem cells under 42x concentration, as reported in reference [3]

Area (cm²)	V (V)	Resistive loss included, theoretical I (mA)	J_{OP} (mA/cm²)	FE (%)	SFE (%)
1.0	2.337	169	4.03	47.01	2.54
1.4	2.761	810	13.53	78.00	14.15
2.0	2.953	1098	13.07	33.88	5.93
4.0	3.120	1341	7.98	8.48	0.91
6.0	3.151	1397	5.54	1.00	0.07

2.11 Conclusion

We have shown that developing a solar fuel production system using the PV-EC architecture facilitates independent design of the power source and electrolyzer components. This eliminates the challenges of materials compatibility and excess optical losses associated with integrated PEC's. The primary benefit is that PV-EC enables optimization of the power-transfer between the PV and the EC systems, targeting SFE maximization using rigorous design and modeling. A directly-coupled PV-driven large-area CO₂ flow-cell electrolysis system was designed, modeled, optimized and implemented in this work using commercial silicon solar cells with sandwich-type flow cell electrolyzer. The predicted trend of SFE dependence on illuminated cell area based on modelling was verified with experiments, designed to span from sub-optimal to beyond optimal cell areas. Unexpected voltage drops in the circuit decreased the peak SFE and shifted the best cell area to higher values than predicted from initial calculations. Modeled results were then corrected by incorporating measured parasitic circuit resistance and exhibited an excellent agreement

with the experimental results to within <3% error. A proof-of-concept modeling and optimization procedure was thus presented for the proposed new approach of PV electrolyzer design and a 6.5% peak SFE was demonstrated, challenging that of the current best CO₂ PV-electrolyzers reported in literature. Much of this work was published in ACS Sustainable Chemistry and Engineering as the largest-area CO₂ PV-EC to be reported. [60]

Chapter 3

ANNUAL GENERATION MODEL FOR SOLAR ELECTROLYZER FIELD PERFORMANCE, APPLICATION TO CO₂ PV-EC

In this chapter, a practical methodology for the analysis of PV-ECs will be provided that accounts for their total annual performance. The underlying premise of this approach is that the generally accepted figure of merit for these devices, SFE is an insufficient measure of their real field performance. Considering that SFE is measured with the device at STC—1-sun, 1000 W/m² insolation, clear sky spectrum, and 25°C operating temperature—it does not offer a comprehensive measure of system performance because actual field operating conditions are rarely close to those used for testing. A thorough understanding of PV-EC field performance under realistic operating conditions can assist in holistic device design and scalability. Here, a model is developed to compute their real-life performance using hourly variation in solar irradiance and air temperature over a one-year period. It is then applied to two systems: a previously reported bench-scale high-efficiency CO₂ PV-EC and a conceptually-designed MW-scale solar H₂O electrolysis system employing commercial solar panels and water electrolyzers. This chapter discusses the development of the annual generation model and applies the results from this model to the previously discussed CO₂ PV-EC. A more detailed description of this annual generation model is provided in Appendix C. Chapter 4 discusses the results from this model applied to the MW-scale H₂O electrolyzer. The contents of Chapters 3 and 4 have also been published in *Sustainable Energy and Fuels*. [61]

3.1 Figure of Merit for Practical Consideration of PV-EC's:

The use of SFE has come to be generally accepted as the primary device performance figure-of-merit for devices reported in the literature. For practical solar fuel devices as discussed here, an additional term, 'collection efficiency', η_{coll} , should be added, representing the efficiency with which product gases are collected after separation, as shown in equation 3-1. This term highlights the importance of effective product gas separation after electrolysis, preventing any crossover. This parameter was set to be 1 in the calculations performed for this work for simplicity.

$$SFE = J_{OP} \times \frac{\mu_{TH}}{P_{IN}} \times FE \times \eta_{coll} \quad (3-1)$$

Very few reports discuss performance of solar electrolysis devices under conditions different from STC. [67], [68] A solar electrolysis device is effectively a source-load combination, and while the load's electrical behavior (the current-voltage curve) remains constant with changing atmospheric conditions, the PV output is very dependent on insolation and operating temperature. This behooves the designer to ensure maximum power transfer between the energy generator and the electrolysis components at all times.

3.2 Power Conditioning Devices as a Coupling Strategy

Optimal power delivery with changing insolation can be achieved through a decoupled PV-EC architecture by employing electronic power conditioning between the source and the load, [69,70] such as switch-mode DC-voltage regulators with maximum power point tracking (MPPT). [71] Such a device would continuously adjust the operating voltage on the solar array I-V curve to keep it at the MPP despite changes in insolation and temperature, and convert that power to a voltage and current suitably matched to the electrolyzer. These two functions, MPPT at the input and V or I

regulation at the output, are very similar to charge controllers already widely used for PV battery charging. [72] The key difference is that the output would be optimized for the needs of an electrolyzer not a battery. The controller can be designed to digitally control the voltage and current delivered to its electrolyzer load so as to accommodate for any specific requirements such as to ensure maximum gas output for any operating condition (especially when the faradaic efficiency of the electrochemical cell has a sensitive dependence on its operating voltage), to ensure a certain product gas mixture ratio, etc. The DC-power optimizer controller considered in this work traces the MPP of the solar array I-V as it changes with operating conditions and converts the power to a voltage and current that match the electrolyzer I-V curve (discussed in detail in Section 3.3.2). Another more traditional approach to couple PV-ECs for optimum power delivery would be to use inverter-connected PV-arrays to power commercial electrolyzers designed for AC (grid) (termed ‘DC-AC-DC’ conversion in this work). Since all PV inverters provide MPPT on their DC input side, this approach also ensures maximum power delivery, except for additional losses involving conversion of AC power back to DC inside the electrolyzer. It also enables the PV array to either provide energy directly to the grid or to the EC or both in parallel. This has a strong practical value which is not captured in our analysis. A schematic of a PV-EC system showing a variety of coupling configurations is given in Figure 3-1.

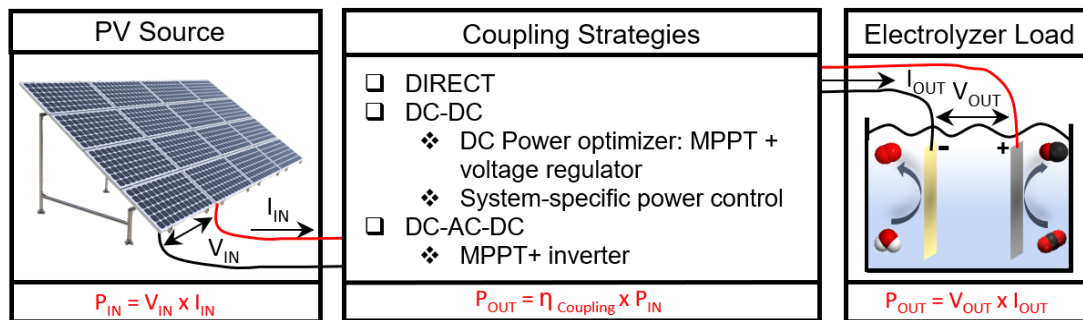


Figure 3-1: Schematic of a PV-EC system showing the different coupling strategies possible. P_{IN} is the input power generated at the solar array at voltage V_{IN} , and current I_{IN} and P_{OUT} is the power delivered to the electrochemical cell at voltage V_{OUT} and current I_{OUT} , with a coupling efficiency $\eta_{coupling}$.

Applying power conditioning devices to decoupled PV-EC's carries several other practical advantages over directly connected counterparts. These factors include: (i) addressing variable collection efficiency of electrolyzer product gases due to electrolyzer transient behavior during a typical day or over an entire year [73], (ii) controlling the CO to H₂ ratio in the case of CO₂ electrolysis systems used with Fisher-Tropsch process, (iii) concurrent operation of electrolyzer with grid-connected PV systems—which has substantial practical and technoeconomic implications besides operating the high-capex electrolyzer at a higher capacity factor (CF) than the average 4 hrs./day insolation in typical US locations, [74] and (iv) assuaging the challenges associated with electrolyzer degradation, [75] that would otherwise lead to a shift in the operating point of the PV-EC and, therefore, its coupling efficiency over time due to the shifted electrolyzer I-V curve falling off of the ‘knee’ portion (the constant current portion) of the solar array I-V curve.

In this chapter, different coupling strategies available for PV-ECs will be compared by using the generation model to calculate PV-EC annual yield with various

coupling configurations. The I-V characteristics of the source and the load are used as input, and atmospheric conditions— insolation and ambient temperature— as variables to generate hourly PV-EC product gas output and SFE. The model is set up to also incorporate power conditioning devices in the simulation to quantitatively assess the benefit they offer to the overall performance of the system. This enables a designer to evaluate the field operation of a PV-EC device, giving insight into its realistic performance rather than idealized STC performance. This model is applied to the CO₂ flow-cell PV-EC device of 6.5% SFE already discussed in Chapter 2. Using these simulations, we compare different coupling strategies available for both lab-scale device (this chapter) and MW-scale system (Chapter 4).

3.3 Model Development

3.3.1 Annual generation model- parameters incorporated

Given a PV-electrolyzer combination optimized for STC operation, the model uses as input the I-V behavior of the PV component, along with the polarization and FE curves of the electrochemical device. Meteorological data provided by NREL's National Solar Radiation Database (NSRDB) [76] was used to obtain the hourly insolation and temperature data for the specific module deployment method and location. For this work, a module installed at fixed latitude tilt in Wilmington, DE, USA (a mid-latitude location with moderate climate) was selected. Using this data, the model computes the solar array I-V curves as a function of changing solar irradiance and temperature every hour during the entire model year, using the PV I-V translation equations below.

$$T = T_{module} = T_{air} + \frac{NOCT-20^{\circ}C}{80} \times S \quad (3-2)$$

$$I_{SC}(S, T) = \frac{I_{SC,STC}}{[1+\alpha(T-25^{\circ}C)]} \times \frac{S}{1000 \frac{W}{m^2}} \quad (3-3)$$

$$\Delta V(T) = \beta(T - 25^{\circ}C) \quad (3-4)$$

$$I(V, S, T) = I(V, S_{STC}) - I_{SC,STC} + I_{SC}(S, T) \quad (3-5)$$

$$V(S, T) = [V_{STC} - \Delta V] - I(S, T)R_S \quad (3-6)$$

where T_{module} is the module temperature, T_{air} is the air temperature, $NOCT$ is the normal operating cell temperature obtained from the module data sheet, S is the insolation in W/m^2 , I_{SC} is the short-circuit current while $I_{SC,STC}$ is the short circuit current at STC, as given in the module spec sheet, α is the temperature coefficient for current, β for voltage and T is the module temperature, S_{STC} is 1-sun insolation- $1000 W/m^2$, R_S is the lumped series resistance of the module isolated from its STC I-V curve [77].

The calculated hourly solar array I-V curves are then overlaid with the electrolyzer polarization curve, giving the operating current $I_{OP}(S, T)$, voltage $V_{OP}(S, T)$, at the intersection of the plots. Using the faradaic behavior of the electrolyzer, the corresponding FE (S, T) is found, from which the hourly SFE and product gas output are computed as given in equations (3-7) and (3-8). The hourly data is then integrated to compute annual yield and annual average SFE as given in equations (3-9) and (3-10).

$$\text{Hourly SFE, } SFE(S, T) = \frac{\mu_{th} \times J_{OP}(S, T) \times FE(S, T)}{P_{Sun}} \quad (3-7)$$

$$\text{Hourly gas output } \left(\frac{g}{hr}\right), g(S, T) = \frac{I_{OP}(S, T) \times 3,600s \times FE(S, T) \times M}{q \times N \times A} \quad (3-8)$$

$$\text{Annual average SFE, } SFE_{annual} = \frac{\sum_{i=1}^N SFE(S, T)}{N} \quad (3-9)$$

$$\text{Annual gas output } \left(\frac{kg}{yr}\right), G(S, T) = \int_{t_1}^{t_2} g(S, T) dt = \sum_{i=1}^N g(S, T) \quad (3-10)$$

where M is the molar mass of the product gas in g/mole, q is the electronic charge in coulomb, n is the number of electrons required for the electrochemical reaction, A is Avogadro's number and N is the total number of *sun* hours in the model year- which in this study was >4,000.

Additionally, the model incorporates DC power optimizer devices to the PV-EC system. As described in the introduction, the suggested power optimizer device would consist of DC voltage regulators with MPPT, tailored to the specific PV-EC system. At its input, this device actively establishes the MPP on the I-V curve of the PV array despite variable insolation and temperature conditions. At its output, it shifts the voltage to deliver this power to match the electrolyzer polarization curve. This is graphically represented in Figure 3-2 using the power vs. voltage, P(V), curves of an example PV-EC system. While the MPPT adjusts the array V_{OP} to keep the solar array output at its peak on the power curve, the voltage regulator would translate that I-V point to fit on the electrolyzer P(V) curve, i.e., at the same power as the MPP (except for conversion losses related to the regulator), but at a different voltage and current point that falls on the load curve. In the case where the PV and EC devices are directly connected, the operating power point would be where the two P(V) curves intersect (red dot). The vertical distance ΔP between the ordinates at the red and the green points is the difference in the power transferred, showing the improved energy transfer with the use

of power optimizer devices over direct-coupled connections during non-standard operating conditions. When integrated over the entire model year, such hourly power differences, ΔP , provide the difference in the annual energy delivered to the electrolyzer load between the two coupling configurations. For a more realistic comparison, the efficiency of these coupling devices, $\eta_{coupling}$, should also be accounted for, although DC-DC switch-mode power converters have efficiencies exceeding 95%. [78] The I-V transfer function for the power optimizer therefore is:

$$V_{IN} \times I_{IN} = \eta_{coupling} \times V_{OUT} \times I_{OUT} \quad (3-11)$$

where $V_{IN} = V_{PV,MPPT}$ and $I_{IN} = I_{PV,MPPT}$ and V_{OUT} and I_{OUT} are the output current from the voltage regulator, pre-set to match the EC load curve.

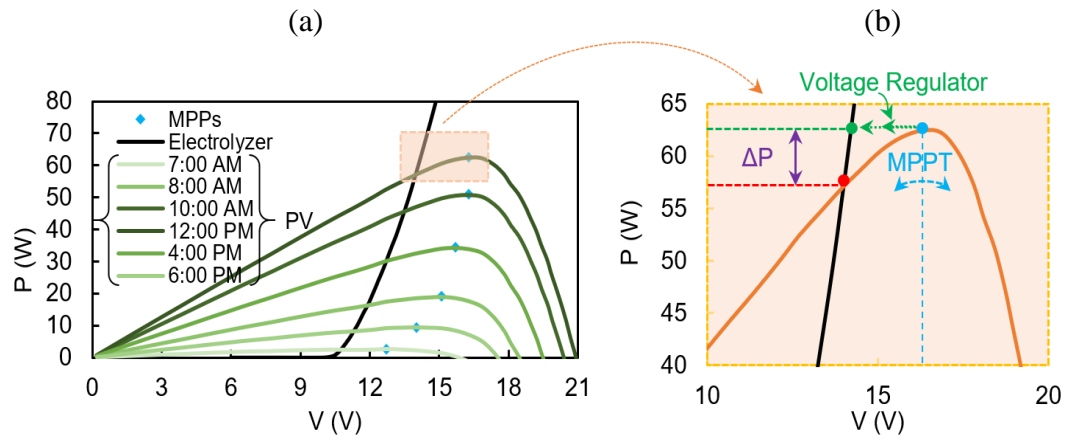
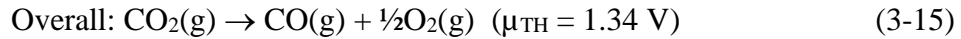
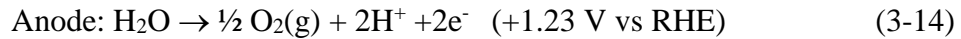
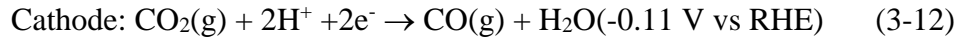


Figure 3-2: (a) Power vs. voltage curves of the PV array of an example PV-EC system for changing insolation during a day, overlaid with the power vs. voltage curve of its electrolyzer load. The MPP points are indicated by blue diamonds at peak of each curve. (b) Graphical representation of the performance of a power optimizer device comprising MPPT and a voltage regulator. The red dot represents the operating point (power and voltage) for a directly connected PV-EC, while the green dot represents the operating point in a PV-EC coupled with a DC power optimizer.

The model is developed using the above equations to compute the performance of PV-ECs coupled with power optimizer devices, facilitating their comparison with directly-connected PV-ECs. Using the final (annual) results from this model in addition to a cost analysis, the designer can determine the best coupling strategy for a PV-EC. Cost analysis, however, is not considered in the scope of this dissertation. The following sections discuss the results calculated from applying the model to the two example PV-EC systems described above.

3.4 Annual Generation Model for Lab-Scale PV-EC

The model is first applied to a reported 25 cm² flow-cell PV-EC for CO₂-CO solar electrolysis device. [60] The source PV circuit was designed for MPP operation at STC giving an SFE of 7.6%. Empirically determined resistive losses due to non-optimized bench-top connections, reduced measured SFE to 6.5%. H₂O electrolysis is a competing reaction at the cathode, due to which FE for CO generation is an important metric, which decreases along with SFE due to increasing parasitic H₂ production. It is important, however, to note that H₂, on its own or together with CO, in CO₂ electrolysis is often a desired product for practical purposes, so the SFE given by equation (3-1) is a rather conservative estimate that does not credit the energetic value contained in H₂ as a product. While CO and H₂ are the products at the cathode, oxygen effuses at the anode, as given below:



where V vs RHE is potential measured against the reversible hydrogen electrode. The I-V curves of the PV and electrochemical components of this device are input to the developed model.

For this device, the output from direct and power-optimizer configurations were computed by applying the annual generation model (discussed in detail in Sections C.4, of Appendix C), the latter referred to as ‘power optimizer coupling’ as defined above. Inverter coupling in this model was implemented using efficiency information of real solar inverters (discussed in Section C.5.1 of Appendix C) that have a variable power

conversion efficiency curve depending on the input power they receive from the PV array. In this work inverter coupling was considered only for large-scale systems and is omitted as a coupling strategy for this scenario. Figure 3-3(a) shows the FE vs. voltage curve of the electrolyzer used, and Figure 3-3 (b) shows the resulting SFE calculated by the model as a function of solar insolation for direct- and power-optimizer coupled PV-ECs. This plot generated by the model contains data for every solar hour of each day in the model year, totaling over 4000 data points. While it is evident from equation (1) that SFE is directly proportional to FE, Figure 3-3 (b) shows how sensitive SFE is to the FE curve given in Figure 3-3(a). Even though the FE in Figure 3-3 (b) and SFE in Figure 3-3 (a) are plotted against different abscissas (voltage and solar irradiance respectively), they can be compared qualitatively due to the approximately-linear dependence of operating voltage on solar irradiance, as given in Figure 3-3 (c).

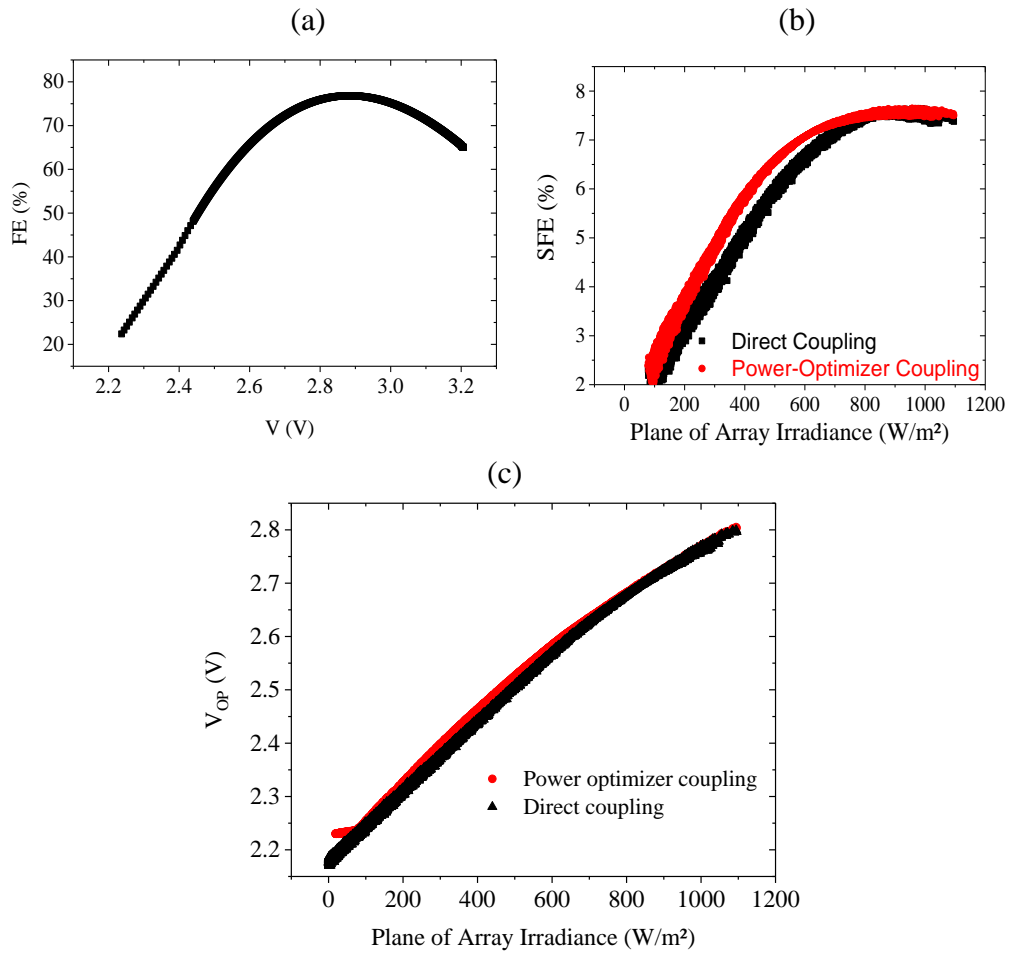


Figure 3-3: (a) FE curve of CO₂ electrolyzer used for the model. (b) Calculated SFE plotted against solar irradiation for directly-connected and power-optimizer-coupled PV-ECs (c) A plot of operating voltage against solar irradiance, showing a near-linear dependence between the parameters, allowing for a qualitative comparison of the FE (V) and SFE (Irradiance) plots (a) and (b).

To compare the coupling configurations quantitatively for the CO₂ PV-EC, the numerical results from the simulation, integrated over the entire model year are given in Table 3-1. The coupling configuration with power optimizer device, has a 5% higher CO gas output with 9% increase in SFE (averaged from its performance for the entire

year) than that of the direct connection. We note that similar increases in the competing production of H₂ are also predicted with power optimizer coupling. While this PV-EC was designed and reported with SFE of 7.6% at STC (without considering voltage drops consistent with this analysis), the actual SFE averaged for the entire year is 5.1% as shown in Table 3-1, a decrease of 32%_{relative} from the maximum efficiency reported at STC. The effect of coupling efficiency on yearly gas output with power optimizer coupling is given in Figure 3-4. A key conclusion is that if the coupling efficiency—the power conversion efficiency of the DC power optimizer—falls below 96%, it does not offer any advantage to the PV-EC over direct connection.

Table 3-1: Final numerical results from annual model calculations for lab-scale CO₂ PV-EC device with demonstrated 7.6% SFE at STC. H₂ production calculated as competing reaction during CO₂ electrolysis

Coupling Type	Avg. SFE (%)	Total CO Produced (g/yr.)	Total H ₂ Produced (g/yr.)
Direct Coupling	5.06	510	24
DC Power-Optimizer Coupling	5.52	536	25

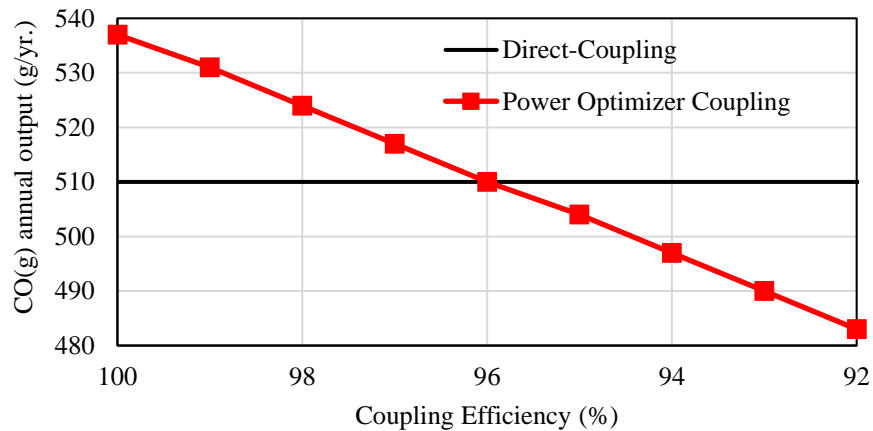


Figure 3-4: Annual gas output from the DC power optimizer configuration as a function of its power conversion (coupling) efficiency.

3.5 Summary

This chapter discussed development of annual generation model for a practical consideration of PV-EC performance. This model used the I-V curves of the solar array and the electrolyzer load as the input, along with the hourly solar insolation and temperature for the selected location, from which it calculates annual average SFE and annual gas output. This model was designed to also incorporate electronic coupling devices in the calculation of its output. This chapter discussed the details of model development and results from its application to the CO₂ PV-EC described in Chapter 2. The results from the model were used to understand the benefit of electronic coupling devices and it was shown that power conditioning devices, the output of this CO₂ PV-EC could be >5% higher annual gas output and >9%_{relative} higher annual average SFE. Chapter 4 discusses the application of this model to a 2 MW H₂O electrolyzer.

Chapter 4

APPLICATION OF YEARLY MODEL TO A CONJECTURAL H₂O PV-EC

This chapter discusses application of the annual generation model to a conceptual PV-EC system comprising commercial c-Si solar cells from SunPower® as the PV source [79] and a 2.1 MW industry-standard proton exchange membrane (PEM) H₂O electrolyzer from ProtonOnsite® as the electrolyzer load [80]. This hypothetical stand-alone solar fuel generation system serves as an example to study a scaled PV-EC system in comparison with lab-scale devices.

The I-V behavior of a single-cell PEM electrolyzer, given in Figure 4-1(a), is scaled up to the power rating of the electrolyzer chosen, 2.1 MW_{DC} (Figure 4-2). The I-V curve of a single solar module is given in Figure 4-1(b). The electrical specifications of the source and the load used for the model are given in Table 4-1. We considered a series connection of the electrolyzer stacks for the 2 MW water electrolysis system in this analysis, however, the exact configuration in the actual system can vary.

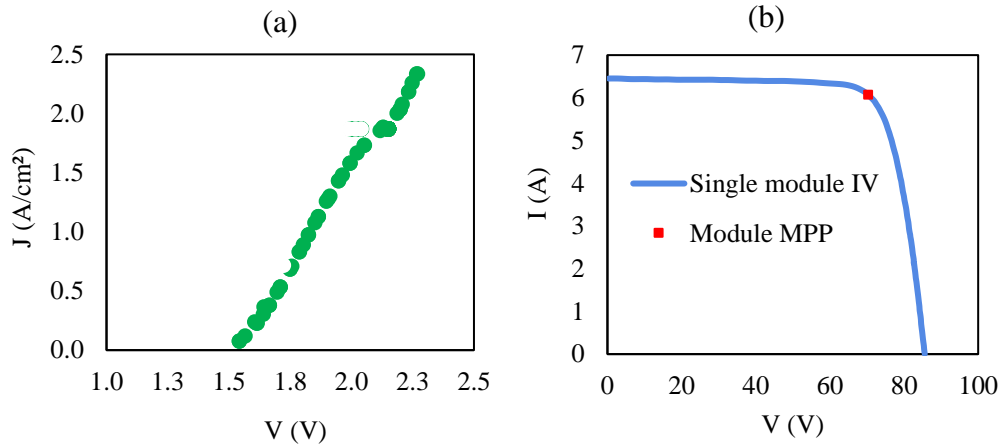


Figure 4-1: (a) Single-cell I-V curve of a PEM water electrolysis cell, (b) I-V curve of a single SunPower® SPE20-435 module used to power the PEM electrolyzer, with MPP indicated.

Table 4-1: Electrolyzer and solar module electrical specifications required for PV-EC design

H ₂ O Electrolyzer Specs [79]		Solar Module Specs [80]	
Maximum operating voltage $V_{EC, Max}$ (V)	1693	P (W)	435
Maximum operating current $I_{EC, Max}$ (A)	1248	V_{MP} (V)	70.6
Power Rating (MW)	2.11	I_{MP} (A)	6.1
H ₂ produced per day (Kg H ₂ /day)	902	Average Power Efficiency (%)	20.3%
Power Consumed per Mass of H ₂ Gas Produced (kWh/kg)	59	Module Power Temperature Coefficient (%/°C)	-0.38
		Module area (m ²)	2.14

To design a PV array that is optimally matched to the electrolyzer of interest in the directly-coupled configuration, the 1-Sun maximum power voltage and current output of the solar array are matched to the rated peak power of the electrolyzer using their I-V curves. This is done as follows,

$$\text{required number of modules in series per string} = \frac{V_{EC,Max}}{V_{MP,1-sun}} = \frac{1693 V_{DC}}{70.6 V_{DC}} \approx 24 \quad (4-1)$$

$$\text{number of strings in parallel} = \frac{I_{EC,Max}}{I_{MP,1-sun}} = \frac{1248 A_{DC}}{6.09 A_{DC}} \approx 205 \quad (4-2)$$

where $V_{EC,Max}$ and $I_{EC,Max}$ are the maximum operating voltage and current of the electrolyzer load (comprised of a single 2.1 MW electrolyzer), respectively, and $V_{MP,1-sun}$ and $I_{MP,1-sun}$ are the maximum power voltage and current of the SunPower® solar module, respectively. [80] The above calculation shows that the PV array would require exactly 24 modules in series per string and 205 strings in parallel, a total of 4,920 modules, to provide sufficient voltage and current, respectively, to the load in direct-coupling configuration. This assumes no system losses and operation at STC conditions. Such an arrangement of solar panels, where the number of strings connected in parallel is much larger than the number of modules per string, is converse to traditional PV array configurations where typically lower currents are driven at high voltages by minimizing the parallel-connected strings to minimize I^2R losses. Routing such high currents (>1200 A) from 205 parallel-connected strings would require impractically heavy gauge wiring to keep I^2R losses suitably low. An indirectly-coupled configuration offers the freedom to design the PV array independent of the DC I-V requirements of the electrolyzer load unlike in direct coupling. This also has the advantage of eliminating the need for bulky wiring across the length of the array, making it a more practical and cost-effective option. While the details are not essential for this modeling, we note that the electrolyzer power requirement would be satisfied in the indirectly connected configuration by arranging the 4,920 modules in a more conventional low-current-high-voltage PV array configuration.

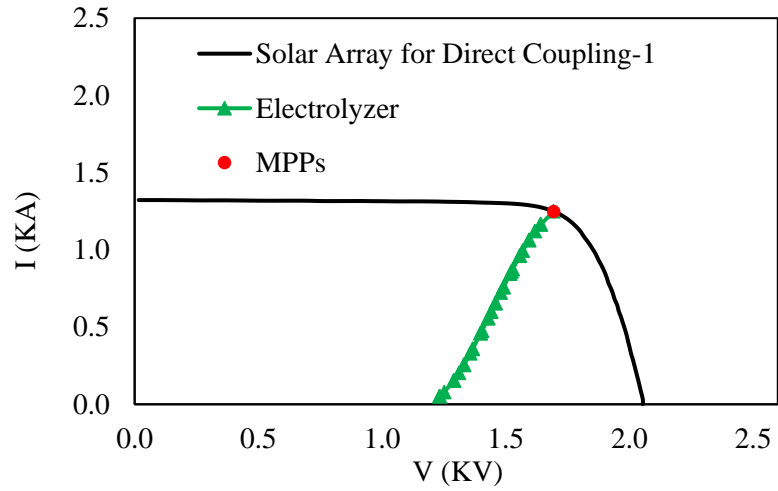


Figure 4-2: I-V curves of 2.1 MW PEM electrolyzer overlaid with the STC I-V curves of the solar array designed the optimally matched ‘Direct Coupling-1’ configuration with MPP indicated.

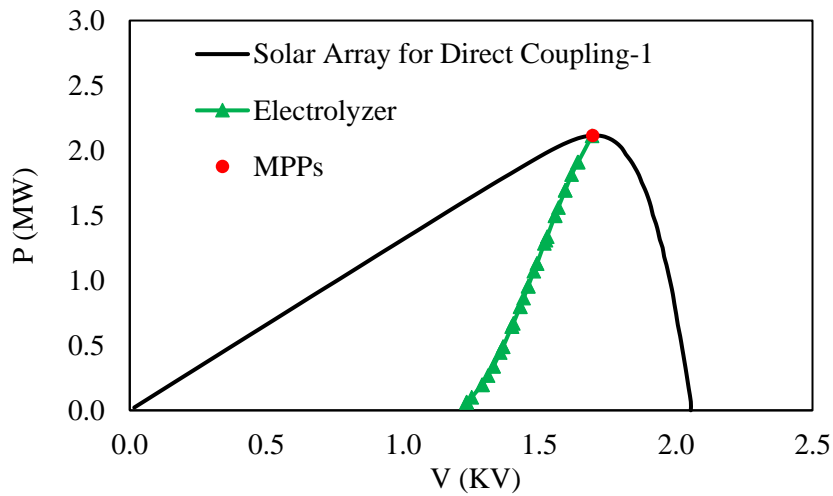


Figure 4-3: Power vs. Voltage— $P(V)$ —curves of 2.1 MW PEM electrolyzer overlaid with the STC I-V curves of the solar array designed for ‘Direct Coupling-1’, optimally matched with MPP indicated.

The results from the model for ‘Direct Coupling-1’ are illustrated as hourly profiles for SFE for a typically sunny and a cloudy day in Figure 4-4. The effect of

changing insolation on SFE can be seen in Figures 4-4 (a) and 4-5(a), and on hourly module temperature in Figures 4-4 (b) and 4-5 (b), for sunny and cloudy days, respectively. It can be seen from these plots that the hourly SFE curve decreases from ~8 am until noon then increases until 5 pm on the sunny day due to larger temperature dependent module losses ($0.38\%/^{\circ}\text{C}$ from Table 4-1) while the SFE remains moderately constant throughout the cloudy day due to the lower peak module temperature. Comparing these curves against insolation and temperature shows that the ~ 30% decrease around noon on the sunny day due to increased module temperature, while decreases during dawn and dusk times are due to low insolation. However, the most critical observation for this work is that the power-optimizer coupling has higher SFE at all times for both types of days.

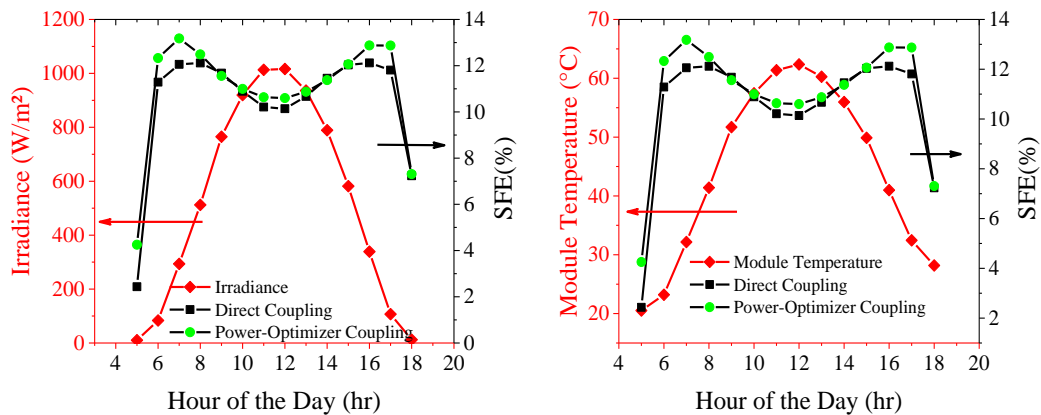


Figure 4-4: Hourly efficiency profile shown for a typical sunny day in August of the model year, (a) in comparison to hourly irradiation and (b) module temperature

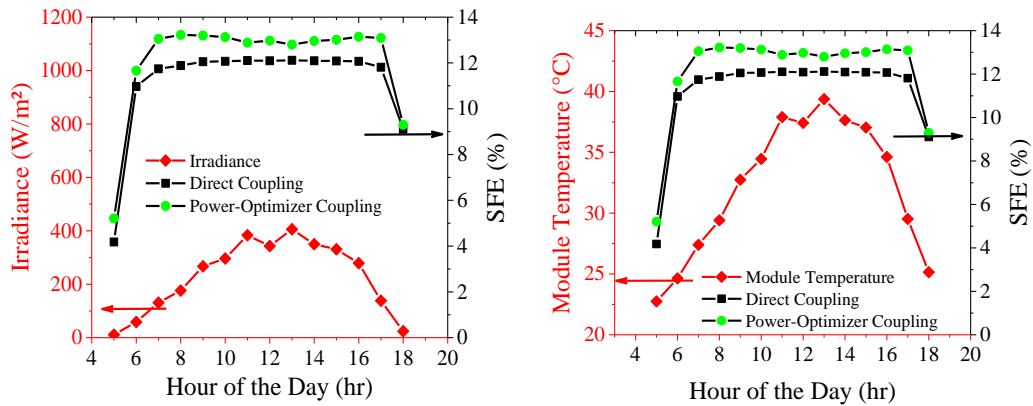


Figure 4-5: Hourly efficiency profile shown for a typical cloudy day in August of the model year, (a) in comparison to hourly irradiation and (b) module temperature

The system efficiency and H₂ gas output integrated over the entire year for the *optimally matched* direct coupling ('Direct coupling-1') and two power optimizer coupling approaches are summarized in Table 4-2. The PV-EC with power optimizer coupling of 100% coupling efficiency produces 5% higher gas output with a 9%_{relative} higher annual average SFE than the optimally matched 'Direct Coupling-1'. In that case, the choice between these two coupling strategies should be made by supplementing the generation model results with cost analysis. The gas yield and SFE for the DC-AC-DC coupling strategy as described in the introduction are also given in Table 4-2. They are the same as those of direct coupling despite the PV inverter providing MPPT. It is evident from these results that the assumed 5% from converting DC to AC at the PV array and back from AC to DC in the electrolyzer in the DC-AC-DC configuration compensate any gain provided by the MPPT included in the PV inverter. Figure 4-6 shows the effect of coupling efficiency on annual gas production, compared to the other

configurations. Similar to the earlier lab-scale device, this configuration loses its advantage at MPPT conversion efficiencies below ~94% efficiency.

Table 4-2: Tabulated annual results from hydrogen generation model applied to 2.1 MW H₂O PV-EC for different coupling strategies: optimally matched direct coupling-1, power optimizer coupling with 100% coupling efficiency, DC-AC-DC coupling with 95% DC-AC conversion efficiency

Configuration	STC Coupling Efficiency (%)	Avg. SFE (%)	Total H ₂ Yield (Ton H ₂ /yr.)
Direct coupling-1	100	10.32	70.78
Power optimizer coupling	NA	11.28	74.62
DC-AC-DC coupling	NA	10.33	70.35

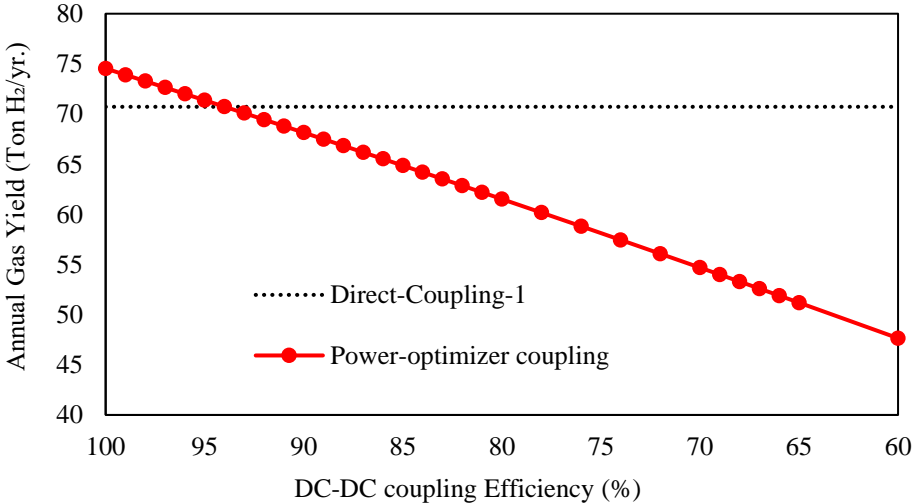


Figure 4-6: Annual gas yield of power optimizer coupled PV-EC as a function of the coupling electronics power conversion efficiency. Annual gas output from Direct Coupling1 are shown without power coupling. The red line with symbols is for a system using power optimizer with variable power conversion efficiency.

4.1 Advantage of Indirect Coupling in *Sub-Optimally Matched* PV-EC's

The benefit from indirect coupling using power optimizer is small for PV-ECs when they are optimally matched for direct connection. The real benefit of using indirect coupling with power conditioning devices can be illustrated using the same example of the MW-scale PV-EC but now we create an *intentional mismatch* between a PV array of the same power capacity as above and the electrolyzer. Consider an alternative PV array configuration for direct connection of this PV-EC—slightly mismatched from the optimal setup to have 30 strings with 164 modules per string instead—termed ‘Direct Connection-2’. Table 4-3 compares the 2 PV arrays, showing that this suboptimal array design is offset from the previous configuration by 25% on the voltage axis. Its effective I-V curve and power curve are given in Figures 4-7 and 4-8 respectively and the modeled results in Table 4-4. It is evident from Figures 4-7 and 4-8 that the electrolyzer curve now falls at a lower voltage from the MPP of the solar array. The annual output calculated from this configuration is 20% lower than the optimally configured PV-EC. In that case, employing power optimizer coupling would offer a much higher benefit—a 24% higher gas yield than the mismatched direct coupling, for a device with >94% coupling efficiency (Figure 4-9). From Figure 4-9, it is apparent that the coupling efficiency would have to be as low as 75% to match the output from this configuration, much smaller compared to the efficiency of power electronic devices.[78]

Table 4-3: Solar array layout and electrical specifications for the two directly coupled PV-EC configurations

Configuration	# of solar panels	P_{MAX} (MW)	V_{MP} (V)	I_{MP} (A)	Comment
Direct-Coupling-1	24s x 205p = 4,920	2.1	1,750	1,224	V_{MP} well matched to EC at STC
Direct-Coupling-2	30s x 164p = 4,920	2.1	2,187	979	V_{MP} mismatched by 25% to EC at STC

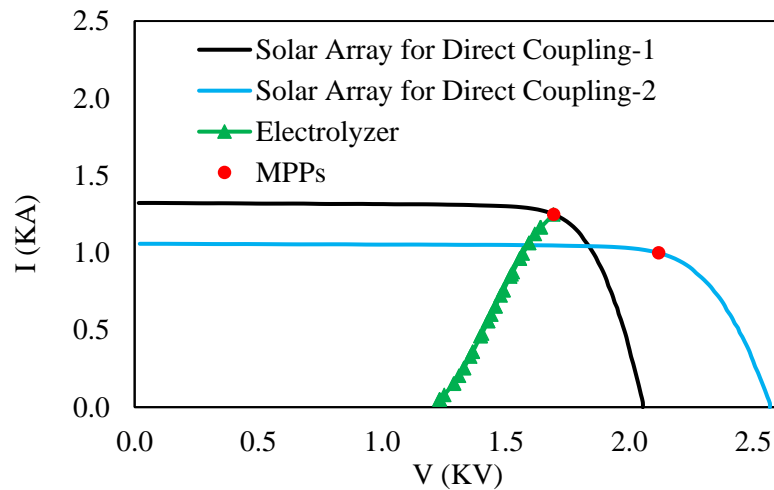


Figure 4-7: I-V curves of 2.1 MW PEM electrolyzer overlaid with the STC I-V curves of the two solar arrays designed for direct coupling—one optimally matched (‘Direct Coupling-1’) and one slightly offset from it (‘Direct Coupling-2’), with MPPs indicated. The PV array in Direct Coupling-2 is designed to have a 25% voltage mismatch relative to Direct Coupling-1, discussed in Section 4.1.

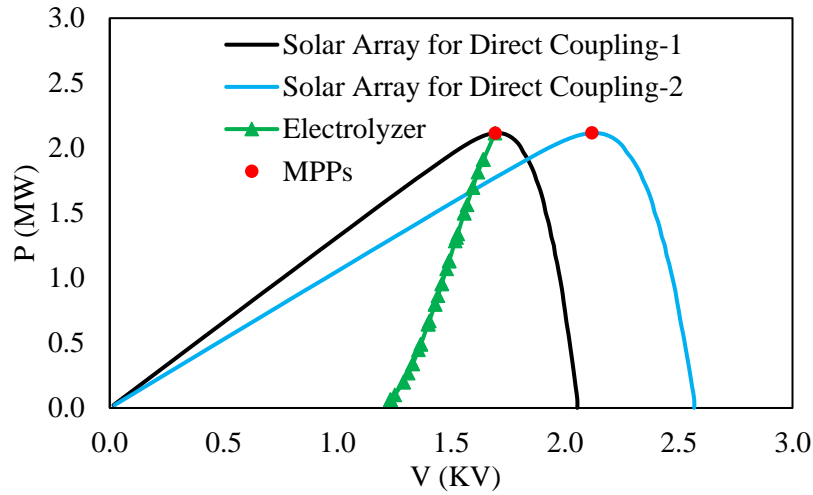


Figure 4-8: Power vs. Voltage—P(V)—curves of 2.1 MW PEM electrolyzer overlaid with the STC I-V curves of the two solar arrays designed for direct coupling—one optimally matched (‘Direct Coupling-1’) and one slightly offset from it (‘Direct Coupling-2’), with MPPs indicated. The PV array in Direct Coupling-2 is designed to have a 25% voltage mismatch from that of Direct Coupling-1, discussed in Section 4.1.

Table 4-4: Tabulated annual results from hydrogen generation model applied to 2.1 MW H₂O PV-EC for ‘Direct Coupling-2’, compared with those of ‘Direct Coupling-1’, power optimizer coupling with 100% power conversion efficiency, and DC-AC-DC coupling with 95% DC-AC conversion efficiency, reproduced here from Table 4-2 for comparison.

Configuration	STC Coupling Efficiency (%)	Avg. SFE (%)	Annual H ₂ Yield (Ton H ₂ /yr.)
Direct Coupling-2	75	9.16	57.39
Direct Coupling-1	100	10.32	70.78
Power optimizer coupling	NA	11.28	74.62
DC-AC-DC coupling	NA	10.33	70.35

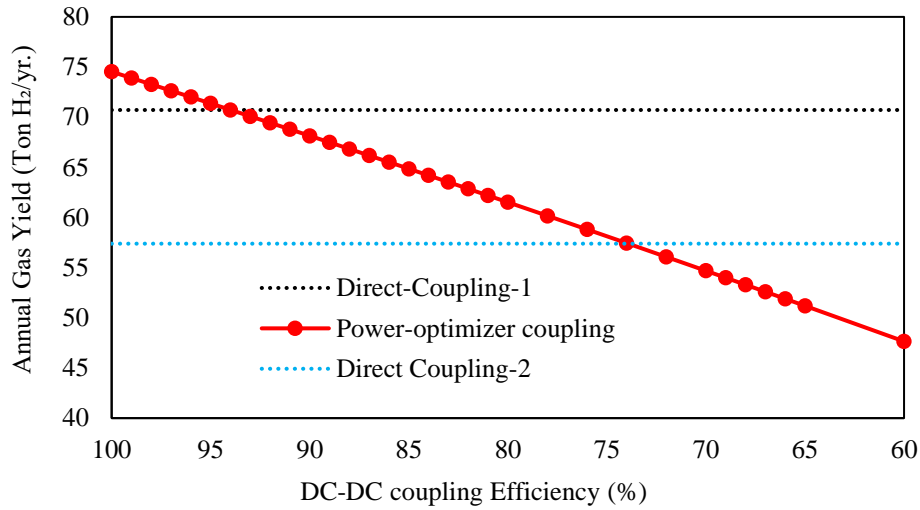


Figure 4-9: Annual gas yield of power optimizer coupled PV-EC as a function of the coupling electronics power conversion efficiency. Results from both well matched (Direct Coupling1) and mismatched (Direct Coupling 2) are shown without power coupling. The red line with symbols is for either system using power optimizer.

4.2 Incorporating Series Resistance Losses

One of the cited disadvantages of PV-ECs over integrated PEC devices is their power loss associated with wiring. [2] The design standard for PV arrays is to keep these losses to <2% of STC voltage output. [81] To quantitatively evaluate potential losses in PV-EC architecture, we configure the developed generation model to incorporate voltage drops from wiring, making the model more realistic in its application. A tabulated account of step-by-step calculation for wiring in relation to the resulting series resistance of 0.2% for the directly-connected PV-EC is given in in Table 4-5. Incorporating wiring losses in the model does not require this elaborate calculation, but rather, the resistance value corresponding to the 2% wiring-related voltage drops is determined as given in equation (4-3) and used as an additional series resistance in the I-V translation equations:

$$R_w = \frac{0.02 \times V_{MP_{STC}}}{I_{MP_{STC}}} \quad (4-3)$$

This table is shown here to give an idea of how a PV array layout is designed in relation to wiring, and to provide an estimate of the ampacity that direct connection demands. It can be seen from this table that following the National Electric Code design standard for solar PV arrays, the directly-connected configuration would require a bundle of 20 AWG 4/0 copper wires to keep the wiring losses (R_w) to 0.2% of V_{MP} at STC. On the other hand, a single AWG 4/0 wire suffices for the indirectly-coupled configurations (not shown here), since its current is 145 A, 8.6x smaller compared to that of the directly-coupled PV array configuration, 1248 A. This exercise demonstrates that indirectly-connected PV-EC's have an additional advantage: reducing 'copper costs' in the system, by means of allowing low operating currents routed at high voltages.

Table 4-5: Tabulated calculation showing wiring design and wiring loss estimation for directly-connected PV-EC

Parameter	Value	Units
I _{SC} from single module	6.43	A
Max. Temp. in Newark, DE	40	°C
I _{SC} Temp. coefficient	2.6	mA/°C
Module NOCT	45	°C
Max. possible solar insolation in Newark, DE (from NSRDB)	1096	W/m ²
Max. possible module temperature, T _{Max}	74.25	°C
Max. possible source circuit current I _{SC, Max}	7.18	A
# of strings in parallel for direct connection	205	-
Total current (max.) out of combiner box	1471	A
156% of max. I _{SC}	2295	A
Ampacity of biggest conductor (after 250 kcmil), 4/0 AWG, with 90°C insulation at 30°C T _{air}	260	A
Ampacity derating for a maximum possible air T of 40°C	0.91	-
Effective ampacity at 40°C is	236.6	A
# of AWG 4/0 conductors now required for max. ever possible currents	9.7	-
Ampacity Derating factor for 10-20 conductors in conduit	0.5	-
Total number of conductors now required	19.4	-
DC resistivity of AWG 4/0 cable	0.061	Ω/kft
Effective resistance of 20 cables in conduit (in parallel), 1000' long, R _w :	304	mΩ
% Voltage drop including R _s , R _w	4.93	-
% Voltage drop using this cable set, AFTER R _s drops	0.22	%
Cost of Wire/1000 ft	5,402	\$

The annual yield for the H₂O PV-EC discussed here was calculated with 2% wiring losses incorporated, and the results are given in Table 4-6, in comparison with no wiring losses. It shows that incorporating a maximum 2% wiring losses have reduced the annual SFE of the direct connection by ~2.5%_{relative} and its annual H₂ yield by 5.5%. This drop in performance is much smaller for the indirectly coupled configurations

(‘Power optimizer coupling’ and DC-AC-DC coupling)—with a $<0.4\%$ _{relative} drop in annual SFE and $<1\%$ drop in annual gas yield. This discrepancy in the decrease of performance with wiring losses incorporated for the direct and indirect connections is explained due to the large difference in operating currents of these two configurations and provides indirect coupling with another advantage.

Table 4-6: Tabulated results from the annual generation model for 2 MW H₂O electrolysis system

Coupling	Without Wiring Losses		2% Wiring Losses Included	
	Avg. SFE (%)	Total H ₂ Yield (Ton H ₂ /yr.)	Avg. SFE (%)	Total H ₂ Yield (Ton H ₂ /yr.)
Direct coupling	10.32	70.78	10.06	66.90
Power optimizer coupling	11.28	74.62	11.24	73.91
DC-AC-DC coupling	10.33	70.35	10.29	69.68

4.3 Summary

In chapters 3 and 4, it was demonstrated that the conventional figure of merit, SFE obtained at STC, is an incomplete metric for realistic solar fuel generation considering the PV device operating conditions are seldom close to STC. Two system-level aspects of PV-EC’s were quantitatively analyzed to determine SFE for non-STC conditions: 1) calculating annual fuel output for an outdoor PV-EC using hourly solar

irradiance and ambient temperature data for a mid-latitude location with moderate climate (Wilmington DE, USA); and 2) determining the benefits of using power optimizing electronic coupling between the PV array and the electrolyzer to address the realistic situation of a non-optimally matched system. An annual generation model for decoupled solar fuel generation systems was developed and used to compare realistic field performance characteristics. The discrepancy between SFE reported under STC and its yearly average value can be as high as 32%. This disparity arises from the fact that PV-EC is effectively a source-load combination where the load (electrochemical cell) has a constant electrical behavior unlike the source (PV component) that varies with irradiance and temperature. We also quantify the benefits that MPPT with voltage-regulated output can offer using the annual generation model on a previously-reported lab-scale CO₂ electrolysis device, and a MW-scale H₂O electrolysis system, conceptually designed for this study. We show that coupling devices improve the annual gas yield by up to 5% even for a PV array that is well matched to the electrolyzer at STC. But the more important result from this study is that the benefit can be many times higher if the directly connected PV-EC is not optimally power matched. This highlights the importance of optimal power matching of PV-ECs to maximize their gas yield. The power conversion efficiency of coupling devices was also explored using this model and it was shown that with optimal STC coupling, efficiencies as low as 95% are tolerable.

This quantitative benefit of electronic coupling over direct PV-EC connection is however, component-specific (based on selection of PV and catalyst technology, conversion efficiency of electronic coupling devices, their I-V behavior, geographic location, and scale, among other specifications). To calculate a quantitative benefit of

electronic coupling for any given system in general, a similar calculation of system output as given in this study is required for a fair and accurate comparison among the several possible coupling strategies, including a detailed cost analysis if so warranted.

Chapter 5

ANTIMONY-DOPED CADMIUM TELLURIDE SOLAR CELLS

Following an examination of extrinsic doping as a means to realize the open circuit voltage potential of CdTe photovoltaics presented in Chapter-1, this chapter justifies Sb as the dopant of choice among other group V elements previously investigated. [58] It also provides a detailed description of device processing, performed by researchers Brian McCandless and Wayne Buchanan at the Institute of Energy Conversion (IEC) and our collaborators at the National Renewable Energy Laboratory (NREL), to provide the necessary background for the primary focus of this work—device characterization and analysis. Section 5.5 of this chapter introduces the different measurement techniques employed in this work to analyze these devices. A brief overview of the device characterization methods and the corresponding analysis techniques employed on the measured data is also given here prior to discussing their application to the devices of focus in this work.

5.1 Sb as the Dopant of Choice

State-of-the-art CdTe cells have relied on bulk intrinsic p-type doping by cadmium vacancies (V_{Cd}), leveraging high temperature deposition for thermodynamically favorable production of V_{Cd} . This new work focuses on leveraging atomic substitution of Te with group V elements for p-type doping by providing Cd excess to allow favorable thermodynamic conditions for Te replacement. The IEC team modified the vapor transport deposition (VTD) process to simultaneously deliver excess Cd vapor and group V vapor species to promote lattice substitution without forming n-type CdTe. Some important material parameters used in evaluating the efficacy of group V elements as dopants are: (i) atomic radius match of the dopant element with that of

Te, which it is replacing, to minimize lattice strain, (ii) low enthalpy of defect formation, and (iii) low transition energy of the resulting defect (dopant substitution of Te). Figure 5-1 presents predicted energy levels of dopant transition energies and plots the other parameters of the selected group V elements. While the covalent radius is a known elemental parameter, the defect transition energy levels and defect formation enthalpies are taken from theoretical estimates of Wei *et al.* [56] Note that the transition energy levels provided by Wei *et al.* are only a theoretical estimate and have not been fully validated experimentally.

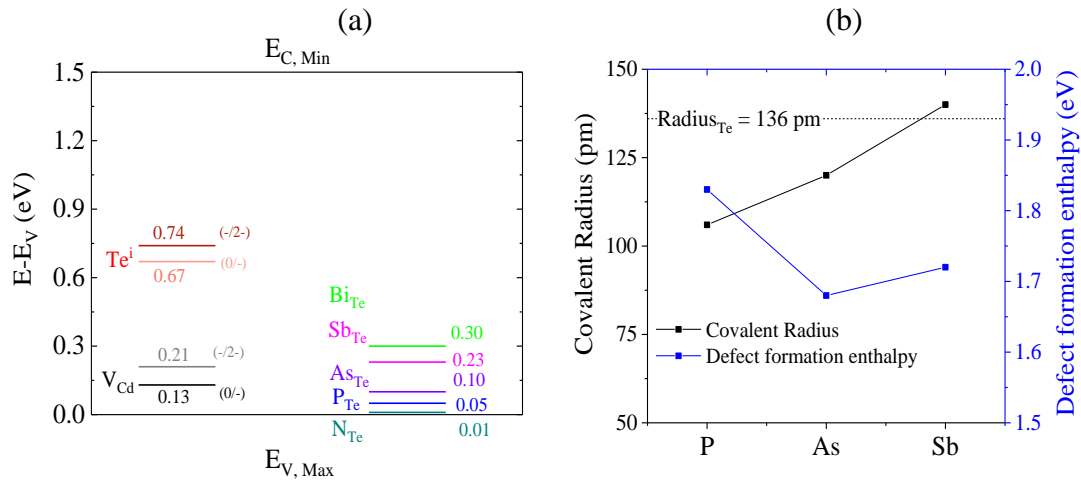


Figure 5-1: (a) Calculated transition energy levels of group V elements in CdTe lattice by Wei *et al.* [56] in CdTe band gap (b) atomic radii and defect formation enthalpies in relation to their suitability as p-type dopants in CdTe

The set of parameters shown in Figure 5-1 is not sufficient to judge the efficacy of these elements as dopants in CdTe films but is rather used as a reference to guide experimental process design. A detailed account of evaluating P, As and Sb as dopants in the CdTe thin films was reported by McCandless *et al.* [58], which provides an

assessment of these dopants based on performance of devices made with doped CdTe. It reports a detailed evaluation of a variety of metrics spanning those dictating processing design to those qualifying doped layer and device behaviors, including: (i) vapor pressure of the dopant precursor in the deposition reactor (the lower, the better), (ii) doped CdTe film quality (dense films, absence of voids, large grains), (iii) sufficient minority carrier lifetime (τ) estimated from time-resolved photoluminescence (TRPL), (iv) incorporation of dopant elements in the film measured by secondary ion mass spectrometry (SIMS), (v) activation of the incorporated dopant estimated from capacitance-voltage measurements (discussed in detail in section 5.2). Following a careful review of these parameters as metrics (discussed in detail in reference 58), Sb was chosen as the focus of this work primarily due to its low formation enthalpy and its close atomic radius match with Te. The following section discusses the fabrication sequence of diagnostic Sb-doped CdTe (CdTe:Sb) devices, performed by researchers at the IEC in collaboration with NREL. The primary focus of this work is the device characterization and analysis, discussed in detail in Chapter 6, and Section 5.5 of this chapter provides an introduction to these measurement and analysis techniques.

5.2 Fabrication Sequence of Diagnostic CdTe:Sb Devices

The front-wall superstrate device structure of diagnostic CdTe:Sb solar cells discussed in this work is given in Figure 5-2. This schematic shows the different layers of the device stack, labeled along with their deposition methods, discussed sequentially in this section.

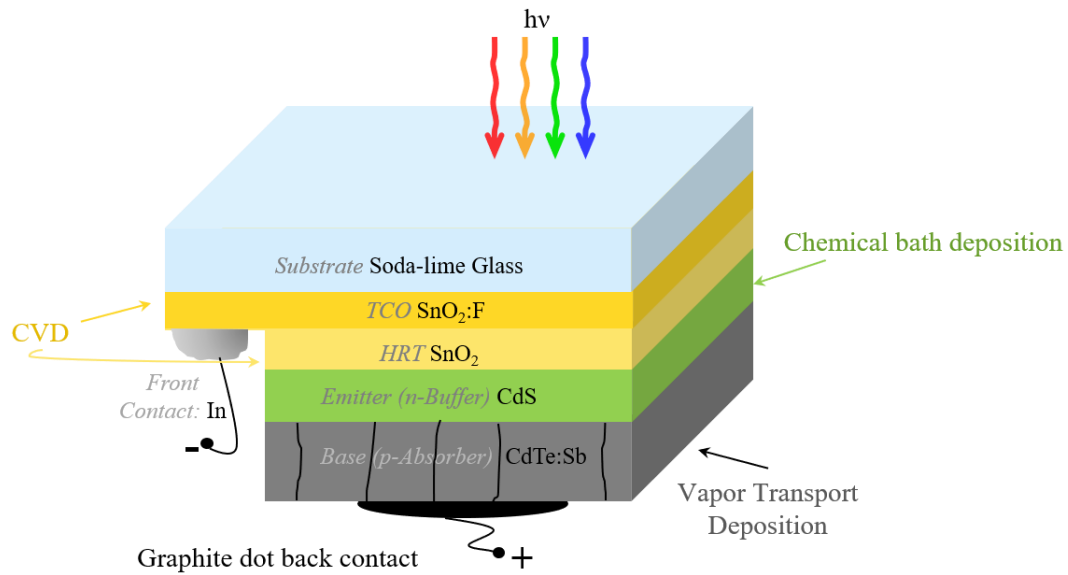


Figure 5-2: Device structure of diagnostic CdTe:Sb solar cells

5.2.1 Window (front contact) layer stack deposition

Thin ‘AF45’ glass from Corning is used as the substrate, chosen for its superior light transmission and heat tolerance properties. The ‘window’ layers consist of a bilayer stack of n-type fluorinated tin oxide ($\text{SnO}_2\text{:F}$) as the transparent conductive oxide (TCO) and undoped, intrinsic, tin oxide (SnO_2) for the high resistance transparent (HRT) layer which are both deposited by chemical vapor deposition (CVD) by our collaborators at NREL. While TCO promotes lateral transport of carriers, HRT layer prevents junction formation between the emitter (CdS) and the TCO ($\text{SnO}_2\text{:F}$) layers.

5.2.2 Chemical bath deposition of CdS

Following CVD of the TCO+HRT window layer stack on the glass substrate, the n-type CdS emitter layer is deposited using chemical surface coating deposition process at IEC. [82], [83] This process is designed to deposit a uniform ~20 nm thick

CdS layer, which is then subject to a CdCl₂ vapor heat treatment (at 415°C for ~10 minutes in air). This treatment is performed to facilitate evaporation of solvent residue from the coating process, along with recrystallization and growth of grains, while mitigating CdS/CdTe interdiffusion during downstream processing. [84] [85]

5.2.3 CdTe:Sb Growth by Vapor Transport Deposition (VTD)

The most critical layer for device performance is the p-type CdTe absorber. A simple schematic of VTD reactor at the IEC used to deposit CdTe [86] is given in Figure 5-3. A moving 10 cm x 10 cm glass substrate, already coated with window layers and CdS emitter, is deposited with CdTe at a rate of ~1 μm/min. Originally designed for intrinsic CdTe deposition, this reactor was modified for group V element incorporation. [58] In the case of Sb-doping, high purity-CdSb crystals were used as a precursor along with CdTe crystals in the perforated quartz ampoule at the inlet zone shown in Figure 5-3. This quartz ampoule is enclosed in a BN source container with an aperture slit facing the surface below, also shown in Figure 5-3. The high temperature growth environment is originally designed to favor Cd vacancies (V_{Cd}) in the deposited film, but the presence of Sb along with Cd and Te₂ vapor mixture allows Sb incorporation in the film. The vapors in the gas mixture are delivered to the glass surface using N₂ carrier gas supplied externally. More details of this process are found in ref [58]. Following the deposition of CdTe in VTD, ~ 1 cm² coupons are cleaved from the 10 cm x 10 cm glass substrate for processing final devices.

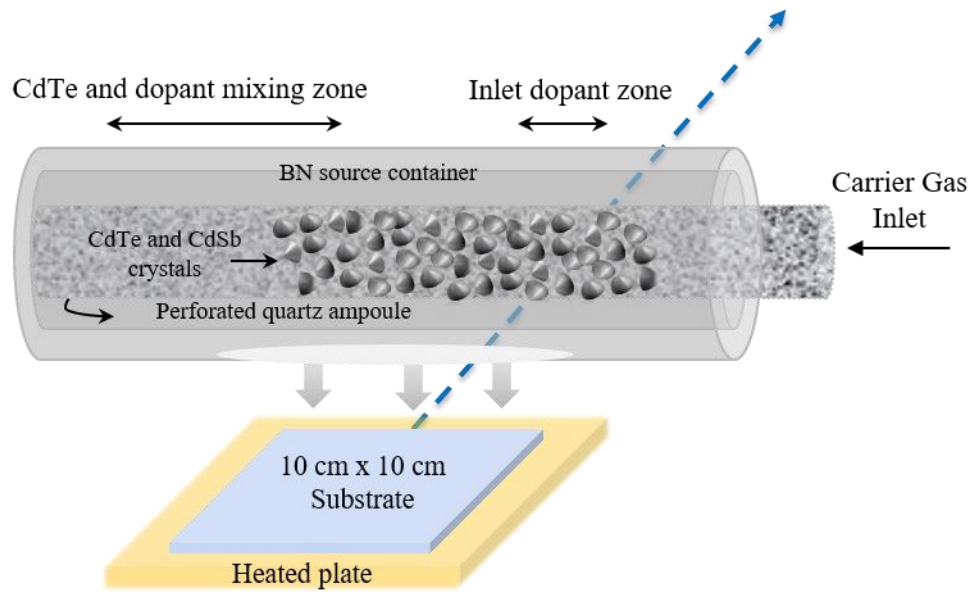


Figure 5-3: Schematic of the VTD reactor at the Institute of Energy Conversion, employed to deposit Sb-doped CdTe layer

5.2.3.1 Dopant incorporation in VTD-deposited films

A SIMS depth profile of a CdTe:Sb film at IEC (measurement provided by Evans analytic group) [58] is given in Figure 5-4 to show Sb incorporation in the VTD-deposited film. A nearly-uniform incorporation, with $>1 \times 10^{17} \text{ cm}^{-3}$ Sb at the CdTe/CdS interface has been demonstrated in films deposited at the IEC (Figure 5-4). Sb concentration is controlled using the ‘inlet method’, where the dopant species are entrained *in-situ* along with the Cd and Te vapor generated from the CdTe source using high purity CdSb as the source material as shown in Figure 5-3. An alternative approach, termed ‘uniform source delivery method’ was also proposed (although the devices in this work are made from the former method), where CdTe source crystals were uniformly coated with CdSb by mechanically blending CdTe powder with CdSb in

sealed quartz ampoules, fired at 840°C and then rapidly cooled, enabling CdTe source material incorporated with Sb up to several weight percent. [58]

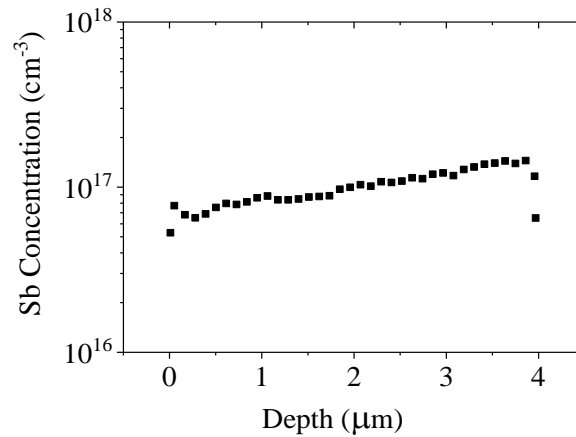


Figure 5-4: Sb incorporation shown in CdTe:Sb film deposited using VTD at the IEC, measured using SIMS at Evans analytic group, taken from ref. [58]

5.3 Annealing Treatments

It is well known that annealing; i.e at 400-500°C for ~20 minutes in air with exposure to CdCl₂, vital to improving device performance of state-of-the-art CdTe solar cells by (i) doping CdTe to ~10¹⁴ cm⁻³, (ii) passivating grain boundaries and (iii) relaxing interface stress between CdTe and CdS. The treatments that the CdTe device stack is subject to in this work, prior to receiving electrical contacts, can be categorized into: (i) CdTe film treatments, to facilitate Sb ‘activation’ in the CdTe film (Sb occupying Te lattice sites) and (ii) CdTe device anneal, to improve the overall stack quality for enhancing the electrical performance of the resulting device made from the stack. These two treatments are discussed in detail below.

5.3.1 Cd-vapor anneal to facilitate Sb incorporation in CdTe lattice

While the VTD process incorporates Sb in the CdTe film, this does not guarantee Sb ‘activation’ *via* Sb substituting Te in the lattice. Extrinsic doping of CdTe using Sb involves formation of V_{Te} point defects, to be effectively occupied by the Sb atoms incorporated in the lattice during VTD. It is extremely important to ensure that this dopant substitution dominates over its interstitial occupancy. A high temperature (400°C-500°C) anneal of CdTe with a Cd overpressure has been shown to effectively activate incorporated extrinsic dopants. [57], [58] [87], [88], [89]. At the same time, it is necessary to ensure prevention of Cd-interstitial (Cd_i) formation, a trap 33 meV below the conduction band. These treatments are performed in a sealed glass ampoule in a temperature-controlled oven. Figure 5-5 shows a photograph of such an ampoule carrying multiple CdTe-deposited substrate coupons. The oven’s spatially variable temperature profile enables providing multiple substrate coupons in the ampoule exposure to different temperatures.

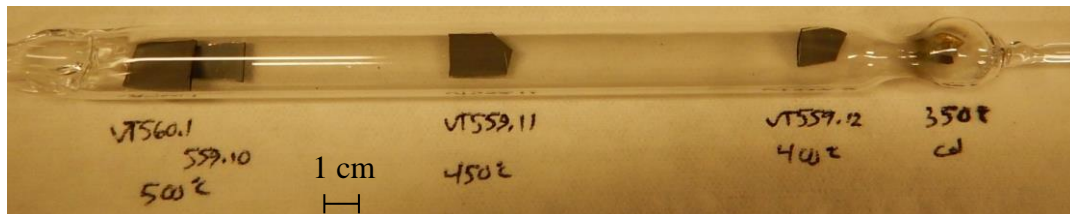


Figure 5-5: Picture of an ampoule receiving Cd-vapor treatment. Shown here are 3 CdTe:Sb film coupons placed at multiple locations strategically to expose each of these samples to different temperature, dependent on their location in the ampoule with respect to the heat source.

5.3.2 Device anneal treatment to improve overall device behavior

CdCl_2 heat treatment for improvement of device behavior is a common post-processing technique for CdTe thin-film photovoltaics. [19] A heat treatment of an activated CdTe film stack on the substrate at 300-500°C with CdCl_2 and air (O_2) in the ambient is known to improve overall device behavior. CdCl_2 has been shown to reduce grain boundary defects by recrystallizing the CdTe layer, increasing the grain size, passivating the CdTe/CdS interface by promoting interdiffusion of sulfur from CdS into CdTe, and increasing carrier transport through grain boundaries. [90] While Cl is most commonly used, other halogens as Br and I have been shown to provide similar effects. [83] O_2 has been known to increase hole concentration by enabling formation of cadmium vacancies (V_{Cd}) for intrinsically p-type doped CdTe devices.

There are two ways to deliver CdCl_2 in the anneal ambient: (i) by coating the exposed CdTe surface with a droplet of a CdCl_2 -methanol solution, or (ii) by placing a CdCl_2 -coated cover plate over the exposed CdTe surface promoting an indirect exposure to CdCl_2 via re-evaporation of the CdCl_2 . A schematic of these two Cl-treatments are given in Figure 5-6. The primary focus of this work is to apply these anneal techniques to Sb-doped devices and evaluate them using device characterization methods described in Section 5.5. The effect of these treatments is discussed in detail with regard to their device performance and analysis in Chapter 6 in detail.

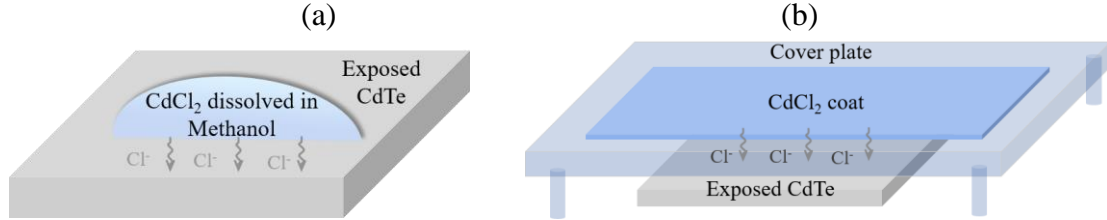


Figure 5-6: Schematic of CdCl₂ anneal by (a) CdCl₂ coat method and (b) CdCl₂ vapor method

5.3.3 Back (p-type) contact deposition

CdTe semiconductor is known to have a high electron affinity of ~ 4.4 eV, [116] making it challenging to find a metal to directly form an ohmic contact. [91] [92] [93]. For this reason, state-of-the-art CdTe device processing usually employs a thin Cu-doped CdTe surface alloy layer as an intermediate tunneling layer for hole transport enabling low resistance and significantly reducing the contact barrier for electron injection. This process, however, is not employed on the devices studied in this work, since the charge arising from Cu doping would interfere with the estimation of charge response from Sb doping using capacitance voltage measurements. Instead, an ~ 10 μm thick graphite dot made on the exposed CdTe surface acts as the p-type contact, made using Acheson 50SS ink. Prior to this step, an ethylenediamine (EDA) etch is performed on the stack to remove surface oxides and create a very thin, <10 -nm, Te surface. The surface area of the resulting device is defined by the area of this dot contact, measured using a calibrated photographic scan. It is important to note that the resulting contact is non-ideal, tending towards a Schottky-type contact, and does not produce a high efficiency device structure for reasons above. It was implemented in these test structures

to avoid clouding the interpretation of the charge measurements and interpretation of Sb doping.

5.3.4 Front (n-Type) Contact Deposition:

The last step in making a device from the substrate stack is to make an electrical contact to the n-type emitter layer facing the front (glass) side. This is done by a careful mechanical abrasion of the exposed CdTe surface. Since the least adhesive interface of the SnO₂:F/i-SnO₂/CdS/CdTe stack is between the TCO and the HRT (SnO₂:F/i-SnO₂), this scraping removes all of CdTe/CdS/ITO stack together, leaving the FTO surface exposed. It is possible to make electrical contact to this exposed surface by pasting a thin indium solder onto it. FTO adheres very well to the glass and is mechanically 'hard' thus resistance to the scraping. A photograph of the resulting CdTe:Sb device is shown in Figure 5-7. The front surface of the device (that receives illumination) is shown in Figure 5-7 (a), and Figure 5-7 (b) shows the device from the back, showing the graphite dot p-type contacts in the center and the indium solder at the corner of the coupon.

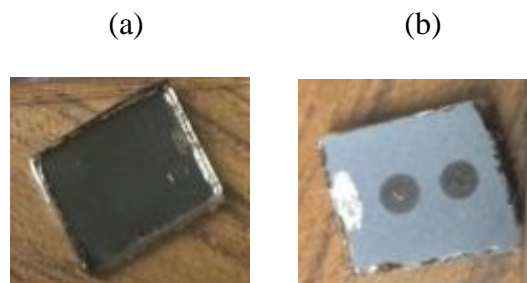


Figure 5-7: A photograph showing finished diagnostic CdTe:Sb devices made on glass substrates (a) from the top and (b) from the bottom. Note that the carbon contacts define the area of the solar cell. The substrate in the picture was $\sim 1 \times 1 \text{ cm}^2$ and the graphite cell contact is approximately 3 mm in diameter

5.3.5 Variability in similar devices

To understand the variability in devices made using the process sequences discussed above, a long coupon (~1" x 0.3") diced from a VTD-grown CdTe:Sb substrate was processed with 4 devices along its length. This enables us to compare devices made on the same substrate and extract an error that can be applied to devices made using this process sequence. A photograph of this device is given in Figure 5-8 (a) and the JV and CV parameters is given in Table 5-1. It is apparent that a maximum error of 10% is seen in device J_{SC} and N_{CV} , while the rest of the parameters show an error <1%. This 10% error in J_{SC} and N_{CV} is consistent with an expected error of 10% in cell area, measured using a calibrated computer scan. Considering that J_{SC} and N_{CV} are measured using two different measurement systems, it is unlikely for the source of this 10% variability to arise from the instrumental setup. Given the linear dependence of J_{SC} and N_{CV} with device area, it is likely for this error to arise from cell area measurement.



Figure 5-8: Photograph of a coupon (measuring ~1" long) processed with 4 devices of ~8 mm² area

Table 5-1: JV and CV parameters of devices made on a VTD-grown CdTe:Sb coupon (shown in the photograph of Figure 5-8) to demonstrate variability in devices studied in this work. From the table on that right, it is apparent that the maximum variability is seen in the device J_{SC} by ~10% error

Device #	V_{oc} (V)	J_{sc} (mA/cm ²)	FF (%)	η (%)	N_{cv} (cm ⁻³)
1	0.599	3.78	39.0	0.9	2.8×10^{13}
2	0.594	4.25	38.7	1.0	3.1×10^{13}
3	0.590	4.62	39.2	1.1	3.2×10^{13}
4	0.583	4.79	39.5	1.1	3.6×10^{13}
Average	0.591	4.36	39.1	1.0	3.2×10^{13}
Standard Deviation	0.006	0.45	0.3	0.1	3.3×10^{13}
Normalized deviation (%)	1.0	10.3	0.9	9.7	10.4

5.4 Applied Device Model

The equivalent circuit model employed for all device analysis performed in this work is given in Figure 5-9. This equivalent circuit consists of 2 diodes of opposite polarity in series. As discussed in Chapter 1, it is expected for all the diagnostic devices to have a blocking contact with CdTe due to the expected electron affinity-work function difference between the CdTe semiconductor and the carbon metal contact. For ideal metal/semiconductor junctions (which is not necessarily the case for the devices discussed in this work but serves as a close approximation for analytical purposes), the barrier height is given as the difference between the metal work function (Φ_M) and the semiconductor's electron affinity (χ_{CdTe}), which when negative creates a blocking contact, given by equation (5-1). The corresponding band diagram between CdS/CdTe/C layers is shown in Figure 5-10.

$$\Phi_C = \Phi_M - \chi_{CdTe} \quad (5-1)$$

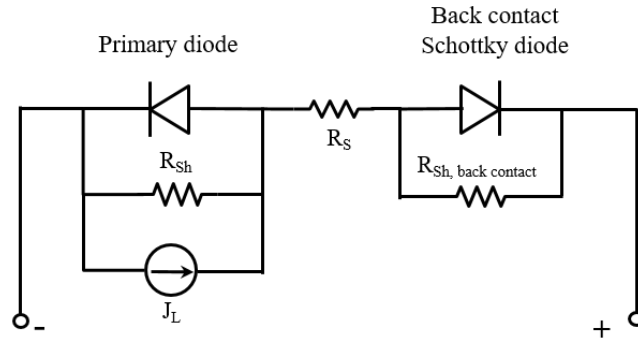


Figure 5-9: Equivalent circuit model of diagnostic CdTe:Sb devices.

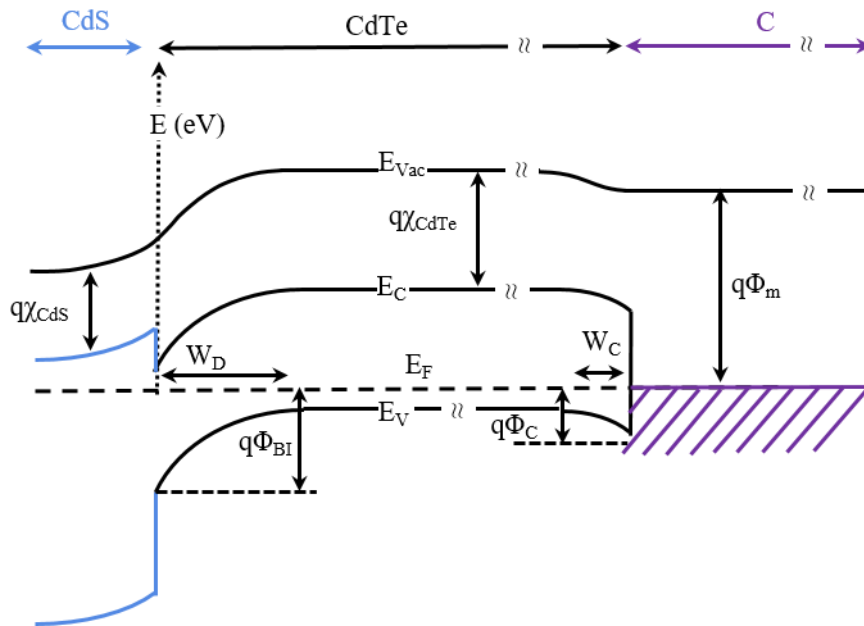


Figure 5-10: A qualitative representation (distance and energy axes are not to scale) of equilibrium band diagram (dark, no applied bias) of diagnostic devices corresponding to the CdS/CdTe/C stack. The junction between CdTe and the p-type contact (CdTe/C) is expected to be a blocking barrier since Cu-doping was not performed on these diagnostic devices to ameliorate the $\Phi_{BI} > \Phi_C$ in real devices.

Consequently, all the characterization techniques used for analyzing these devices are subject to the device models given by the equivalent circuit given in Figure 5-9 and band model shown in Figure 5-10. Section 5.5 of this chapter provides a brief overview of all the electrical characterization techniques and the corresponding analysis methodologies employed in this work to study diagnostic CdTe:Sb devices using example measurements.

5.5 Suite of Device Measurement Techniques Used

5.5.1 JV measurement

As described in Chapters 1 and 2, initial current density-voltage (JV) measurements are performed on all devices to obtain their most important solar cell parameters: V_{OC} , J_{SC} , FF, and η . Important qualitative information is obtained from the shape of the JV curve especially in forward bias regarding the blocking contact. For well-behaved devices that can be subject to single-diode equivalent circuit model (unlike the circuit model appropriate to the devices discussed in this work, given in Figure 5-9), a lumped parameter estimate of their equivalent series resistance, shunt conductance and ideality factor, recombination saturation current density can also be extracted using their JV curves. [94]

5.5.2 Capacitance-Voltage Sweep

A room temperature capacitance voltage (CV) sweep is performed on all devices to screen for the effective hole density achieved from extrinsic doping. The capacitance of a one-sided step junction measured as a function of the dc voltage can be used to estimate carrier/doping density, N_{CV} , by attributing the measured charge response to originate in the space-charge region of the base layer, CdTe:Sb. Considering that the

CdS emitter layer of the devices studied in this work is very thin (<20 nm) in comparison to that of the base layer (~10 μm), applying a one-sided step junction model to this measurement is appropriate. Consequently, the slope of a plot of $1/C^2$ vs. the reverse bias dc voltage (known as ‘Mott-Schottky’ plot) gives an estimate of the doping concentration at the edge of the depletion width. For non-ideal devices with non-negligible series resistance and/or a blocking contact, however, the $1/C^2$ vs. V_{dc} plot is not linear but varies in different regions. For this reason, an alternative way of extracting carrier density is used here, given by equations (5-2) and (5-3). These equations essentially calculate instantaneous slope at each voltage, $\frac{d(\frac{1}{C^2})}{dV_a}$, and plot this as a function of inverse capacitance which is equivalent to the profiling distance, given by x in equation (5-3).

$$N_{CV}(x) = - \frac{2}{q\epsilon_{CdTe} \left[\frac{d(\frac{1}{C^2})}{dV_a} \right]} \quad (5-2)$$

$$x = \frac{\epsilon_{CdTe}}{C} \quad (5-3)$$

5.5.2.1 Limitation to capacitance measurement

Agilent 4284A (20 Hz-1MHz) Precision LCR meter[®] was used to measure capacitance of devices studied in this work. The equivalent circuit mode of the device under test provided to this instrument for admittance measurement is given in Figure 5-11. Using this circuit mode, the LCR meter separates the real and imaginary parts of the measured admittance ($Y = G_{SH} + j\omega C$) and attributes the susceptance (the imaginary part of the measured admittance) to the equivalent device capacitance, $C = \text{Im}\left(\frac{Y_{meas}}{\omega}\right)$. At large forward bias voltages ($V_a \gg \frac{kT}{q}$), the dynamic resistance of the diode reduces significantly, increasing the equivalent shunt conductance across from

the diode capacitance. This leads to a significant increase in the dissipation factor, D , which is the ratio of susceptance from the shunt conductance (G_{sh}) and the capacitance (ωC), $D = \frac{G_{sh}}{\omega C}$, causing the instrument to read erroneous equivalent capacitance values. [95] For these reasons, capacitance values read at large forward (dc) biases are typically inaccurate and are not considered for analysis.

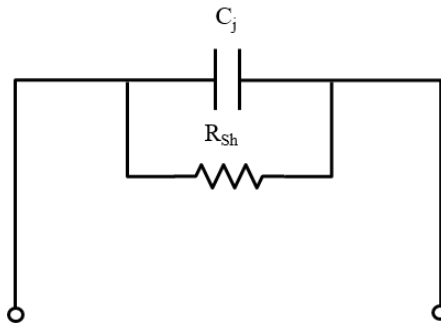


Figure 5-11: Equivalent circuit mode of the device under test (solar cell) provided to the LCR instrument for capacitance measurement

For the reason stated above, in addition to a presence of a non-negligible series resistance and/or a blocking contact in the equivalent circuit of the device, the measured $C(V)$ curves of solar cell devices display a characteristic ‘peaking behavior’ at large forward biases, leading to an apparent U-shape in the carrier density profiles generated using equation (5-2). [36] This feature is exaggerated in the presence of deep defects in the device that respond to low measurement frequencies. [96] Consequently, the doping density estimation is made from the low forward bias region of the Mott-Schottky plot, or from the minimum of the carrier profile curve (N_{cv} vs. x), as shown in Figure 5-12 (b).

Figure 5-12 (a) shows as an example, measured CV plots of a set of diagnostic CdTe:Sb devices. This plot shows CV curves of (i) a device made from an as-deposited CdTe:Sb substrate, (ii) a device made from a CdTe:Sb substrate that received Cd-vapor ‘activation’ treatment described in section 5.3.1, (iii) a device made from a film that received both Cd-vapor treatment and CdCl₂ device anneal. Figure 5-12 (b) gives the corresponding doping density profiles for all these devices by plotting N_{CV} profile from equation (5-2). Notice that the treated devices show a substantially higher N_{CV} than the device processed with the as-deposited CdTe:Sb film.

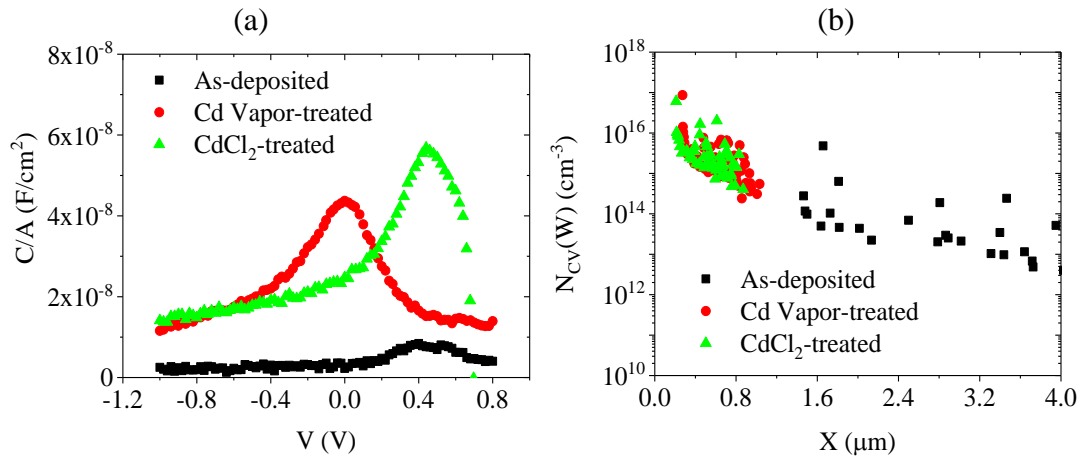


Figure 5-12: (a) Raw C(V) data and (b) corresponding carrier density profiles of a sample set containing CdTe:Sb diagnostic devices made from CdTe films (i) as-deposited, (ii) with Cd vapor treatment, and (iii) with both Cd-vapor treatment and CdCl₂ device anneal.

5.5.3 Admittance Spectroscopy

The capacitance measured as a function of measurement frequency and temperature, often called admittance spectroscopy, can provide information about the charge response arising from the filling and emptying of traps with transition energies

between the Fermi level and mid gap, in the absorber material by the edge of the depletion region. [97] It can also provide information about the series resistance.

The raw admittance spectroscopy data of an example CdTe:Sb device is shown in Figure 5-13 (a), where the characteristic step in capacitance is apparent at every temperature. This drop in capacitance with increasing frequency is seen at every temperature and arises from a ‘freeze out’ of defects in the absorber, whose relationship with temperature and frequency is given in equation (5-4), where E_ω is the energy corresponding to the measurement frequency, ω_0 , and measurement temperature, β_p is ‘attempt to escape velocity’ of the trap, given as a product of its capture cross section (σ_p) and the carrier thermal velocity ($v_{th,p}$). [97]

$$E_\omega - E_V = kT \ln \frac{2\beta_p N v}{\omega_0} \quad (5-4)$$

This change in charge response can be seen more clearly in the fdC/df (or $\omega dC/d\omega$) plots given in Figure 5-13 (b). Using the inflection frequencies taken at each temperature from the fdC/df plots, an Arrhenius plot is made (Figure 5-13(c)). The slope of this plot gives an activation energy, E_a , which according to equation (5-4) would be the transition energy of the trap. For devices with a blocking barrier, such as those studied in this work, the charge response can also arise from thermalization (thermionic emission) of carriers over the blocking barrier, leading to the extracted E_a with the Schottky barrier (more details in Section 6.5.3.3). In devices where the dopant transition energy in the absorber is deep ($> kT/q$), this energy can also be attributed to the resulting ‘carrier freezeout’. [97] [98] It is important to note also that the charge response analysis studied using this measurement technique requires that the dielectric relaxation time of the absorber, τ_σ , given by equation (5-5), is much less than the

oscillation time period corresponding to the ac frequencies at which capacitance measurements are performed, $\frac{1}{\omega_0}$.

$$\tau_\sigma = \frac{\epsilon}{\sigma} \quad (5-5)$$

$$\tau_\sigma \ll \frac{1}{\omega_0} \quad (5-6)$$

where ϵ is the dielectric permittivity of the semiconductor and σ is its conductivity, given by $\sigma = qn\mu_e + qp\mu_h$, with q representing electronic charge, n , p representing electron and hole concentrations, $\mu_{e/h}$ representing electron/hole mobility. The dielectric relaxation time calculated for CdTe using equation (5-5) with parameters taken from reference [116] is ~ 34 ps, which satisfies this condition (equation (5-6)) for the measurement frequencies used in this study, 1KHz- 1MHz.

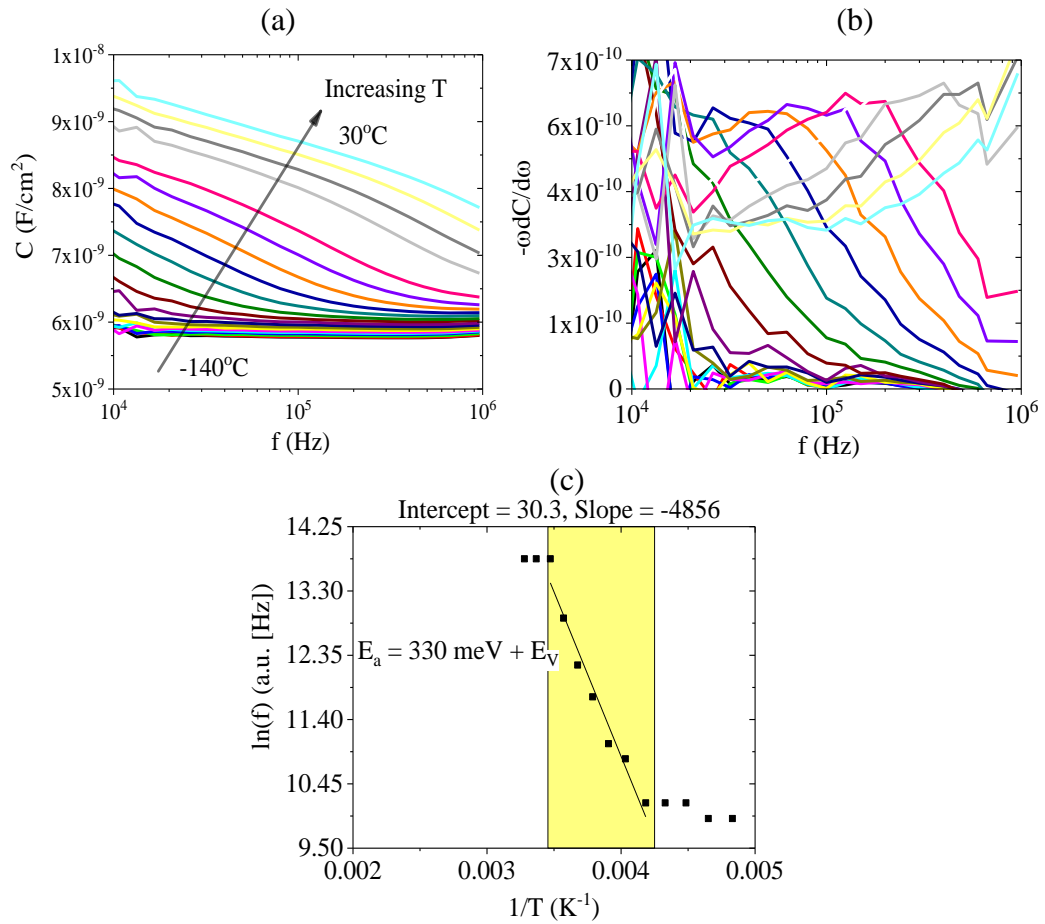


Figure 5-13: (a) Raw data of admittance spectroscopy taken at 0V dc bias. This consists of capacitance vs. frequency measured at different temperatures from -140°C to $+30^\circ\text{C}$ in $\sim 10^\circ\text{C}$ step size (b) a plot of the derivative of capacitance vs. frequency to find the inflection capacitance as a peak of this curve (c) Arrhenius plot of the inflection frequencies, whose slope gives an activation energy of the charge response, that can be potentially attributed to multiple factors. These include a recombination center in the absorber material, the barrier height of a blocking contact, if applicable, or carrier freezeout [97], as dictated by equation (5-4).

5.5.4 JV(T)

Temperature-dependent current-voltage measurements, $JV(T)$, can be performed both under illumination and in the dark. They are a versatile resource to

extract the activation energy, E_a , that can provide important information regarding device recombination and blocking barrier potential, discussed below.

5.5.4.1 JV(T) Light

A plot of V_{OC} as a function of temperature using JV data measured at different temperatures can be used to extrapolate V_{OC} at 0K. Since there is no current flowing at V_{OC} , $V_{OC}(T)$ can facilitate an understanding of loss mechanisms in pn junction diodes without the effects from series resistance and blocking contact-related losses. This is useful to extract ‘activation energy’ of the reverse saturation current in the device, given by the following equations, [77], [99]

$$J_0 = J_{00} \exp\left(\frac{E_a\{R^n\}}{kT}\right) \quad (5-7)$$

$$V_{OC} = \frac{nkT}{q} \ln\left(\frac{J_{SC}}{J_0(T)}\right) \quad (5-8)$$

$$qV_{OC} = E_a\{R^n\} + nkT \ln\left(\frac{J_{SC}}{J_{00}}\right) \quad (5-9)$$

where T is cell temperature in Kelvin, J_0 is the reverse saturation current density, $E_a\{R^n\}$ depicts the activation energy of recombination, J_{00} is the temperature-independent reverse saturation current density. If $V_{OC}(0K) = E_a\{R^n\} = E_g$, then this means that the recombination in the device is radiative-limited, suggesting a well-behaved device with negligible traps in the bulk of the absorber. Otherwise ($E_a\{R^n\} < E_g$), this could mean that the recombination current is dominated by trap-assisted Shockley-Read Hall (SRH) recombination in the bulk of the absorber or at the pn junction interface.

Figure 5-14 shows example $V_{OC}(T)$ plots of those devices from a similar sample set as described in Section 5.5.2. The extracted $E_a\{R^n\}$ or $V_{OC}(0K)$ of the ‘As-deposited’ device and ‘Cd-vapor treated’ devices were ~1.23 eV and 1.34 eV respectively, suggesting that their V_{OC} ’s are interface recombination-limited as given

by equation (5-7). On the other hand, the device that received both Cd-vapor treatment and CdCl₂ treatment shows an E_a of 1.47 eV which is close to its E_g, suggesting that its V_{OC} is bulk-recombination-limited.

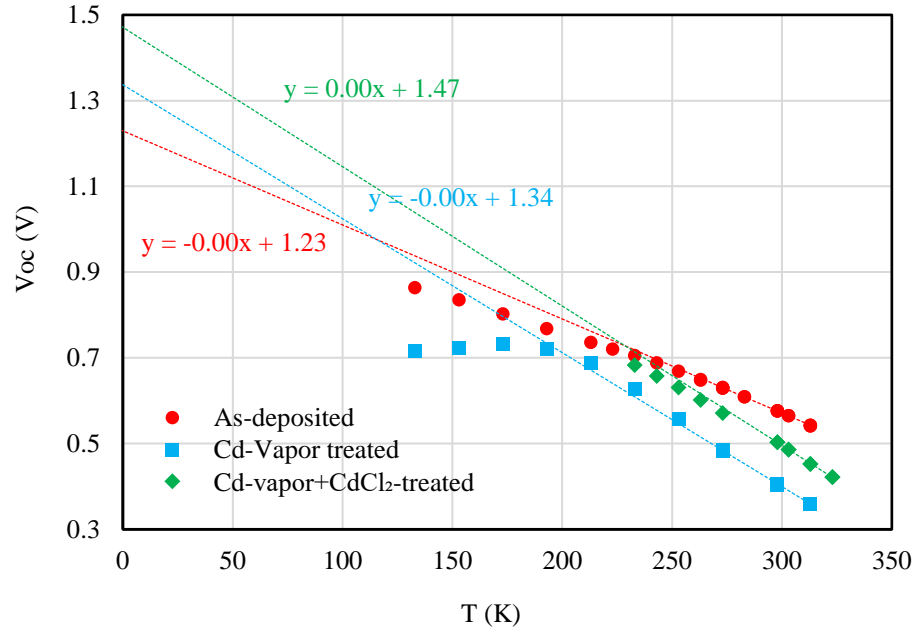


Figure 5-14: A plot of measured V_{OC} as a function of temperature, shown here being used to extrapolate V_{OC} (0K)

5.5.4.2 JV(T) Dark

JV measurements as a function of temperature performed in the dark can be used to extract the Schottky barrier potential of the blocking contact. [100], [101], [102] It is well known that JV curves of those devices with a severe blocking contact display a characteristic ‘S-shape’, or a ‘cross-over’ [103] of light and dark JV curves, or a ‘roll-over’ in the high forward bias region. [36] Exactly how much the presence of a blocking contact affects the JV behavior of a device in the light and thereby reduce its FF depends

on several factors including: (i) blocking barrier potential (ii) blocking diode's equivalent saturation current density, J_{C0} , (iii) shunt conductance across the blocking diode. The effective JV curve of the whole device can be an intricate function of these lumped parameters that their exact extraction is not only quite challenging but also limited to the exact diode current-voltage model used. In other words, quantifying these parameters is contingent upon the model and does not necessarily provide a useful and objective deduction pertaining to a specific physical quality of the device.

It is well known that the best of CdTe solar cells exhibit a slight blocking barrier at the p-type contact, but this does not affect the device's JV curve in the power-quadrant (3rd quadrant), thereby leaving the FF largely unaffected. Typically, barrier potentials of up to 300 mV are tolerable in baseline devices without significantly affecting the FF, at least at room temperature, since the impact of a back barrier increases at very low temperature. Extraction of barrier potential in this work is carried out using the contact resistance method proposed by Phillips & McCandless [100] in those devices exhibiting JV curves without a significant 'light-to-dark cross-over', where the dark JV curve intersects the light JV curve in high forward bias. In devices with an apparent roll-over, a 'turning current' Arrhenius behavior method [102] was used to extract the barrier potential.

Figure 5-15 (a) shows raw data of a CdTe:Sb device as an example. In Figure 5-15 (b), a plot of dV/dJ vs. $1/J$ is shown, which is used to extract series resistance at large forward bias voltages for different measurement temperatures. [77] At forward bias, near V_{OC} of the primary junction, the total device current is dominated by the reverse saturation current of the blocking contact (leading the 'roll-over'). Assuming a negligible voltage drop at the blocking contact ($V_C \ll kT/q$), the series resistance at large

forward bias is given as the ratio of the reverse saturation current of the blocking diode and the thermal voltage (kT/q). Given that the reverse saturation current of the blocking diode has an exponential dependence on its barrier height, [104], an Arrhenius plot of the series resistance yields the barrier height of the blocking contact. This procedure is discussed in detail by Phillips, *et al.* in ref. [100].

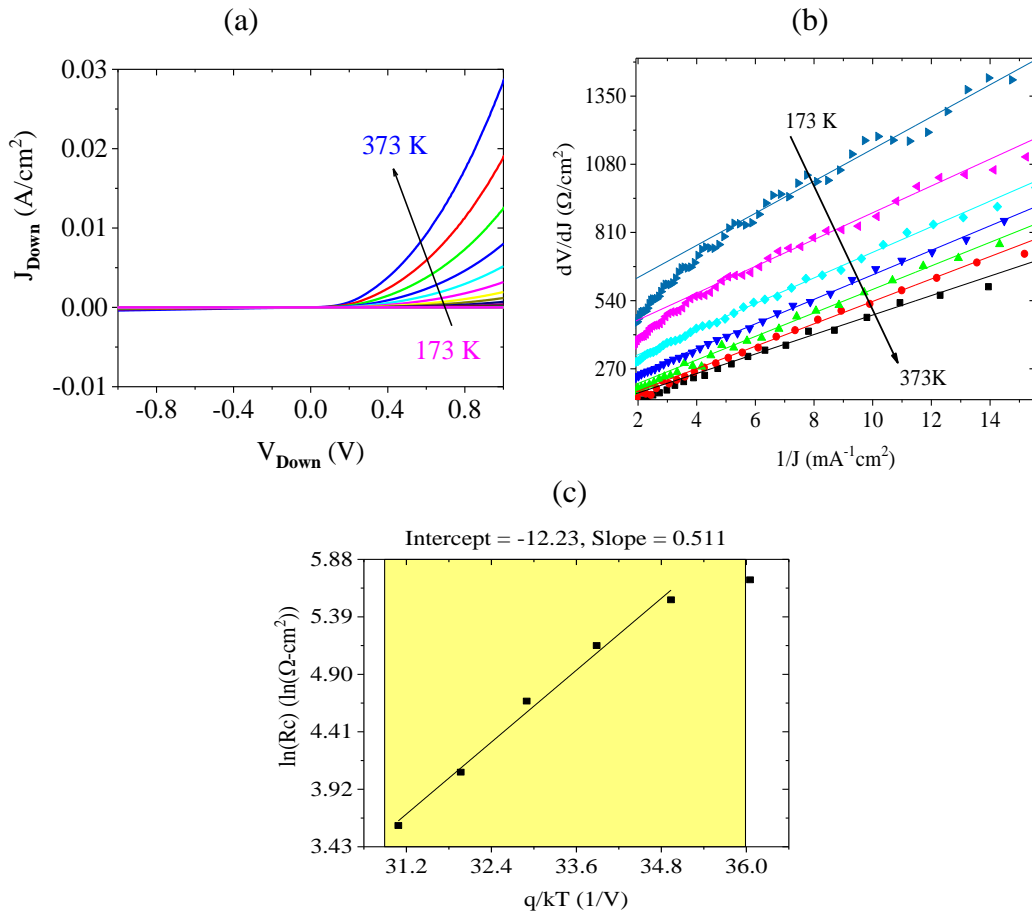


Figure 5-15: (a) JV(T), Dark raw data of a device given for demonstration of barrier potential extraction (b) a plot of dV/dJ vs. $1/J$ for series resistance extraction from large forward biases. [77] Using this, the contact resistance (R_C) is calculated for different temperatures (c) Arrhenius plot of R_C for estimation of an activation energy that serves as an estimate of the blocking barrier potential [100]

5.5.5 Quantum efficiency:

Quantum efficiency (QE) measurements were used in this work to estimate the bandgap of the polycrystalline CdTe:Sb material in the devices. For photovoltaic devices, quantum efficiency is defined as a ratio of ‘carriers out’ to ‘photons in’, given by equation (5-10) below, by using spectrally resolved photocurrent measurements.

$$QE = \frac{\text{\# of carriers collected}}{\text{\# of incident photons}} \quad (5-10)$$

The shape and magnitude of the QE provides information about the solar cell’s optical and electronic properties. In this work, the long wavelength QE was used to extract absorber material E_g . [105] [106] using equation (5-11), neglecting any band tailing or potential fluctuations in the absorber. [107] E_λ in equation (5-11) represents photon energy of long wavelength light. This method of obtaining E_g from devices has been validated by comparing it to values from variable angle spectroscopic ellipsometry (VASE) at the IEC using CuInGa(Se)₂ alloy pn junction devices with a wide range of absorber bandgaps.

$$E_g \approx E_\lambda \text{ at } \max \left\{ \frac{d(QE)}{d(E_\lambda)} \right\} \quad (5-11)$$

Figure 5-16 (a) shows QE data for two CdTe:Sb devices as example, one with Cd vapor anneal alone (‘Cd vapor-treated’) and one with Cd vapor anneal and CdCl₂ anneal (CdCl₂-treated). The absorber bandgaps of these two devices estimated using equation (5-11), shown in the plot of Figure 5-16 (b) were similar: 1.49 eV for the ‘Cd-vapor treated’ device and 1.48 eV for the device that received Cd vapor and CdCl₂ treatments. The CdTe absorber band gap is reduced slightly by interdiffusion with CdS from the interface, owing to a bowing parameter in the alloy CdTe_{1-x}S_x.

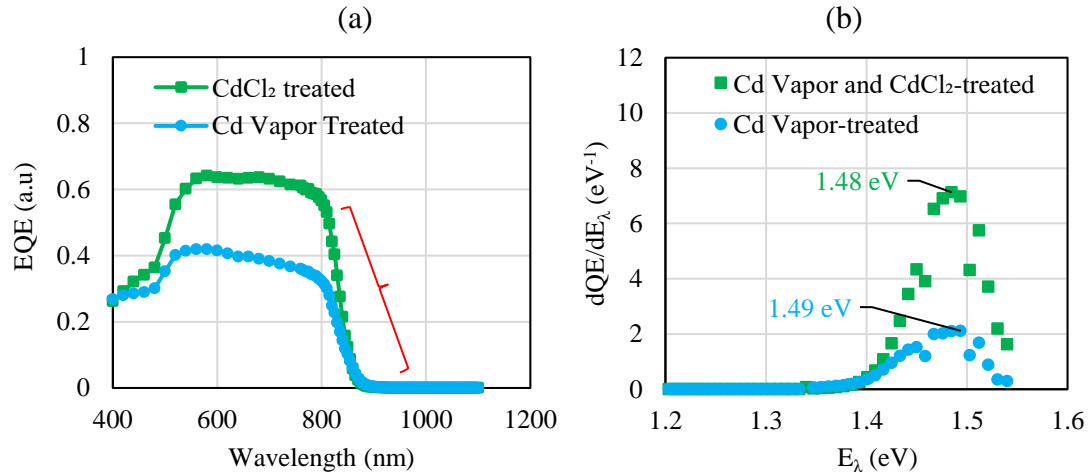


Figure 5-16: (a) QE data for two Sb-doped devices: with and without device anneal treatment. (b) dQE/dE_{λ} plots to extract absorber bandgap for these two devices

5.5.6 JV(Illumination-G)/ Suns V_{OC} :

A solar cell's JV behavior measured as a function of illumination intensity can be used to extract the ideality factor (n) and reverse saturation current density, J_0 , by plotting it as qV_{OC}/kT vs. $\ln(J_{SC})$ using equation (5-12).

$$\frac{qV_{OC}}{kT} = n[\ln(J_{SC}) - \ln(J_0)] \quad (5-12)$$

V_{OC} (G) data of an example device is given in Figure 5-17(a), from which a qV_{OC}/kT vs. $\ln(J_{SC})$ plot is made in Figure 5-17(b), this device the ideality factor was estimated to be ~ 1.93 , indicating that dominant recombination mechanism is Shockley-Read-Hall (SRH), primarily in the depletion region. [108] Its reverse saturation current density was estimated to be 1.6×10^{-5} mA/cm².

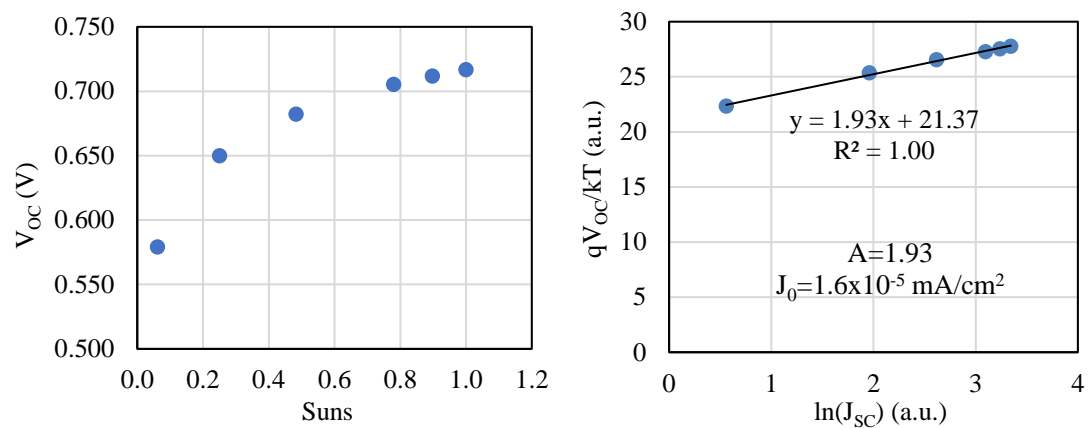


Figure 5-17: (a) A plot of V_{OC} as a function of solar intensity ('Suns'), (b) plotted as $\ln(J_{SC})$ vs. qV_{OC}/kT to extract ideality factor n and reverse saturation current density, J_0 , using equation (5-12).

5.6 Summary

This chapter discussed the process sequence of making thin film CdTe:Sb solar cells from glass substrates using various thin film deposition techniques. This description is specific to the device architecture employed for diagnostic CdTe solar cells doped with Sb. A few of the processes differ for state-of-the-art CdTe solar cell fabrication, such as rear contact processing. This is necessary to avoid complicating or obscuring the interpretation of the doping density but unfortunately results in a non-ideal Schottky-type rear contact.

A brief overview of the various device characterization techniques was also provided here, along with a description of the corresponding analysis techniques for parameter extraction and their limitations, using example devices. This chapter thus provides the necessary context to understand a more detailed analysis of actual devices of interest, discussed in Chapters 6 and 7. While CV sweep, admittance spectroscopy and $JV(G)$ are the most important measurements used for device analysis in this work, the results from the rest of the measurements such as QE and $JVT(L)$ were used to extract parameters that were used to supplement the more important aforementioned analysis techniques.

Chapter 6

ANALYSIS OF ANTIMONY-DOPED DEVICES AND EVALUATING DEVICE TREATMENT TECHNIQUES

The emphasis of this dissertation is to evaluate the action of well-known CdTe device treatment techniques to Sb-doped devices. The concept of post-deposition treatments is invoked to provide electronic activation of the dopant, since growth rate with VTD can be too high for the deposited CdTe:Sb film to remain at high temperature for sufficient duration to ensure activation. Sb incorporation using this growth technique was successfully demonstrated (as discussed in Section 5.2.3.1), considering the requirement of high growth rate for commercially viable VTD growth of CdTe for thin film PV. It would not be surprising that additional thermal processing may be necessary to modify the defect content, ensure p-type dopant activation, and to generally improve film and device quality by reducing intra-grain defects (commonly achieved using CdCl₂) and passivating surfaces (combining CdCl₂ and oxygen), as discussed in Section 5.3.2. In fact, the different specific processes explored here are those that have become essential for intrinsic CdTe to achieve high quality devices but have hitherto unknown effects on Sb-doped films. For example, treatment in oxygen ambient might improve doping density but not necessarily the carrier lifetime. [83] [90] The desired outcomes from exploring the post-processing treatment techniques is to (i) achieve a near-100% dopant activation while (ii) maintaining film quality by realizing a sufficient minority carrier lifetime, by (iii) mitigating defect formation by minimizing the defect formation from un-activated dopant species in the device, as given in Table 6-1.

In addition to screening the applicability of these treatment techniques for CdTe:Sb solar cells, this work also focuses on analyzing the voltage deficit in these extrinsically doped devices by employing several electrical characterization techniques.

In the previous chapter, a brief discussion of device anneals in conventional undoped CdTe photovoltaics was provided. However, application of the same knowledge, hypotheses and methodologies might not be straightforward for extrinsically doped CdTe solar cells. Consequently, a systematic study of these device anneal treatments was pursued to specifically isolate the effect of CdCl₂ and O₂ in the treatment ambient. A matrix of 4 anneal treatments on CdTe:Sb diagnostic devices was designed (given in Table 6-2) using coupons cut from a plate containing $5 \times 10^{16} \text{ cm}^{-3}$ Sb loading. These devices were studied in comparison to a baseline, ‘undoped’ (intrinsically doped p-type) CdTe solar cell. Sb-doped sample ‘0’ was processed on a coupon that received no Cd-vapor treatment to be compared with samples 1-4, whose absorber films have all received this activation treatment. Samples 1-4 are used to study the effect of O₂ and CdCl₂ in the device anneal ambient. While sample #1 received O₂ and sample # 2 received CdCl₂ vapor exclusively, samples #3 and #4 have both air and CdCl₂ vapor in their anneal ambient. Samples 3 and 4 differ in the way in which CdCl₂ was delivered to the exposed CdTe:Sb surface: while sample #3 has CdCl₂ delivered as a vapor, it was delivered as a coat for sample #4 (as discussed in Section 5.3.2). Each of the anneal treatments for Sb-doped devices was also studied as a function of temperature. The anneal temperature for all Sb-doped devices was varied between 375, 400 and 425°C. However, only the temperatures that yielded the best doping density (N_{CV}) for each of the treatments were studied in this work and are given in Table 6-2. The anneal duration for group V-doped devices was optimized independent of this study to be 60 min.

Section 6.1 evaluates these treatment techniques on Sb-doped devices in terms of their key performance parameters from JV and CV measurements and makes deductions about the effect of the different species present in the anneal ambient.

Section 6.2 discusses the V_{OC} deficit in all these devices by applying the different characterization techniques described in Chapter 5, with Section 6.3 summarizing the study.

Table 6-1: Expected benefits from post-deposition treatments

Treatment	Cd-vapor	Air	CdCl ₂
Known benefit	Enhance carrier density of Sb-doped CdTe films by creating Te vacancies (V_{Te}) in CdTe lattice	Increase hole concentration by promoting Cd vacancies (V_{Cd}) in conventional intrinsically-doped CdTe films and oxidize interstitial Cd	Carrier lifetime enhancement by (i) reduced crystallographic defects, (ii) passivating CdS/CdTe interface

Table 6-2: The anneal matrix used to evaluate the effect of CdCl₂ and Air in the anneal ambient on CdTe:Sb diagnostic devices.

Sample #	Doping	Cd-Vapor Anneal	Anneal Ambient		Anneal Temperature (°C)
			Air	CdCl₂	
U	Intrinsic	NA	Y	Vapor	400
0	Sb	N	-	-	-
1	Sb	Y	Y	-	425
2	Sb	Y	-	Coat	400
4	Sb	Y	Y	Coat	375
3	Sb	Y	Y	Vapor	400

6.1 Evaluation of Devices from Anneal Matrix with JV and CV Measurements

All Sb-doped solar cells from the anneal matrix presented in Table 6-2 were screened for their device parameters using JV and CV measurements. A SIMS measurement of the film used to make these devices has shown Sb incorporation of $5 \times 10^{16} \text{ cm}^{-3}$, which establishes the upper limit on Te substitution acceptor levels. The JV curves of all these devices are given in Figure 6-1, and the corresponding device parameters including N_{CV} (representing the free carrier density and defined in equation (5-2)) are given in Table 6-3.

A graphical representation of these device parameters is given in Figure 6-2. We note again that these devices lacked the complete sequence of chemical and thermal processing which are now commonly applied to make a high efficiency CdTe solar cell. In particular, they lack a Cu-doping step to create an ohmic back contact and high FF because the Cu atoms are known to diffuse rapidly and dope the entire CdTe film. This would interfere with characterizing the impact of the Sb-doping. Thus, these test structures have a severely limited FF ~ 25%.

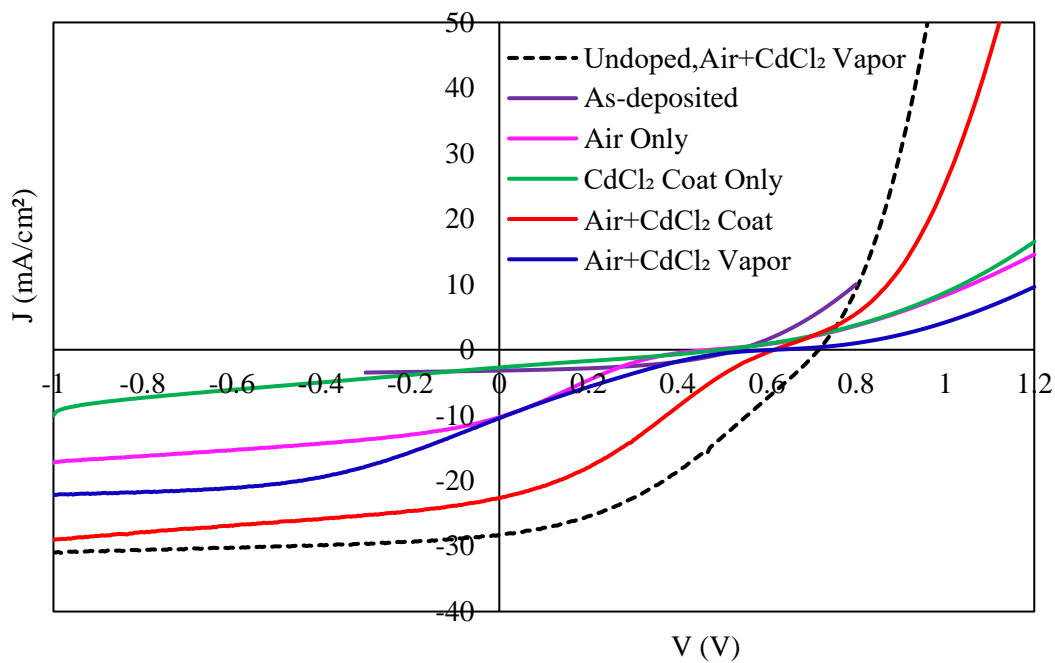


Figure 6-1: JV curves of devices from the anneal matrix, with an apparent S-shape for all the devices indicating the presence of a blocking contact. The dashed and the blue curves can be directly compared as they have received similar device anneal treatments ('Air+CdCl₂ vapor'). It can be seen that Sb-doped ('Air+CdCl₂ vapor') device has a severe 'S'-shape, indicating the presence of a leaky blocking contact. It also exhibits a lower V_{OC} , J_{SC} and FF than the baseline device.

Table 6-3: JV and CV Parameters of devices from the anneal matrix. V_{oc} , J_{sc} , FF and η are from illuminated JV measurements at STC. N_{cv} is obtained from CV measurements at 0.5 MHz.

Parameter	Measurement	Undoped	Sb-doped				
		Air+CdCl ₂ Vapor	As- deposited	Air Only, No CdCl ₂	CdCl ₂ coat Only, No Air	Air+ CdCl ₂ coat	Air+ CdCl ₂ Vapor
V_{oc} (mV)	JV	717	561	474	500	617	619
J_{sc} (mA-cm ⁻²)	JV	28.3	6.4	10.3	2.7	22.7	10.5
FF (%)	JV	36.7	23.1	19.5	27.9	29.7	18.0
η (%)	JV	7.4	0.8	1.0	0.4	4.2	1.2
N_{cv} (cm ⁻³)	CV at 0.5 MHz	2.8×10^{14}	6.7×10^{13}	3.7×10^{15}	3.3×10^{13}	1.2×10^{15}	4.4×10^{14}
n	JV(G)	1.93	-	1.57	3.42	3.57	2.14
J_0 (mA-cm ⁻²)	JV(G)	1.6×10^{-5}	-	8.0×10^{-5}	7.5×10^{-3}	2.5×10^{-2}	1.4×10^{-4}
V_{oc} (0K) (mV)	JV(T) Light	1.28	-	0.94	1.39	1.33	1.32
E_g (eV)	QE	1.48	-	1.44	1.48	1.48	1.46

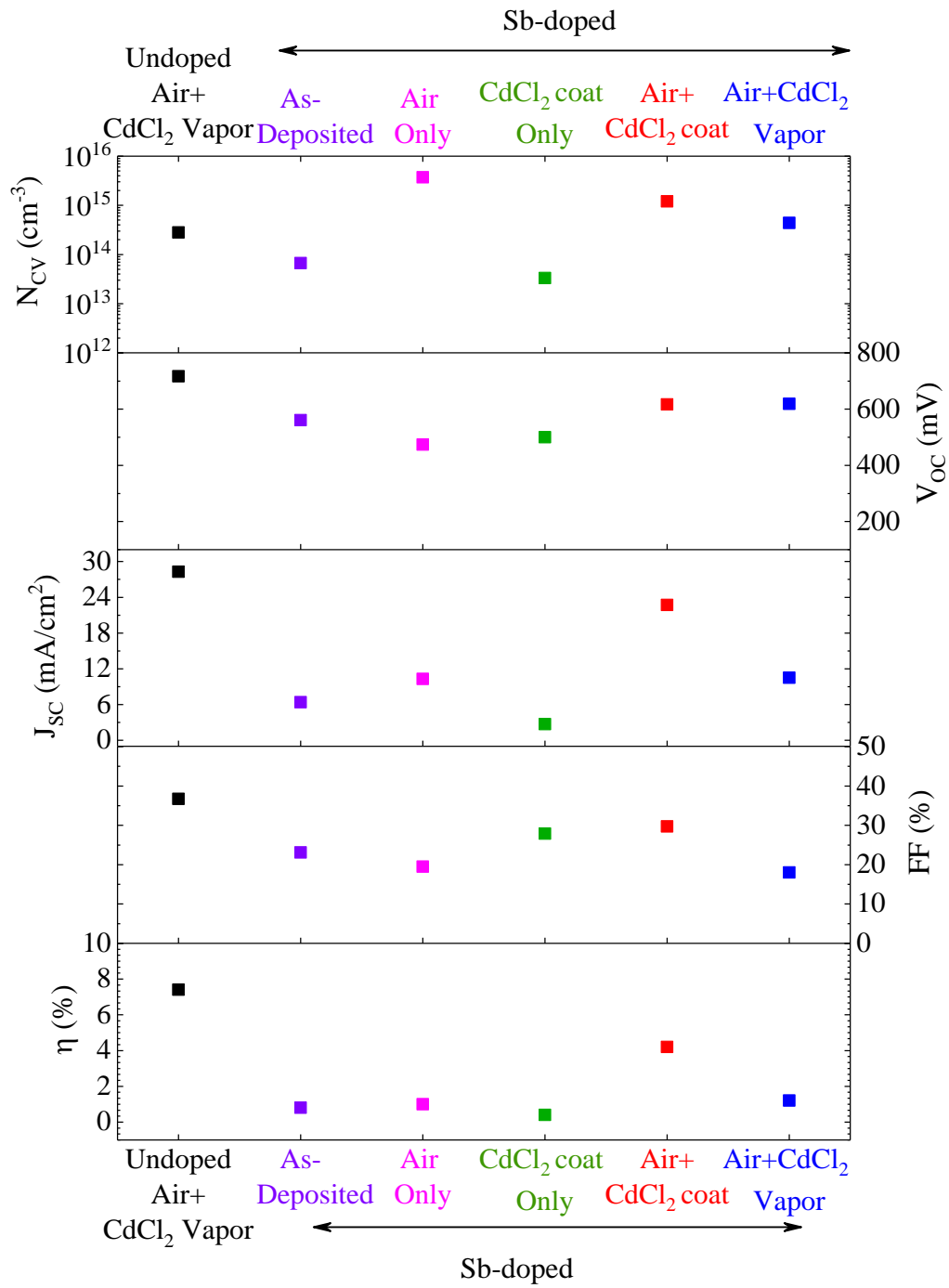


Figure 6-2: Tabulated JV and CV parameters of CdTe:Sb devices from the anneal matrix shown pictorially for comparison

6.1.1 Interpreting results from device measurements

The JV curves (Figure 6-1), JV and CV data (Table 6-3) allow the following interpretations:

(i) all devices have a significant blocking barrier (evident as a strong ‘S’ shape in their JV curves and low FF)—as expected considering they did not receive Cu-alloying at the p-type contact (as discussed in Chapters 1 and 5). On fully optimized conventional devices with undoped CdTe bulk and Cu-alloy-doped back contact processed at IEC, values of $V_{OC} > 830$ V, and $FF > 81\%$ have been obtained without any suggestion of the ‘S’-curvature,

(ii) Sb-doping can increase the carrier density by as much as an order of magnitude (i.e., N_{CV} increased from $\sim 3 \times 10^{14}$ to 4×10^{15} cm^{-3} in the Sb-doped devices compared to the ‘Undoped’ devices both with air anneal), and can yield functional solar cell devices,

(iii) increased carrier density, however, did not translate to increased photovoltage (V_{OC}) which was the essential question we sought to answer,

(iv) ‘Air+CdCl₂ Coat’ resulted in an 18x increase in carrier density over the Sb-doped untreated sample. It had the highest FF, highest current conduction in forward bias and least S-curvature suggesting the Sb-doping and treatment improved both the bulk and back-contact properties. A detailed evaluation of each of the treatment techniques is provided in the following subsections, and

(v) V_{OC} (0K) extracted from temperature-dependent JV measurements in light of all Cd-vapor-treated Sb devices and the baseline undoped device are lower than the bandgaps extracted from their QE, suggesting that the V_{OC} ’s are limited by non-radiative recombination, which could arise from deep defects in the CdTe bulk or at CdTe/CdS interface. Large values of recombination current density, J_0 and ideality

factors ~ 2 (extracted from intensity-dependent JV measurements) are consistent with this result.

6.1.1.1 Effect of Cd-vapor treatment

Table 6-3 and Figure 6-2 show that the device made from an ‘as-deposited’ CdTe:Sb film has very low carrier density, given by its $N_{CV} \sim 7 \times 10^{13} \text{ cm}^{-3}$. The N_{CV} of the rest of the Sb-doped devices, whose CdTe films received the Cd-vapor treatment, is much higher, reaching $\sim 4 \times 10^{15} \text{ cm}^{-3}$, yielding a doping efficiency of $\sim 8\%$. Similarly-doped CdTe:Sb films have shown high activation levels, with doping efficiencies $> 10\%$. [58]. This shows that Cd-vapor anneal performed in a sealed ampoule under Cd-over pressure (discussed in Section 5.3.1) activates the dopant atoms in the CdTe lattice to enhance acceptor (p-type carrier) density.

6.1.1.2 Effect of O₂ in the device anneal ambient

The effect of oxygen in the device anneal ambient can be deduced by the performance of the device that received only air in the anneal ambient- named as ‘Air only’ in the matrix. The N_{CV} of this device, $> 3 \times 10^{15} \text{ cm}^{-3}$, is much higher than that of the ‘Undoped’ or ‘As-deposited’ devices, indicating that oxygen in the treatment ambient enhances carrier density. This is consistent with studies showing the benefit of introducing O₂ during intrinsic CdTe film growth. [90] This increased N_{CV} , however, does not translate to an increase in V_{OC} , given that this device has a low voltage output—of 474 mV. This device has a moderate J_{SC} among the Sb-doped samples, of 10.3 mA/cm^2 , (similar to ‘Air+CdCl₂ vapor’ device) which although higher than that of the ‘As-deposited’ device, is less than half that expected for CdTe cells on this window stack.

6.1.1.3 Effect of CdCl₂ in device anneal ambient

The effect of CdCl₂ in the anneal ambient can be studied using the ‘CdCl₂ coat only’ device that received a concentrated delivery of CdCl₂ (where CdCl₂ dissolved in a solvent is placed as a droplet on the CdTe:Sb exposed film as discussed in Section 5.3.5) during its device anneal in the absence of air. It is evident from the initial results that this device has shown no improvement in N_{CV} over the ‘As-deposited’ sample, showing that CdCl₂ alone does not assist in dopant activation after a Cd-vapor anneal. This sample also exhibits a low J_{SC} of 2.7 mA/cm², indicating a poor carrier collection. This shows that CdCl₂ on its own cannot improve the quality of CdTe:Sb film, nor can it activate the dopants to enhance carrier density.

6.1.1.4 A combination of CdCl₂ and O₂ in the ambient

The devices that received both O₂ and CdCl₂ in the anneal ambient (‘Air+CdCl₂ coat’ and ‘Air+CdCl₂ vapor’) exhibit a higher device performance (V_{OC}, J_{SC} and η) than those that received O₂ or CdCl₂ exclusively. More specifically, the best of all the Sb-doped devices received this ‘Air+CdCl₂ coat’ treatment where the CdCl₂ was supplied as a solid by precipitation from a liquid methanol solution coating onto the exposed CdTe:Sb surface. This device has shown high carrier density of >1x10¹⁵ cm⁻³, sustained at sufficiently high film quality to ensure high V_{OC} and J_{SC} of 617 mV and 23 mA/cm², respectively. In contrast, the device which received CdCl₂ delivered as a vapor (‘Air+CdCl₂ vapor’) shows lower N_{CV} and J_{SC} of 4x10¹⁴ cm⁻³ and 10 mA/cm² respectively, indicating weak carrier collection.

Even though O₂-containing ambient improves carrier density as seen from an improved N_{CV}, the device behavior does not necessarily improve with oxygen in the ambient alone. The samples that received both O₂ and CdCl₂ exhibit a much better

device efficiency than the samples with ‘Air only’ or ‘CdCl₂ only’ ambient, suggesting that a combination of O₂ and CdCl₂ in the anneal ambient is required for Sb-doped devices—where O₂ improves carrier density and CdCl₂ improves device efficiency. A more detailed treatment of performance deficit in all Sb-doped devices which received device anneals is provided in Section 6.2.

6.2 Quantitative Analysis of Performance Deficit

6.2.1 J_{sc} losses

The ‘Undoped’ baseline device exhibited the maximum J_{sc} output >28 mA/cm². All the Sb-doped devices on the other hand exhibit very low J_{sc}’s despite being processed on IEC baseline window layer stack. This implies that the deficit in J_{sc} of these devices is not from optical absorption losses but due to poor collection of the light-generated carriers. This could either be from insufficient drift field or from severe recombination or a combination of the two. It is known that the presence of a uniform field of strength \mathcal{E} increases the ‘upstream’ diffusion length, L_{n+} , of carriers (whose non-field diffusion length is otherwise $L_n = \sqrt{D_n \tau_n}$), given by the following equation: [109]

$$L_{n+} \cong \left[\left(\frac{qL_n^2 \mathcal{E}}{kT} \right) + 1 \right]^{-1} = \left[\left(\frac{qD_n \tau_n \mathcal{E}}{kT} \right) + 1 \right]^{-1} \quad (6-1)$$

This equation demonstrates the significance of drift field strength and minority carrier lifetime for efficient carrier collection at the contacts. It provides an important relationship to understand the dependency of photocurrent collection on electric field. The electric field, $\mathcal{E}(x)$, in the depletion region of these devices drops linearly through the depletion width from maximum to zero, given by equation (6-2) below. Past studies have shown that the current collection most conventional CdTe devices is dominated by

field-aided drift than by bulk diffusion. [103] The equivalent boost in diffusion length from this field in the depletion region can be calculated using 1-D modeling to solve for the transport equation in these devices.

$$\mathcal{E}(x) = -\frac{q}{\epsilon_{CdTe}} N_a (x + W_d) \quad (6-2)$$

Note that equation (6-2) also demonstrates the benefit of increased doping density in the absorber, N_a , in terms of increasing the drift field in the depletion region for effective collection of carriers generated in the depletion region. Engineering thin-film pn junction solar cells to provide a built-in electric field in the quasi-neutral bulk by spatial variation of acceptor concentration is well-studied for a-Si devices. [110]

The Sb-doped devices with $>5 \times 10^{14} \text{ cm}^{-3}$ doping density would have sufficient built-in voltage and therefore the adequate electric field to provide the necessary drift to the light-generated carriers in the depletion region. At higher doping densities, with photocarrier generation occurring outside the shorter space-charge region, carrier collection by diffusion is necessary, and may become the limiting factor. This suggests the dominant role of recombination in the CdTe:Sb absorber layer whether in the depletion width, or the neutral bulk beyond the depletion region.

6.2.2 Voc losses

As discussed in Section 6.1.1, an improvement in N_{CV} of all Sb-doped CdTe solar cells does not yield expected improvement in V_{OC} , as given by equation (6-3) below.

$$\Delta V_{OC, N_{CV}} = \frac{kT}{q} \ln \left(\frac{N_{CV}}{N_{CV0}} \right) \quad (6-3)$$

To provide a quantitative account of V_{OC} deficit arising from different loss mechanisms, estimates of theoretical maximum V_{OC} 's of all devices under study were made as a

function of their doping density. Recombination (or reverse saturation) current density (J_0) was first calculated assuming a minority carrier lifetime (τ_n), of 10 ns (which is the ideal value to achieve high efficiency solar cells, [58]) given by equation (6-4). Using this value of J_0 , the maximum possible V_{OC} for the measured current density is calculated using equation (6-5). Accordingly, V_{OC} deficit from insufficient carrier collection losses is calculated as the difference between $V_{OC, Max-1}$ and $V_{OC, Meas.}$, given by equation (6-6).

$$J_0(\tau_n) = qn_i^2 \left(\frac{D_n}{N_a L_n} \right) = \frac{qn_i^2}{N_a} \sqrt{\frac{D_n}{\tau_n}} \quad (6-4)$$

$$V_{OC, Max-1}(\tau = 10ns, J_{SC, Meas}) = \frac{kT}{q} \ln \left[\frac{J_{SC, Meas.}}{J_0(\tau_n=10ns)} \right] \quad (6-5)$$

$$V_{OC, Loss, Recombination} = V_{OC, Meas.} - V_{OC, Max-1} \quad (6-6)$$

Considering that the maximum possible J_{SC} output among the CdTe devices studied in this work was 28 mA/cm², measured on the ‘Undoped’ baseline device, the theoretical maximum V_{OC} for the measured doping density, termed as $V_{OC, Max-2}$, was calculated assuming an ideal carrier collection, i.e., assuming a maximum J_{SC} of 28.3 mA/cm², using equation (6-7). Consequently, the V_{OC} deficit attributed to recombination losses is calculated as the difference between $V_{OC, Max-1}$ (calculated for 10 ns τ_n) [111] [58] and $V_{OC, Max-2}$ as given in equation (6-6).

$$V_{OC, Max-2}(\tau = 10ns, J_{SC, Max}) = \frac{kT}{q} \ln \left[\frac{J_{SC, Max}}{J_0(\tau=10ns)} \right] \quad (6-7)$$

$$V_{OC, Loss, Collection} = V_{OC, Max-2} - V_{OC, Max-1} \quad (6-8)$$

The theoretical maximum V_{OC} 's for all devices under study calculated this way are given in the 3rd column of Table 6-6, along with expected maximum J_{SC} 's and measured N_{CV} 's (the FF values in this table are discussed in the following section). These voltage estimates are also graphically represented for each device in Figure 6-3. From this graph, it is apparent that a significant portion of V_{OC} deficit in the doped devices arises from SRH recombination, while the deficit from non-ideal current collection is insignificant (due to the logarithmic dependence of V_{OC} on J_{SC}). Figure 6-3 also shows a calculated maximum V_{OC} of 1071 mV as an upper limit for a near-ideal device with a doping density of $5 \times 10^{16} \text{ cm}^{-3}$ and a τ_n of 10 ns and a J_{SC} of 28 mA/cm^2 . This shows that directing future efforts to refine polycrystalline CdTe solar cell processing to reach $>5 \times 10^{16} \text{ cm}^{-3}$ carrier densities at $>10 \text{ ns}$ τ_n can help break the 1V barrier of V_{OC} output in this technology (discussed in detail in Chapter 7).

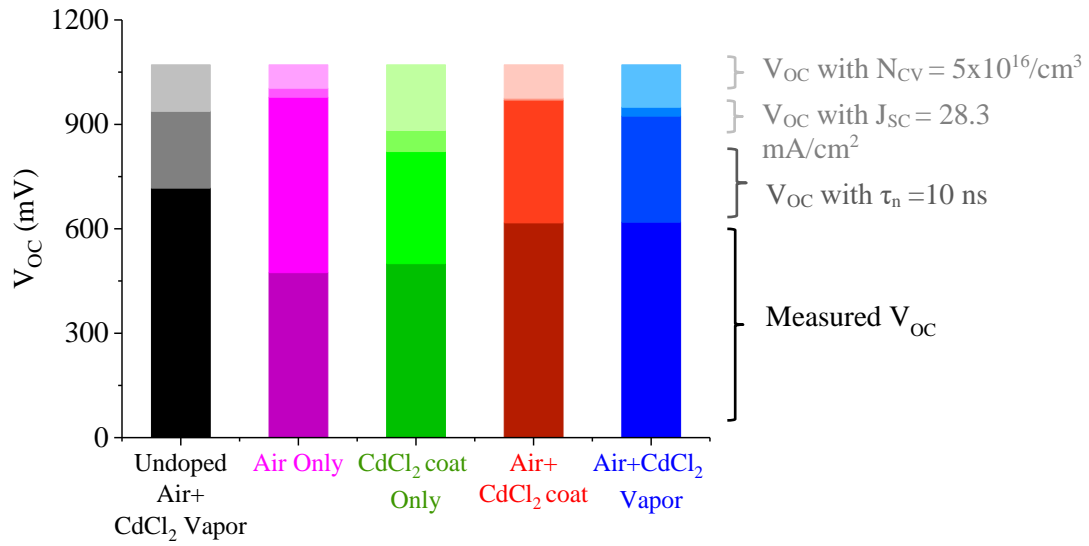


Figure 6-3: Measured V_{OC} 's of devices from anneal matrix, compared with expected V_{OC} 's, calculated using equations (6-8) and (6-6) as a function their measured N_{CV} , for 10 ns τ_n and a maximum J_{SC} of 28 mA/cm². The note on the right is attributing this deficit to recombination in the devices.

6.2.2.1 Voc deficit as a function of defect density

The charge response to capacitance measurements taken at different frequencies and temperatures is different due to the relation between the energy level of responding defects to measurement temperature and frequency, given as follows:

$$E_{\omega} = -kT \ln\left(\frac{\omega}{\omega_0}\right) \quad (6-9)$$

with ω_0 given by,

$$\omega_0 = 2\pi N_V v_{th} \sigma_e \quad (6-10)$$

where N_V is the valence band density of states, v_{th} , the electron thermal velocity, and σ_e , the capture cross section of the defect responding to the ac voltage. From this equation, it is apparent that low frequencies yield response from both shallow and deep defect states within the bandgap while only those defects close to the valence band edge

respond to high frequencies. From equation (6-9) (for a $\sigma_e \approx 1 \times 10^{-14} \text{ cm}^2$ at room temperature), the maximum transition energy of the defects that respond to high frequency (0.5MHz) CV measurement is $\sim 340 \text{ meV} + E_V$, whereas defects with energies up to $520 \text{ meV} + E_V$ can respond to low frequency measurements (1 kHz). Consequently, the N_{CV} taken from CV measurements performed at high frequencies (0.5 MHz) can be attributed to charge response from shallow dopants, whereas low frequency (1 kHz) response can be attributed to all defects below 520 meV in the bandgap. Following common practice, this difference in N_{CV} obtained with low and high frequency measurements, ΔN_{CV} , approximately represents defect density in the CdTe bandgap. Figure 6-4 (a) shows a graph of measured V_{OC} 's plotted as a function of ΔN_{CV} . Except for the device with the lowest N_{CV} ('CdCl₂ only, no air'), (whose doping density is too low for fair comparison with the rest of the devices as its absorber layer is likely fully depleted from charge carriers), the rest of the devices exhibit a trend of decreasing V_{OC} with an increased density of defects in the absorber, represented by ΔN_{CV} , as expected. This graph suggests that the V_{OC} of devices studied in this work is limited by recombination assisted by defects in the absorber bandgap whose density is comparable to the acceptor concentration.

Studies performed on large sample sets of CdTe devices made using different CdTe growth techniques [112] have shown that their TRPL-measured lifetimes (τ_{PL} , which is a close approximation to the minority carrier lifetime in absorber materials of devices) exhibit the following empirical relationship with measured V_{OC} 's:

$$V_{OC} \approx \frac{\ln\{4.6 \times 10^{14} \tau_{PL}(s)\}}{16} \quad (6-11)$$

Expected τ_{PL} of the devices from the anneal matrix extracted using the above relationship are plotted in Figure 6-4 (b) against ΔN_{CV} , which also suggests the inverse

relationship between device quality (represented by expected TRPL lifetime, τ_{PL}) and defect density (represented by ΔN_{CV}), similar to the plot of Figure 6-4 (a). So, while we did not have access to TRPL measurements, the empirically derived results in Figure 6-4 (b) confirms the dependence of V_{OC} on defects or equivalently lifetime. It also confirms that we can use lifetime as a stand-in for defects in modeling in the following section.

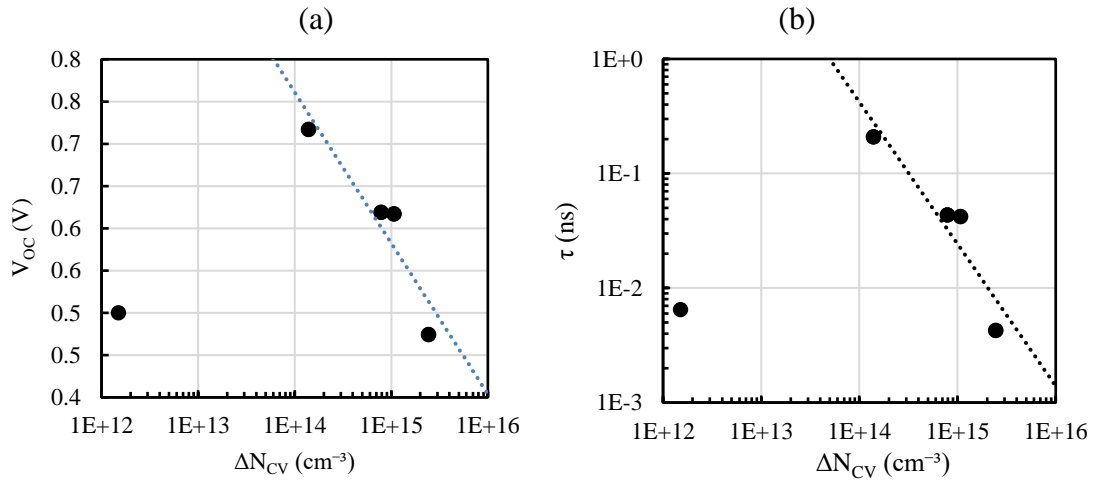


Figure 6-4: Plot showing (a) V_{OC} , and (b) corresponding TRPL lifetime extracted from the empirical relationship given in equation (6-11), as a function of ΔN_{CV} , with the exception of the very-low doping ('CdCl₂ coat only) device on the left whose absorber layer is likely depleted of charge carriers. The remaining devices from the anneal matrix show that their V_{OC} and expected τ_{PL} are limited by defect density, given by ΔN_{CV} .

6.2.3 Blocking contact and its effect on FF deficit

As discussed in Section 5.5.4.2, temperature dependent JV curves taken in the dark can be analyzed to extract the blocking barrier potential in a solar cell. These

contact barrier potentials (Φ_C) extracted for all devices in the study are given in Table 6-4. Activation energies estimated from admittance spectroscopy measurements (discussed in Section 5.5.3) are also given in this table (E_A-E_V) to compare with the JVT-estimated blocking potentials. The large error in the estimated (E_A-E_V) of some of the samples is due to a variability in the slope of the fit at different regions of the fit. This uncertainty is marked here as an error bar in the extracted activation energy. It can be evident from this plot that (E_A-E_V)'s of all devices estimated from admittance measurements match closely with Φ_C 's extracted from *Dark JV(T)* measurements. This similarity indicates that admittance spectroscopy is in-fact measuring the charge response arising from the Schottky barrier at the back contact (as discussed in Section 5.5.4), preventing extraction of defect transition energies that respond to the ac voltage, frequency and temperature in a similar fashion.

Table 6-4: Schottky barrier potentials of the rear CdTe:Sb/C contacts extracted for all the devices in the anneal matrix from *JV(T)-Dark* measurements, compared with the activation energies of charge response extracted from their admittance spectroscopy measurements

Sample Type	Φ_C from JV(T)- Dark (mV)	E_A-E_V (meV) from AS
Undoped (Air+CdCl ₂ Vapor)	352	330
Air Only, No CdCl ₂	515	500
CdCl ₂ coat Only, No Air	490	370±170
Air+CdCl ₂ coat	537	464±20
Air+CdCl ₂ Vapor	480±80	530

Since it is now established that contact potentials of. ~400-500 mV exist in all Sb-doped devices, compared to Φ_C ~350 mV in the control sample, its effect on the performance of these devices is now investigated. It is known that blocking contact

mainly affects device FF but it has no effect on device V_{OC} because no current flows in the device at V_{OC} . This is the same reason why series resistance has no impact on device V_{OC} . The rear barrier is also likely to have negligible effect on J_{SC} since most of the photocarriers are generated at the front of the device in the main junction depletion region and never ‘see’ the reverse barrier at the back. The only way the back barrier could impact V_{OC} or J_{SC} is if carriers were generated in the rear depletion region and it had a photovoltage that opposed that of the main junction. The effect of blocking contact on device FF, however, is well-understood. It is known that the ideal FF is a direct function of device V_{OC} for solar cells, given by equations (6-12) and (6-13), in the absence of any non-idealities in the solar cell (such as those discussed in Section 1.3.1). [113] Thus, the maximum possible FF for any given voltage can be calculated as $FF_0(V_{OC})$ as:

$$FF_0(v'_{OC}) \approx \left(1 - \frac{\ln v'_{OC}}{v'_{OC}}\right) \left(1 - \frac{1}{v'_{OC}}\right) \left(\frac{1}{1 - \exp(-v'_{OC})}\right) \quad (6-12)$$

$$v'_{OC} = \frac{qV_{OC}}{kT} + \ln\left(\frac{qV_{OC}}{kT} + 1\right) \quad (6-13)$$

Using these equations, FF_0 as a function of measured V_{OC} of all devices are calculated using the above equations and given in Table 6-5

Table 6-5: FF limit calculated as a function of V_{OC} , assuming no blocking contact, series or shunt resistances

Sample Type	FF _{Meas.} (%)	FF ₀ ($V_{OC, Meas}$) (%)
Undoped	36.7	86.1
Air Only, No CdCl ₂	19.5	81.6
CdCl ₂ coat Only, No Air	27.9	82.2
Air+CdCl ₂ coat	29.7	84.6
Air+CdCl ₂ Vapor	18.0	84.6

The analysis of FF deficit in the devices under study indicate severe losses arising from the blocking barrier at the back in addition to lumped series and shunt resistances. In most 1-diode devices (with ohmic p- and n- contacts), series and shunt resistances are the dominant cause of FF deficit. Therefore, future efforts should be directed towards making duplicates of extrinsically doped devices with Cu doping or alternative contacts which provide more ideal match to the doped CdTe work function. While the samples without Cu-alloying at the back can be used to estimate N_{CV} using CV measurements (without interference from Cu doping), their duplicates that receive such improved back contacts would allow isolation of the effects of recombination and of blocking barrier in the FF deficit of devices.

6.2.4 Performance estimation of extrinsically doped solar cells

Using the analytical approach discussed in Section 6.2.2, the upper limit for device performance of the best Sb-doped device ('Air+CdCl₂ coat') is estimated. The maximum V_{OC} possible for the carrier density measured on this device ($N_{CV}=1 \times 10^{15} \text{ cm}^{-3}$) is estimated to be 975 mV (using equation (6-5)) if a carrier lifetime of 10 ns is achieved. [111] Furthermore, if a 100% doping efficiency (i.e., $N_{CV}=5 \times 10^{16} \text{ cm}^{-3}$) is realized, V_{OC} of 1071 mV is achievable. Table 6-6 compares the measured JV

parameters of this device with those calculated for the aforementioned ideal conditions, with a maximum J_{SC} assumed to be 28.3 mA/cm^2 (as measured on the baseline ‘undoped’ device) and FF assumed to be 81% (maximum reported FF for devices processed at IEC [114] and close to that of champion cells). Considering that $5 \times 10^{16} \text{ cm}^{-3}$ Sb incorporation in VTD-grown CdTe was successfully demonstrated, bridging this gap in device performance entails further exploration and refinement of empirical process sequences aimed at successful activation of the incorporated Sb species.

Table 6-6: JV parameters of the best Sb-doped device as measured (‘Air+CdCl₂ coat’), compared to hypothetical devices: one with improved $\tau_n = 10 \text{ ns}$, and another with $N_{CV}=[Sb]=5 \times 10^{16} \text{ cm}^{-3}$, to demonstrate the potential of efficiency gain from successful extrinsic doping in CdTe

Sample Type		τ_n (ns)	N_{CV} (cm^{-3})	V_{OC} (mV)	J_{SC} (mA/cm^2)	FF (%)	η_{Max} (%)
Best Sb-doped device	As-measured	<0.01	1.6×10^{15}	617	22.7	29.7	4.2
	With $\tau_n=10\text{ns}$, maximum J_{SC} and FF	10	1.6×10^{15}	975	28.3	81.0	22.3
Device with near-ideal $5 \times 10^{16} \text{ cm}^{-3} N_{CV}$	With $\tau_n=10\text{ns}$, maximum J_{SC} and FF	10	5.0×10^{16}	1071	28.3	81.0	24.6

6.3 Best Sb-Doped Device Processed at IEC

While this dissertation primarily focused on separating the effects of different known CdTe film treatments, subsequent devices processed following further optimization of other process sequences were not discussed within the scope of this work. CdTe:Sb films processed in subsequent VTD depositions have yielded $>9 \times 10^{16}$

cm⁻³ Sb incorporation levels. The best-recorded efficiency for Sb-doping was achieved on a device processed on this film, that yielded a doping density of 3x10¹⁵ cm⁻³ (equivalent to a doping efficiency of 3.3%), a V_{OC} of ~760 mV—exceeding the V_{OC}'s of all devices studied in this work, doped and undoped—with an efficiency of 6.4%. The JV and CV data of this device is provided in Figure 6-5 below. This device is seen to also be limited by a blocking barrier (from the characteristic ‘S-shape’ in its J-V curve), as is expected for diagnostic device structures. The results for this device show promise for extrinsic doping of CdTe with Sb, demonstrating an ~10x enhancement in doping density compared to state-of-the-art CdTe devices, yielding V_{OC} >750 mV.

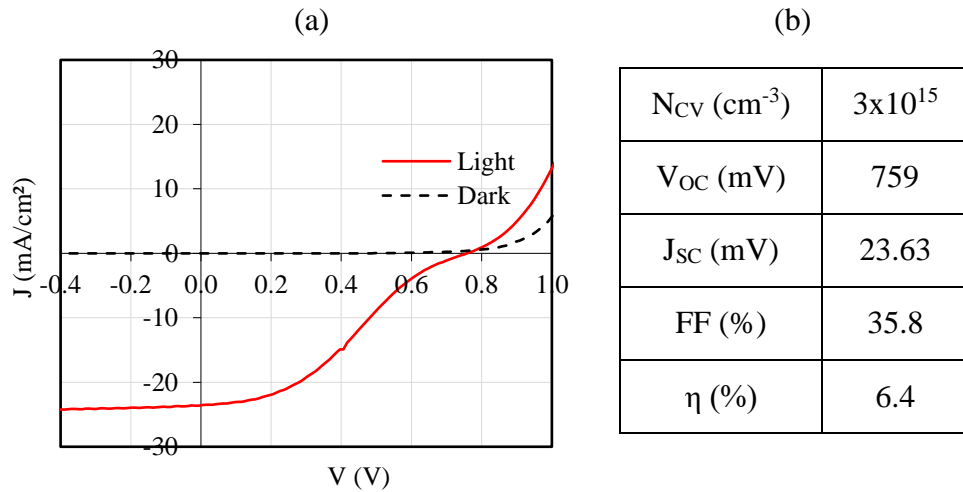


Figure 6-5: (a) JV curve of the best Sb-doped device processed at IEC and its (b) tabulated device parameters

6.4 Discussion and Summary

In this chapter, established CdTe device anneal treatments were applied to Sb-doped devices. Sb doping has shown promise of improved acceptor density over intrinsically doped CdTe by more than an order of magnitude ($>13x$). Successful demonstration of V_{OC} enhancement with extrinsic doping CdTe solar cells will benefit from studying device processing techniques to enable control over all the properties which affect device performance. Different post-processing techniques evaluated in this study to separate effects of ambient and chemical agent (Section 6.1) show that devices annealed in a combination of air and $CdCl_2$ show best performance. While Sb doping has shown significant promise in increasing the carrier concentration, this does not, however, translate to improved photovoltage. Photovoltages $> 1V$ and device efficiencies of $>22\%$ are possible with the Sb-doped devices studied here if all these non-idealities are effectively mitigated. More specifically, it is the low ‘doping efficiency’, in which un-activated Sb affects transport and recombination, that limits device V_{OC} , while a large blocking barrier (at the p-type contact) affects the FF. Considering Sb incorporation of $\sim 5 \times 10^{16} \text{ cm}^{-3}$ demonstrated in the CdTe:Sb film and measured doping densities of $\sim 3 \times 10^{15} \text{ cm}^{-3}$ in the devices processed from these films, the doping efficiency is $<10\%$ (in comparison to nearly 100% doping efficiency of the semiconductors used in other solar cell technologies, such as c-Si) but still significantly higher than has been achieved in 2 decades of intensive effort to increase the acceptor density using Cu and Cl. This means that $>5 \times 10^{16} \text{ cm}^{-3}$ Sb atoms are present in the CdTe:Sb lattice, occupying defect states of unknown properties, leading to severe recombination. Consequently, further improvement of the various process sequences—from absorber deposition to contact preparation—aimed at enhancing doping efficiency to $\sim 100\%$ is key to realize the potential of Sb-doped CdTe solar cells. A more targeted

approach to mitigating these defects would require further investigation into the nature of these defects and their properties—such as transition energy level, concentration, capture cross section, etc.

The results from JV and capacitance measurements emphasize the need for a combination of high drift field in the depletion region enabled by high dopant density, along with sufficient carrier lifetime enabled by minimizing defect concentration from Sb incorporation is essential to extract the potential high performance in these devices. The answer to both these challenges lies in successful activation of incorporated Sb atoms in CdTe or to aim for near 100% ‘doping efficiency’.

CONCLUSION AND FUTURE WORK

7.1 Decoupled PV-EC Architecture for Efficiency and Practicality

7.1.1 Conclusion of experimental and simulation results

This dissertation focused on employing decoupled PV-EC architecture to achieve efficient, yet practical devices. A generalized model was developed using ‘load-matching’ to optimize the efficiency of PV-EC’s using the current-voltage characteristics of the solar cell and electrochemical device as input. Experimental implementation of a CO₂ PV-EC using the highest efficiency commercially-available c-Si solar cells with an independently optimized CO₂ electrolyzer (designed and processed by Dr. Jiao’s group at UD [63]) yielded a solar-to-fuel efficiency of 6.5%, that matched very closely with the efficiency predicted from the model after accounting for known parasitic losses. These modeling and experimental results were published as the largest-area CO₂ solar fuel device to be reported. [59], [60]

The model was extended to calculate gas output for any PV-EC of known electrical and electrochemical characteristics (of the PV source and electrochemical load, respectively), and for any given location (with the corresponding weather data, hourly insolation and temperature for a model year). This extended model was applied to the experimentally-demonstrated CO₂ PV-EC and a conceptually designed MW-scale H₂O electrolyzer. The latter PV-EC system was designed using all-back-contact c-Si solar modules (~435 W_p each) from SunPower® and a 2.1 MW H₂O electrolyzer from ProtonOnsite®. The annual generation model was used also to evaluate the advantage of employing power conditioning devices with decoupled PV-ECs. Annual gas yield from CO₂ and H₂O PV-ECs were calculated using hourly irradiance and temperature

data for Wilmington, DE, USA and compared with and without power electronic devices to maintain MPPT during operation. It was demonstrated that power-conditioning devices employing MPPT can improve annual gas output by >20% for sub-optimally matched systems. Besides improved performance, power conditioning devices offer several other practical advantages, the most critical one being that they remove the constraint of needing to match the power of the PV array to the electrolyzer which in any case only can occur at a single irradiance and temperature. Additionally, MPPT power matching devices help to maintain a constant input voltage to the EC which helps to control the product gas ratio and alleviates degradation-related or weather-related challenges in power matching, offering an effective storage mechanism for grid-level systems, preventing curtailment of PV or wind-generated electricity.

7.1.2 Future work

The load matching model proposed in Chapter 2 of this work discusses successful implementation and experimental results with commercially available solar cells. However, when used with high efficiency multijunction solar cells under concentration, this model has demonstrated increased potential for enhanced SFE potential of up to 14%, at high current densities of $>1 \text{ A/cm}^2$, compared to the current SFE record of 10% for CO_2 devices. [5]

The annual generation model developed in this work calculates annual performance of PV-EC systems irrespective of their scale. This model can be further improved to incorporate a cost component, enabling a more complete comparison and assessment for planning and commissioning real solar fuel projects.

7.2 Sb-doped CdTe Photovoltaics for Increased Voltage Output

7.2.1 Summary of results from device analysis

This work focused on applying extrinsic doping as a means to realize the V_{oc} potential in thin film CdTe technology. Substitutional p-type doping of Te in the CdTe lattice using Sb was studied. Specifically, different electrical characterization techniques were applied on the diagnostic devices made on Sb-doped CdTe films and its results were analyzed to understand loss mechanisms. Enhancement in thin-film CdTe carrier concentration by over an order of magnitude—from 1×10^{14} to $>5 \times 10^{15}$ cm^{-3} —was demonstrated using substitutional doping with Sb, using an industry-standard vapor transport deposition technique. It was shown that a high temperature (400-500°C) anneal of CdTe:Sb films in excess Cd vapor pressure was essential to ‘activate’ the incorporated Sb in the CdTe lattice and contribute to acceptor doping. Devices made on Cd-vapor-treated CdTe:Sb films show an improvement in carrier concentration by over 2 orders of magnitude. Established post-processing treatments used for state-of-the-art CdTe solar cells were applied to these Sb-doped devices and effects on device performance was compared. Initial JV and CV measurements of these devices suggest that similar to intrinsically doped CdTe solar cells, Sb-doped devices benefit from anneal treatments at $\sim 400^\circ\text{C}$ in an ambient providing both O_2 and CdCl_2 to the exposed CdTe:Sb surface, which improved carrier concentration, and overall device efficiency.

While Sb-doping improved doping density and yielded functioning solar cells, their performance, however, was inferior to baseline ‘undoped’ devices. A combination of different device measurement and analysis techniques was applied to understand the loss mechanisms of CdTe:Sb devices. Complementary techniques confirmed that non-

radiative recombination from defect density comparable to that of doping leads to significant losses in device V_{OC} and J_{SC} , while a blocking p-type contact at the CdTe/C interface with barrier potential of ~ 500 mV severely affects the FF. Mitigating the blocking contact and minimizing defect formation by effectively activating 100% incorporated Sb atoms as acceptor dopants reduces non-radiative recombination will push efficiency to $>25\%$ when 100% doping efficiency with $5 \times 10^{16} \text{ cm}^{-3}$ doping density is realized.

7.2.2 Future work

Dopant incorporation $>5 \times 10^{16} \text{ cm}^{-3}$ (Section of Chapter 5, Figure 5-4) was demonstrated in CdTe:Sb films grown using the vapor transport deposition technique, but the measured acceptor densities, N_{CV} , on devices processed from these films remained $<5 \times 10^{15} \text{ cm}^{-3}$ activated dopant density. This is suggestive of $>5 \times 10^{15} \text{ cm}^{-3}$ Sb atoms in the CdTe lattice present as un-activated dopant species. Specific information regarding the exact nature of these un-activated Sb atoms is not known or understood, particularly pertaining to (as demonstrated in Figure 7-1) (i) their occupation in the lattice—as interstitials, anti-sites, segregation at grain boundaries, interfaces, or other lattice sites, (ii) the spatial, or energy profiles of the corresponding defects they contribute in the bandgap (defect density as a function of depth (x), position (y,z) and energy relative to valence band edge, respectively), capture cross section, occupancy etc. (iii) a quantitative account of their contribution to non-radiative recombination, and to the losses in specific device parameters and (iv) how this information can be used to tune and improve empirical processes to ultimately enhance doping efficiency. To that end, future efforts should be focused on applying more device and materials characterization tools, such as secondary-ion mass spectroscopy (SIMS),

x-ray photoelectron spectroscopy (XPS), deep level transient spectroscopy (DLTS), time-resolved photoluminescence (TRPL), and cathodoluminescence (CL) in parallel with simulation studies using density function theory (DFT) and device modeling to extract information regarding the defect chemistry.

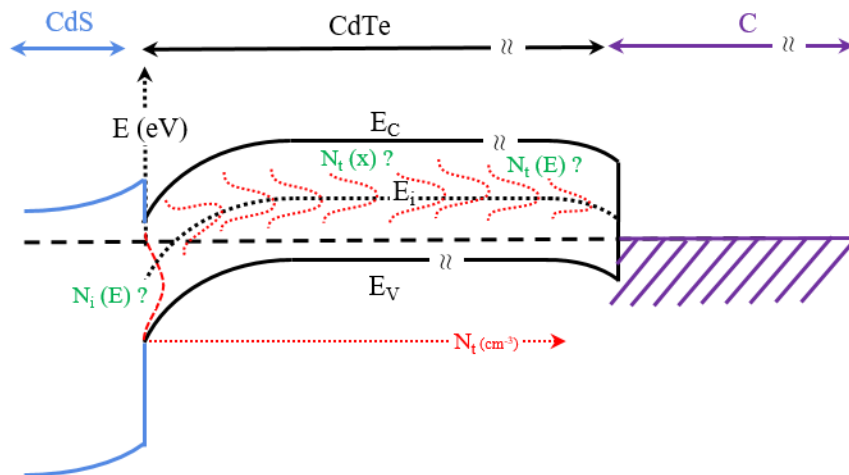


Figure 7-1: Band diagram of CdTe:Sb devices illustrating the unknown nature of defects contributing to deficit in performance.

Another key conclusion of this work was that the presence of a large blocking contact barrier prevents efficient extraction of photocurrent and contributes to significant FF losses. Consequently, further exploration of empirical processes in the future can benefit from processing replicates of all doped devices, with one receiving an undoped, carbon contact as the anode that can enable effective carrier density extraction from CV measurement, while duplicate pieces receive Cu-doped back contacts that can be used for better JV measurement. This prevents the interference of blocking contacts for accurate measurement of device performance. An effective optimization of process sequences for extrinsically doped CdTe devices with Sb and other group V dopants such as P and As, [58] supported by accurate extraction of information regarding defect chemistry using appropriate material and device characterization techniques can facilitate the realization of >25% photo-conversion efficiencies, enabled by $>5 \times 10^{16} \text{ cm}^{-3}$ carrier concentrations.

REFERENCES

- [1] "Dept. of Energy's Federal Energy management program", [Online]. Available: <https://www.energy.gov/eere/femp/federal-agency-use-renewable-electric-energy>. [Accessed Nov. 16, 2018].
- [2] T. J. Jacobsson *et al*, "Sustainable solar hydrogen production: from photoelectrochemical cells to PV-electrolyzers and back again," *Energy & Environmental Science*, vol. 7, (7), pp. 2056-2070, 2014.
- [3] J. Jia *et al*, "Solar water splitting by photovoltaic-electrolysis with a solar-to-hydrogen efficiency over 30%," *Nature Communications*, vol. 7, pp. 13237, 2016.
- [4] C. R. Cox *et al*, "Ten-percent solar-to-fuel conversion with nonprecious materials," *Proceedings of the National Academy of Sciences*, vol. 111, (39), pp. 14057-14061, 2014.
- [5] X. Zhou *et al*, "Solar-driven reduction of 1 atm of CO₂ to formate at 10% energy-conversion efficiency by use of a TiO₂-protected III–V tandem photoanode in conjunction with a bipolar membrane and a Pd/C cathode," *ACS Energy Letters*, vol. 1, (4), pp. 764-770, 2016.
- [6] Deguchi Masahiro, Yotsuhashi satoshi and Yamada yuka, "Method for reducing carbon dioxide," US 8,414,758 B2, Apr 9, 2013.
- [7] H. H. Storch, N. Golumbic and R. A. Anderson, *The Fischer-Tropsch and Related Syntheses*. 1951, 6.
- [8] A. Fujishima and K. Honda, "Electrochemical photolysis of water at a semiconductor electrode," *Nature*, vol. 238, (5358), pp. 37, 1972.
- [9] O. Khaselev and J. A. Turner, "A monolithic photovoltaic-photoelectrochemical device for hydrogen production via water splitting," *Science*, vol. 280, (5362), pp. 425-427, 1998.
- [10] J. Jia *et al*, "Solar water splitting by photovoltaic-electrolysis with a solar-to-hydrogen efficiency over 30%," *Nature Communications*, vol. 7, pp. 13237, 2016.

-
- [11] W. M. Ayers, "Carbon Dioxide Chemistry: Environmental Issues," *Royal Society Chemistry*, vol. 153, pp. 365-374, 1994.
- [12] E. E. Benson *et al*, "Electrocatalytic and homogeneous approaches to conversion of CO₂ to liquid fuels," *Chem. Soc. Rev.*, vol. 38, (1), pp. 89-99, 2009.
- [13] J. Marshall, "Springtime for the artificial leaf," *Nature*, vol. 510, (7503), pp. 22, 2014.
- [14] Hemminger, J. C., R. Carr, and G. A. Somorjai. "The photoassisted reaction of gaseous water and carbon dioxide adsorbed on the SrTiO₃ (111) crystal face to form methane." *Chemical Physics Letters* 57, no. 1 (1978): 100-104.
- [15] M. Halmann, "Photoelectrochemical reduction of aqueous carbon dioxide on p-type gallium phosphide in liquid junction solar cells," *Nature*, vol. 275, (5676), pp. 115, 1978.
- [16] M. Schreier *et al*, "Efficient photosynthesis of carbon monoxide from CO₂ using perovskite photovoltaics," *Nature Communications*, vol. 6, pp. 7326, 2015.
- [17] X. Zhou *et al*, "Solar-driven reduction of 1 atm of CO₂ to formate at 10% energy-conversion efficiency by use of a TiO₂-protected III-V tandem photoanode in conjunction with a bipolar membrane and a Pd/C cathode," *ACS Energy Letters*, vol. 1, (4), pp. 764-770, 2016.
- [18] J. Rongé *et al*, "Monolithic cells for solar fuels," *Chem. Soc. Rev.*, vol. 43, (23), pp. 7963-7981, 2014.
- [19] B. McCandless, "Cadmium telluride solar cells," in *Handbook of Photovoltaic Science and Engineering*, A. H. Luque Steven, Ed. John Wiley & Sons, 2003.
- [20] J. J. Loferski, "Theoretical considerations governing the choice of the optimum semiconductor for photovoltaic solar energy conversion," *J. Appl. Phys.*, vol. 27, (7), pp. 777-784, 1956.
- [21] P. Rappaport, "The photovoltaic effect and its utilization," *Solar Energy*, vol. 3, (4), pp. 8-18, 1959.
- [22] J. Mimila-Arroyo *et al*, "Electric and photovoltaic properties of CdTe pn homojunctions," *Solar Energy Materials*, vol. 1, (1-2), pp. 171-180, 1979.
- [23] G. Cohen-Solal, D. Lincot and M. Barbe, "High efficiency shallow p nn cadmium telluride solar cells," in *Fourth EC Photovoltaic Solar Energy Conference*, 1982, pp. 621-626.

-
- [24] J. P. Ponpon and P. Siffert, "Barrier heights on cadmium telluride schottky solar cells," *Revue De Physique Appliquée*, vol. 12, (2), pp. 427-430, 1977.
- [25] R. S. Muller and R. Zuleeg, "Vapor-Deposited, Thin-Film Heterojunction Diodes," *J. Appl. Phys.*, vol. 35, (5), pp. 1550-1556, 1964.
- [26] K. W. Mitchell, A. L. Fahrenbruch and R. H. Bube, "Evaluation of the CdS/CdTe heterojunction solar cell," *J. Appl. Phys.*, vol. 48, (10), pp. 4365-4371, 1977.
- [27] K. Yamaguchi *et al*, "CdS–CdTe solar cell prepared by vapor phase epitaxy," *Japanese Journal of Applied Physics*, vol. 16, (7), pp. 1203, 1977.
- [28] E. I. Adirovich, Y. M. Yuabov and G. R. Yagudaev, "Photoelectric effects in film diodes with CdS-CdTe heterojunctions," *Sov Phys Semiconductors*, vol. 3, (1), pp. 61-64, 1969.
- [29] X. Wu, "High-efficiency polycrystalline CdTe thin-film solar cells," *Solar Energy*, vol. 77, (6), pp. 803-814, 2004.
- [30] (Feb 23,). *First Solar Achieves Yet Another Cell Conversion Efficiency World Record*.
Available: <https://www.businesswire.com/news/home/20160223005315/en/>.
- [31] NREL Technical Staff, "Cadmium Use in Photovoltaics" *nrel.gov*, [Online] Available: www.nrel.gov/cdte/perspective.html. [Accessed July 10, 2018]
- [32] J. Siemer, "The situation for PV funds is complicated, but the great potential remains" *Photon International*, pp. 32-37, Sep 9. 2005.
- [33] M. A. Green, "Thin-film solar cells: review of materials, technologies and commercial status," *J Mater Sci: Mater Electron*, vol. 18, (1), pp. 15-19, 2007.
- [34] V. M. Fthenakis, "Life cycle impact analysis of cadmium in CdTe PV production," *Renewable and Sustainable Energy Reviews*, vol. 8, (4), pp. 303-334, 2004.
- [35] A.L. Fahrenbruch, "Ohmic contacts and doping of CdTe." *Solar Cells*, vol. 21 (1), pp. 399-412, 1987.
- [36] A. Niemegeers and M. Burgelman, "Effects of the Au/CdTe back contact on IV and CV characteristics of Au/CdTe/CdS/TCO solar cells," *J. Appl. Phys.*, vol. 81, (6), pp. 2881-2886, 1997.

-
- [37] J. Britt and C. Ferekides, "Thin-film CdS/CdTe solar cell with 15.8% efficiency," *Appl. Phys. Lett.*, vol. 62, (22), pp. 2851-2852, 1993.
- [38] H. Ohyama *et al*, "16.0% efficient thin-film CdS/CdTe solar cells," in *Photovoltaic Specialists Conference, 1997., Conference Record of the Twenty-Sixth IEEE*, 1997.
- [39] M. A. Green *et al*, "Solar cell efficiency tables (version 18)," *Prog. Photovolt: Res. Appl.*, vol. 9, (4), pp. 287-293, 2001.
- [40] X. Wu *et al*, "16.5%-efficient CdS/CdTe polycrystalline thin-film solar cell," in *Proceedings of the 17th European Photovoltaic Solar Energy Conference*, 2001.
- [41] M. A. Green *et al*, "Solar cell efficiency tables (version 37)," *Prog. Photovolt: Res. Appl.*, vol. 19, (1), pp. 84-92, 2011.
- [42] M. A. Green *et al*, "Solar cell efficiency tables (version 48)," *Prog. Photovolt: Res. Appl.*, vol. 24, (7), pp. 905-913, 2016.
- [43] E. Wesoff, "Exclusive: First Solar's CTO Discusses Record 18.6% Efficient Thin-Film Module," Green Tech Media, 15 June 2015. [Online]. Available: <http://www.greentechmedia.com/articles/read/Exclusive-First-Solar's-CTO-Discusses-Record-18.6-Efficient-Thin-Film-Mod>. [Accessed 15 September 2015].
- [44] A. Kanevce and T. A. Gessert, "Optimizing CdTe solar cell performance: Impact of variations in minority-carrier lifetime and carrier density profile," *IEEE Journal of Photovoltaics*, vol. 1, (1), pp. 99-103, 2011.
- [45] C. Walkons, "Approaches to Improve the Voc of CdTe Devices: Device Modeling and Thinner Devices, Alternative Back Contacts.", University of Delaware, 2016.
- [46] First Solar Technical Staff, "First Solar builds the highest efficiency thin film PV cell on record." August 1, 2014, [Online] Available: <http://investor.firstsolar.com/releases>. [Accessed August 8, 2015].
- [47] R. A. Sinton and A. Cuevas, "Contactless determination of current-voltage characteristics and minority-carrier lifetimes in semiconductors from quasi-steady-state photoconductance data," *Appl. Phys. Lett.*, vol. 69, (17), pp. 2510-2512, 1996.

-
- [48] A. Rockett, S. Marsillac and R. Collins, "Novel contact materials for improved performance CdTe solar cells final report," Colorado School of Mines, Golden, CO (United States), 2018.
- [49] C. Walkons *et al*, "CdTe solar cells with a PCBM back contact," in *2014 IEEE 40th Photovoltaic Specialist Conference (PVSC)*, 2014.
- [50] M. Tuteja *et al*, "Direct observation of CdCl₂ treatment induced grain boundary carrier depletion in CdTe solar cells using scanning probe microwave reflectivity based capacitance measurements," *The Journal of Physical Chemistry C*, vol. 120, (13), pp. 7020-7024, 2016.
- [51] M. Tuteja *et al*, "Direct observation of electrical properties of grain boundaries in sputter-deposited CdTe using scan-probe microwave reflectivity based capacitance measurements," *Appl. Phys. Lett.*, vol. 107, (14), pp. 142106, 2015.
- [52] K. Zanio, "Chapter 3," in *Semiconductors and Semimetals*, R. K. Willardson and A. C. Beer, Eds. New York: Academic Press, 1978.
- [53] F. A. Kröger, "The defect structure of CdTe," *Revue De Physique Appliquée*, vol. 12, (2), pp. 205-210, 1977.
- [54] A. J. Strauss, "The physical properties of cadmium telluride," *Revue De Physique Appliquée*, vol. 12, (2), pp. 167-184, 1977.
- [55] J. Gu *et al*, "Ohmic contact and impurity conduction in P- doped CdTe," *J. Appl. Phys.*, vol. 46, (3), pp. 1184-1185, 1975.
- [56] S. Wei and S. B. Zhang, "First-principles study of doping limits of CdTe," *Physica Status Solidi (B)*, vol. 229, (1), pp. 305-310, 2002.
- [57] J. M. Burst *et al*, "CdTe solar cells with open-circuit voltage breaking the 1 V barrier," *Nature Energy*, vol. 1, (3), pp. 16015, 2016.
- [58] B. E. McCandless *et al*, "Overcoming Carrier Concentration Limits in Polycrystalline CdTe Thin Films with In Situ Doping," *Scientific Reports*, vol. 8, (1), pp. 14519, 2018.
- [59] G. M. Sriramagiri *et al*, "Design and Implementation of High Voltage Photovoltaic Electrolysis System for Solar Fuel Production from CO₂," *MRS Advances*, vol. 2, (55), pp. 3359-3364, 2017.

-
- [60] G. M. Sriramagiri *et al*, "Toward a Practical Solar-Driven CO₂ Flow Cell Electrolyzer: Design and Optimization," *ACS Sustainable Chem. Eng.*, vol. 5, (11), pp. 10959-10966, 2017.
- [61] G. Sriramagiri *et al*, "Computation and assessment of solar electrolyzer field performance: comparing coupling strategies," *Sustainable Energy Fuels*, 2019. Available: <http://dx.doi.org/10.1039/C8SE00399H>.
- [62] Ahmed, N., Zhang, L., Sriramagiri, G., Das, U., & Hegedus, S. "Electroluminescence analysis for spatial characterization of parasitic optical losses in silicon heterojunction solar cells". *Journal of Applied Physics*, 123(14), 143103.
- [63] W. Luc, J. Rosen and F. Jiao, "An Ir-based anode for a practical CO₂ electrolyzer," *Catalysis Today*, vol. 288, pp. 79-84, 2017.
- [64] Q. Lu *et al*, "A selective and efficient electrocatalyst for carbon dioxide reduction," *Nature Communications*, vol. 5, pp. 3242, 2014.
- [65] Q. Lu, J. Rosen and F. Jiao, "Nanostructured Metallic Electrocatalysts for Carbon Dioxide Reduction," *ChemCatChem*, vol. 7, (1), pp. 38-47, 2015.
- [66] V. Sabnis, H. Yuen and M. Wiemer, "High-efficiency multijunction solar cells employing dilute nitrides," *AIP Conference Proceedings*, vol. 1477, (1), pp. 14-19, 2012.
- [67] J. Bullock *et al*, "Efficient solar-driven electrochemical CO₂ reduction to hydrocarbons and oxygenates," *Energy & Environmental Science*, vol. 10, (10), pp. 2222-2230, 2017.
- [68] S. Haussener *et al*, "Simulations of the irradiation and temperature dependence of the efficiency of tandem photoelectrochemical water-splitting systems," *Energy & Environmental Science*, vol. 6, (12), pp. 3605-3618, 2013.
- [69] M. T. Winkler *et al*, "Modeling integrated photovoltaic–electrochemical devices using steady-state equivalent circuits," *Proc. Natl. Acad. Sci. USA*, 2013.
- [70] A. Mohammadi and M. Mehrpooya, "A comprehensive review on coupling different types of electrolyzer to renewable energy sources," *Energy*, vol. 158, pp. 632-655, 2018.

-
- [71] T. Eswam and P. L. Chapman, "Comparison of Photovoltaic Array Maximum Power Point Tracking Techniques," *IEEE Transactions on Energy Conversion*, vol. 22, (2), pp. 439-449, 2007.
- [72] H. Masheleni and X. F. Carelse, "Microcontroller-based charge controller for stand-alone photovoltaic systems," *Solar Energy*, vol. 61, (4), pp. 225-230, 1997.
- [73] R. R. Gutierrez and S. Haussener, "Modeling of Concurrent CO₂ and Water Splitting by Practical Photoelectrochemical Devices," *J. Electrochem. Soc.*, vol. 163, (10), pp. H1018, 2016.
- [74] M. R. Shaner *et al*, "A comparative technoeconomic analysis of renewable hydrogen production using solar energy," *Energy & Environmental Science*, vol. 9, (7), pp. 2354-2371, 2016.
- [75] R. R. Gutierrez and S. Haussener, "Modeling of Concurrent CO₂ and Water Splitting by Practical Photoelectrochemical Devices," *J. Electrochem. Soc.*, vol. 163, (10), pp. H1018, 2016.
- [76] NREL Technical Staff, "NREL's National Solar Radiation Database (NSRDB)" [Online]. Available: <https://nsrdb.nrel.gov/nsrdb-viewer> [Accessed July 17, 2018].
- [77] Hegedus SS, Shafarman WN. Thin-film solar cells: device measurements and analysis. *Prog Photovoltaics Res Appl* 2004;12(2-3):155-176.
- [78] B. K. Bose, "Power Electronics and Motor Drives Recent Progress and Perspective," *IEEE Transactions on Industrial Electronics*, vol. 56, (2), pp. 581-588, 2009. . DOI: 10.1109/TIE.2008.2002726.
- [79] ProtonOnsite[®] Technical Staff, "Proton OnSite[®]'s M Series Hydrogen Generation Systems Specification Sheet" [Online]. Available: http://www.protononsite.com/sites/default/files/2018-04/PD-0600-0119_rev_a.pdf [accessed July 17, 2018].
- [80] SunPower[®] Technical Staff, "SunPower[®]'s E-series module data sheet" [Online]. Available: <https://us.sunpower.com/sites/sunpower/files/media-library/data-sheets/ds-e20-series-435-commercial-solar-panels.pdf> [Accessed July 17th, 2018].
- [81] R. A. Messenger and J. Ventre, "Grid-connected utility-interactive PV systems," in *Photovoltaic Systems Engineering* Anonymous CRC press, pp. 106-137.

-
- [82] B. E. McCandless and W. N. Shafarman, "Chemical Surface Deposition of Ultra-Thin Semiconductors," U.S. Patent 6,537,845, 25 Mar., 2003.
- [83] B. E. McCandless and W. A. Buchanan, "High throughput processing of CdTe/CdS solar cells with thin absorber layers," in *2008 33rd IEEE Photovoltaic Specialists Conference*, 2008.
- [84] N. Romeo *et al*, "Growth of polycrystalline CdS and CdTe thin layers for high efficiency thin film solar cells," *Materials Chemistry and Physics*, vol. 66, (2), pp. 201-206, 2000.
- [85] W. K. Metzger *et al*, "CdCl₂ treatment, S diffusion, and recombination in polycrystalline CdTe," *J. Appl. Phys.*, vol. 99, (10), pp. 103703, 2006.
- [86] G. M. Hanket *et al*, "Design of a vapor transport deposition process for thin film materials," *Journal of Vacuum Science & Technology A*, vol. 24, (5), pp. 1695-1701, 2006.
- [87] J. M. Burst *et al*, "Carrier density and lifetime for different dopants in single-crystal and polycrystalline CdTe," *APL Materials*, vol. 4, (11), pp. 116102, 2016.
- [88] S. Farrell *et al*, "In Situ Arsenic Doping of CdTe/Si by Molecular Beam Epitaxy," *J Electron Mater*, vol. 44, (9), pp. 3202-3206, 2015.
- [89] E Colegrove *et. al*, "Experimental and theoretical comparison of Sb, As, and P diffusion mechanisms and doping in CdTe," *J. Phys. D*, vol. 51, (7), pp. 075102, 2018.
- [90] B. E. McCandless, M. G. Engelmann and R. W. Birkmire, "Interdiffusion of CdS/CdTe thin films: Modeling x-ray diffraction line profiles," *J. Appl. Phys.*, vol. 89, (2), pp. 988-994, 2001.
- [91] E Janik and, R. Triboulet, "Ohmic contacts to p-type cadmium telluride and cadmium mercury telluride," *J. Phys. D*, vol. 16, (12), pp. 2333, 1983.
- [92] R. K. Swank, "Surface Properties of II-VI Compounds," *Phys. Rev.*, vol. 153, (3), pp. 844-849, 1967.
- [93] S. M. Sze and K. N. Kwok, "Measured barrier heights," in *Physics of Semiconductor Devices* Anonymous 2007, pp. 179.

-
- [94] S. S. Hegedus and B. E. McCandless, "CdTe contacts for CdTe/CdS solar cells: effect of Cu thickness, surface preparation and recontacting on device performance and stability," *Solar Energy Materials and Solar Cells*, vol. 88, (1), pp. 75-95, 2005.
- [95] HP Technical Staff, "Section 3-33," in *Operating Manual for HP 4274A Precision LCR Meter* Anonymous HP, 1979, pp. 3.27.
- [96] J. V. Li *et al*, "Theoretical analysis of effects of deep level, back contact, and absorber thickness on capacitance–voltage profiling of CdTe thin-film solar cells," *Solar Energy Materials and Solar Cells*, vol. 100, pp. 126-131, 2012.
- [97] T. Walter *et al*, "Determination of defect distributions from admittance measurements and application to Cu(In,Ga)Se₂ based heterojunctions," *J. Appl. Phys.*, vol. 80, (8), pp. 4411-4420, 1996.
- [98] O. Gunawan *et al*, "Electronic properties of the Cu₂ZnSn (Se, S) 4 absorber layer in solar cells as revealed by admittance spectroscopy and related methods," *Appl. Phys. Lett.*, vol. 100, (25), pp. 253905, 2012.
- [99] T. Kirchartz, K. Ding and U. Rau, "Chapter 2," in *Advanced Characterization Techniques for Thin Film Solar Cells*, D. Abou-Ras, T. Kirchartz and U. Rau, Eds. Wiley-VCH, 2011, pp. 44-46.
- [100] B. E. McCandless, J. E. Phillips and J. Titus, "Characterizing contacts to p-type CdTe in CdS/CdTe solar cells," in *Proc. 2nd World Conf. on PV Solar Energy*, 1998.
- [101] M. Roy, S. Damaskinos and J. E. Phillips, "The diode current mechanism in CuInSe/sub 2/(CdZn)S heterojunctions," in *Conference Record of the Twentieth IEEE Photovoltaic Specialists Conference*, 1988.
- [102] B. Ali *et al*, "Analysis of voltage and temperature dependent photocurrent collection in p3ht/pcbm solar cells," *J. Appl. Phys.*, vol. 112, (11), pp. 114514, 2012.
- [103] S. Hegedus, D. Desai and C. Thompson, "Voltage dependent photocurrent collection in CdTe/CdS solar cells," *Prog. Photovolt: Res. Appl.*, vol. 15, (7), pp. 587-602, 2007.
- [104] R. Muller and T. Kamins, "Schottky barrier, equation 3.3.16," in *Device Electronics for Integrated Circuits*, R. Muller and T. Kamins, Eds. Wiley Publications, 2003, pp. 155.

-
- [105] F. Urbach, "The long-wavelength edge of photographic sensitivity and of the electronic absorption of solids," *Physical Review*, vol. 92, (5), pp. 1324, 1953.
- [106] A. Iribarren *et al*, "Optical and structural evidence of the grain-boundary influence on the disorder of polycrystalline CdTe films," *Appl. Phys. Lett.*, vol. 74, (20), pp. 2957-2959, 1999.
- [107] C. J. Hages, N. J. Carter and R. Agrawal, "Generalized quantum efficiency analysis for non-ideal solar cells: Case of $\text{Cu}_2\text{ZnSnSe}_4$," *J. Appl. Phys.*, vol. 119, (1), pp. 014505, 2016.
- [108] T. Kirchartz, K. Ding and U. Rau, "Fundamental electrical characterization of thin-film solar cells," in *Advanced Characterization Techniques for Thin Film Solar Cells*, D. Abou-Ras and U. Rau, Eds. Wiley, 2011, pp. 37-39.
- [109] A. L. Fahrenbruch and R. H. Bube, "Section 4.5.1," in *Fundamentals of Solar Cells* Anonymous New York: Academic Press, Inc., 1983, pp. 83.
- [110] A. L. Fahrenbruch and R. H. Bube, "Section 4.5.1," in *Fundamentals of Solar Cells* Anonymous New York: Academic Press, Inc., 1983, pp. 84.
- [111] J. N. Duenow *et al*, "Relationship of Open-Circuit Voltage to CdTe Hole Concentration and Lifetime," *IEEE Journal of Photovoltaics*, vol. 6, (6), pp. 1641-1644, 2016.
- [112] W. K. Metzger *et al*, "Time-resolved photoluminescence studies of CdTe solar cells," *J. Appl. Phys.*, vol. 94, (5), pp. 3549-3555, 2003.
- [113] Alexis De Vos, "The fill factor of a solar cell from a mathematical point of view," *Solar Cells*, vol. 8, (3), pp. 283-296, 1983.
- [114] B. E. McCandless, "CdTe Solar Cells: Processing Limits and Defect Chemistry Effects on Open Circuit Voltage," *MRS Proceedings*, vol. 1538, pp. 249-260, 2013.
- [115] R. S. Muller and T. I. Kamins, "Section 1.2, equation 1.2.20," in *Device Electronics for Integrated Circuits by Muller and Kamins, 2nd Ed.* 2003, pp. 36.
- [116] M. Gloeckler, A. L. Fahrenbruch and J. R. Sites, "Numerical modeling of CIGS and CdTe solar cells: Setting the baseline," in *Proceedings of 3rd World Conference on Photovoltaic Energy Conversion*, 2003.
- [117] A. L. Fahrenbruch and R. H. Bube, "Section 4.4.2," in *Fundamentals of Solar Cells* Anonymous New York: Academic Press, Inc., 1983, pp. 78.

-
- [118] R. S. Muller and T. L. Kamins, "Section 5.3, equation 5.3.10," in *Device Electronics for Integrated Circuits, 3rd Ed.*, R. S. Muller and T. I. Kamins, Eds. Wiley India Edition, 2003, pp. 241.
- [119] R. S. Muller and T. L. Kamins, "Equation 5.3.15," in *Device Electronics for Integrated Circuits* New Delhi: Wiley India Edition, 2003, pp. 243.
- [120] T. Ishikawa, "Grid-connected photovoltaic power systems: survey of inverter and related protection equipments," *Report IEA PVPS T5-05*, vol. 2006, 2002.
- [121] Hitachi Technical Staff, *Spec. Sheet for Hitachi Hiverter NP201i PWN Solar Inverter* Hitachi, Accessed Jun 2018.
- [122] G. Notton, V. Lazarov and L. Stoyanov, "Optimal sizing of a grid-connected PV system for various PV module technologies and inclinations, inverter efficiency characteristics and locations," *Renewable Energy*, vol. 35, (2), pp. 541-554, 2010

Appendix A

DERIVATION OF V_{OC} DEPENDENCE ON DOPING USING CURRENT CONTINUITY EQUATIONS

As an alternative to Eq. 1-16 to 1-21, the V_{OC} dependence on doping can also be derived using the continuity equations for current and carrier concentration as follows. We start with the basic equation for V_{OC} based on lumped circuit model of a solar cell with net current =0 and solve for resulting voltage, which is by definition V_{OC} :

$$V_{OC} = \frac{nkT}{q} \ln \left(\frac{J_L}{J_0} \right) \quad (A-1)$$

This equation is used to derive the V_{OC} of a CdTe solar cell, using the current continuity equations in the light to determine J_L , and in the dark to determine J_0 .

A.1 Current transport model for CdTe devices of this study

We first determine whether CdTe solar cells studied in this work qualify as a long-base ('semi-infinite absorber device' where absorber width, $W \gg$ electron diffusion length, L_n) or short-base ('finite absorber device' where W is comparable to L_n). Using Einstein's relation [115] given in equation (A-2), with a minority carrier (electron) mobility $\mu_n = 320 \text{ cm}^2/\text{V}\cdot\text{s}$ [116], and an assumed lifetime, τ_n , between 0.1 and 1 ns relevant to the devices of this study, L_n is calculated as follows:

$$D_n = \left(\frac{kT}{q}\right) \mu_n = 25.8 \text{ mV} \times 320 \frac{\text{cm}^2}{\text{V-s}} = 8.26 \frac{\text{cm}^2}{\text{s}} \quad (\text{A-2}),$$

$$L_n = \sqrt{D_n \tau_n} = \sqrt{8.26 \frac{\text{cm}^2}{\text{s}} \times (0.1 \text{ to } 1) \text{ ns}} = 0.3 \text{ to } 0.9 \mu\text{m} \quad (\text{A-3})$$

Comparing this with the absorber (CdTe) thickness of $\sim 10 \mu\text{m}$ makes the case of electronic transport in these devices to be that of a ‘semi-infinite absorber thickness’ [117]. For this condition, we use equation (A-1) to derive the V_{OC} after first computing the light-generated current density, J_L , and the dark current using current continuity equations.

A.1 Derivation of light-generated current for a semi-infinite absorber case

J_L is given by the current density at the edge of the depletion region on the p-type absorber side, $J_n(x_p)$ as:

$$J_L = J_n(x_p) = qD_n \left. \frac{\partial n_p}{\partial x} \right|_{x=x_p} \quad (\text{A-4})$$

where D_n is the diffusivity of the minority carriers, electrons, in the p-type CdTe absorber, n_p is the minority carrier concentration

To solve this, the concentration of light-generated excess carriers should be solved for, using the continuity equation for diffusion of light generated minority carriers. [118] This is derived from the fact that the net change in the concentration of charge carriers under illumination in an infinitesimal space is given as a sum of the current flowing in and out of the volume and of the generation and recombination of the carriers.

$$\frac{\partial^2 n_p}{\partial x^2} - \frac{(n_p - n_{p0})}{D_n \tau_n} = -\frac{G(x)}{D_n} = -\frac{\alpha \Gamma}{D_n} \exp[-\alpha(x - x_p)] \quad (\text{A-5})$$

where $\Gamma = \Gamma(x)$ is the monochromatic illumination photon flux density at $x = x_p$, $\alpha(\lambda)$ is the absorption coefficient as a function of the wavelength of the photon flux, λ , and $G(x)$, the generation rate. The boundary conditions are:

$$n_p(x_p) = n_{p0} \exp\left(\frac{qV}{kT}\right), \quad n_p(x = \infty) \rightarrow n_{p0} \quad (\text{A-6}),$$

The solution to this differential equation is then given by,

$$n_p = n_{p0} \left[\exp\left(\frac{qV_a}{kT} - 1\right) \exp\left[-\frac{(x-x_p)}{L_n}\right] + \frac{\alpha \Gamma(\lambda)}{D_n \left(\alpha^2 - \frac{1}{L_n^2}\right)} \left\{ \exp\left(-\frac{x-x_p}{L_n}\right) - \exp[-\alpha(x - x_p)] \right\} \right] + n_{p0} \quad (\text{A-7})$$

where V_a is the applied bias and $L_n \equiv \sqrt{D_n \tau_n}$ as in equation (A-3).

The electron current from diffusion at the edge of the depletion layer width is defined here as the light-generated current, given as:

$$J_L = J_n(x_p) = qD_n \left. \frac{\partial n_p}{\partial x} \right|_{x=x_p} \quad (\text{A-8})$$

From the above equations, light-generated current can be derived as follows:

$$J_n(x) = -\frac{(qD_n n_{p0})}{L_n} \exp\left[-\frac{(x-x_p)}{L_n}\right] \left[\exp\left(\frac{qV}{kT}\right) - 1 \right] + \frac{q\alpha \Gamma(\lambda)}{\left(\alpha^2 - \frac{1}{L_n^2}\right)} \left\{ \alpha \exp[-\alpha(x - x_p)] - \frac{1}{L_n} \exp\left[-\frac{(x-x_p)}{L_n}\right] \right\} \quad (\text{A-9})$$

Hence, the short circuit current, J_L , given by equation (A-8), at the depletion layer edge, x_p , and at 0 V bias for this monochromatic flux would be:

$$J_L(\lambda) = J_n(x_p, V_a = 0V) = \frac{q\Gamma(\lambda)}{\left(1 + \frac{1}{\alpha L_n}\right)} \quad (\text{A-10})$$

This current, when integrated for the incident spectrum can be given as:

$$J_L = \int J(\lambda) d\lambda = \int \frac{q\Gamma(\lambda)}{\left[1 + \frac{1}{\alpha(\lambda)L_n}\right]} d(\lambda) \quad (\text{A-11})$$

This can be rewritten by defining a carrier concentration, Δn_{p0} , given by:

$$\Delta n_{p_0} \equiv \frac{L_n}{D_n} \int \frac{q\Gamma(\lambda)}{\left[1 + \frac{1}{\alpha(\lambda)L_n}\right]} d(\lambda) \quad (\text{A-12})$$

From this, the light-generated current can be given as:

$$J_L = \frac{qD_n}{L_n} \Delta n_{p_0} \quad (\text{A-13})$$

A.2 Dark saturation current

Similarly writing the continuity equations of the voltage-dependent current in the dark yields J_0 , the dark saturation current to be given by: [119],

$$J_0 = qn_i^2 \left(\frac{D_p}{N_d L_p} + \frac{D_n}{N_a L_n} \right) \quad (\text{A-14})$$

where N_d and N_a are the donor and acceptor doping densities on the n-type CdS emitter layer and the p-type CdTe absorber layer respectively. Since $N_d = 10^{17} \text{ cm}^{-3} \gg N_a$, J_0 can be approximated as:

$$J_0 \approx qn_i^2 \left(\frac{D_n}{N_a L_n} \right) \quad (\text{A-15})$$

A.3 Derivation of V_{OC}

Using equations (A-13) and (A-15) in (A-1) then gives V_{OC} as:

$$V_{OC} = \frac{kT}{q} \ln \left[\frac{\left(\frac{qD_n \Delta n_{p_0}}{L_n} \right)}{qn_i^2 \left(\frac{D_n}{N_a L_n} \right)} \right] \quad (\text{A-16})$$

$$\Rightarrow V_{OC} = \frac{kT}{q} \ln \left(\frac{\Delta n_{p_0} N_a}{n_i^2} \right) \quad (\text{A-17}),$$

which is similar to the equation 1-21 for V_{OC} . Hence V_{OC} can be improved by enhancing the absorber doping density with sufficiently high carrier lifetime as given below.

$$\Delta V_{OC} = \frac{nkT}{q} \Delta \ln(N_A) \quad (\text{A-18})$$

Appendix B

A DETAILED DESCRIPTION OF PV-EC LOAD-MATCHING MODEL

This chapter describes the *load-matching* model discussed in Chapter 2 with the CO₂ flow-cell electrolyzer processed by Wesley Luc *et al.* [62], [63], [64] and SunPower[®] solar cell combination. This appendix provides a more generalized description of the model, suitable for use with any PV-EC source-load combination. The goal of the *load-matching* model developed in this work is to optimally couple a PV-electrolyzer (source-load) combination to determine a configuration that yields maximum SFE. Section B.1 specifies the input to be provided to the model and Section B.2 discusses the output that the model is designed to compute. Section B.3 gives a detailed description of the algorithm. The *Origin*[®] analysis template used to implement the load-matching model is also provided here as a reference.

B.1 Model Input

This model needs the electrical characteristics of the individual solar cell/ solar module used as the photovoltaic (PV) power source and that of the electrochemical load. Consequently, the solar cell I-V data measured at standard testing conditions (STC), the electrolyzer voltammogram (its I-V curve) and its faradaic efficiency as a function of potential, FE(V) are given as inputs to the model.

B.2 Model Output

This model is designed to provide the parameters for the optimum configuration achievable for the given source-load combination. For large scale PV-EC systems (KW-MW), these parameters would be those pertaining to the solar array layout—number of panels to be connected in series per string and number of solar panel strings in parallel.

For smaller scale (<100 W, bench-scale) devices (such as the flow-cell CO₂ electrolyzer of Chapter-2), its output would be the parameters of the solar array as its individual solar cell area and number of cells in series.

B.3 Model assumptions

The load-matching model discussed here uses the dark I-V curve of a solar cell/solar panel and computes the light I-V curves for varying array configurations. To that end, it assumes that the light I-V curves of a solar cell/panel can be computed from its dark I-V curve *via* superposition with its short circuit current, I_{SC} , given by the diode equations below:

$$I_L(V) = I_D(V) + I_{SC} \quad (\text{B-1})$$

where

$$I_D(V) = I_0 \left\{ 1 - \exp\left(-\frac{qV}{kT}\right) \right\} \quad (\text{B-2})$$

However, if there are significant non-idealities present in the photovoltaic device, such as voltage-dependent collection losses [103]—similar to those arising from deep defects—the model cannot compute the I-V curves accurately. Considering that commercially-available high-performance single crystalline silicon solar cells were used for PV source, it can compute the results for the PV-EC's discussed in this work with reasonable accuracy.

B.4 Model Algorithm

The exact procedure to implement load-matching varies slightly with the scale of the system. Section B.3.1 gives the procedure for large-scale PV-EC's where the current and voltage output from a single PV unit (solar cell/panel) is smaller than the current and voltage requirement of the electrolyzer respectively. Section B.3.2 discusses

load-matching for smaller-scale devices, where the current output from a single PV unit (solar cell) is larger than the current requirement of the electrolyzer. Unless multi-junction PV components are used, the voltage output from a solar cell is typically smaller than the voltage requirement of electrolyzers for the reactions of interest in this work, i.e., H₂O and CO₂ reduction.

B.4.1 Load-matching for large-scale PV-EC systems

For larger-scale electrochemical systems (similar to the 2.1 MW H₂O electrolyzer discussed in chapter 4), configuring the PV array to the electrochemical device for maximum power delivery is simpler, since the output voltage and current can be controlled by using the discrete number of solar panels to be connected in series and parallel as the variables, respectively. Additionally, for large-scale PV-EC's the resulting system SFE is less sensitive to the 'quanta' of solar panels connected in series or parallel, compared to bench-scale PV-EC's. Consequently, the load-matching procedure for such a system simplifies to two steps, as listed below:

1. The number of solar cells required in series (n_s) is determined by dividing the electrolyzer voltage requirement (its desired operating point- $V_{OP_{EC}}$) with the maximum power voltage of the solar panel used as the power source ($V_{MP_{PV}}$). This is given by the following equation:

$$n_s = \frac{V_{OP_{EC}}}{V_{MP_{PV}}} \quad (\text{B-3})$$

2. The number of solar cells in parallel is determined by dividing the electrolyzer current at the desired operating point- $I_{OP_{EC}}$ with the maximum power current of the solar panel, as given by the equation below.

$$n_p = \frac{I_{OP_{EC}}}{I_{MP_{PV}}} \quad (\text{B-4})$$

B.5 Load-Matching for Small-Scale PV-EC's

If the scale of the PV-EC is small (similar to the CO₂ electrolysis device discussed in chapter 2 and 3), maximizing the SFE using a PV source with dissimilar voltage and current rating is more nuanced. This is further complicated if the electrochemical device has a sensitive FE(V) curve. This is explained as an algorithm as follows:

The minimum number of solar cells in series is determined by dividing the minimum voltage required to drive the electrochemical reaction of interest with the maximum power voltage output of the solar cell, as given by equation (B-3). Since the maximum power current output of the solar cell is larger than the minimum current requirement of the electrolyzer, the surface area (also referred to here as ‘illumination area’) of the solar cell is used to control the output current from the PV source, using which its SFE is optimized.

The I-V behavior of the solar component in the dark and in the light is used for the input, for known illumination area A_0 . The short-circuit current density (J_{SC}), open-circuit voltage (V_{OC}), maximum power current density (J_{MP}), maximum power voltage (V_{MP}), and lumped series resistance, R_S , are determined for a single solar cell. The single-cell dark I-V dataset of the PV component is given as $(V_{i_{PV}}^0, I_{i_{PV_{Dark}}}^0)$. Using this data, the voltage-current density dataset of single solar cell $(V_{i_{PV}}^0, J_{i_{PV_{Dark}}}^0)$ is determined as follows:

$$(V_{i_{PV}}^0, J_{i_{PV_{Dark}}}^0) = \left(V_{i_{PV}}^0, \frac{I_{i_{Dark}}^0}{A_0} \right) \quad (\text{B-5})$$

The J-V curve of a solar array made with n_s solar cells in series is then computed, using the following equation:

$$V_{i_{PV}}(n_s) = V_{i_{PV}}^0 \times n_s \quad (\text{B-6})$$

The minimum and maximum current values from the electrolyzer voltammogram data, $(V_{j_{EC}}, I_{j_{EC}})$, $(V_{j_{EC}}, FE_{j_{EC}})$ are used to determine the limits of solar cell areas to be considered— A_{min} and A_{max} —using the following equations:

$$A_{min} = \frac{I_{EC_{Min}}}{J_{MP}} \quad (\text{B-7})$$

$$A_{Max} = \frac{I_{EC_{Max}}}{J_{MP}} \quad (\text{B-8})$$

For the configuration with n_s cells in series, all possible solar cell illumination areas are considered, from A_{min} to A_{max} . The step size of these areas should be determined by the accuracy with which the solar cell area can be empirically controlled. Consequently, the I-V curves of all the solar array configurations with n_s cells in series for illumination areas, A_l , ranging from A_{min} to A_{max} is modeled using the following equations:

$$V_{i_{PV}}(n_s, A_l) = V_{i_{PV}}(n_s) \quad (\text{B-9})$$

$$I_{i_{PV_{Dark}}}(A_l) = J_{i_{Dark}} \times A_l \quad (\text{B-10})$$

$$I_{i_{PV_{Light}}}(n_s, A_l) = I_{i_{PV_{Dark}}} + (J_{SC} \times A_l) \quad (\text{B-11})$$

The resulting I-V curve for PV configuration, (n_s, A_l) , is used with the electrolyzer I-V curve to solve for the operating voltage and current. Graphically, this is equivalent to finding the intersection point of these two I-V curves. To solve these

equations numerically, the I-V data of PV array, $(V_{i_{PV}}, I_{i_{PV_{Light}}})$ (n_s, A_l), and that of the electrolyzer $(V_{j_{EC}}, I_{j_{EC}})$, along with its FE data, $(V_{j_{EC}}, FE_{j_{EC}})$ are first interpolated to a common voltage range of sufficient resolution, V_k as $(V_k, I_{k_{PV_{Light}}})$, $(V_k, I_{k_{EC}})$ and $(V_k, FE_{k_{EC}})$. For each index k , the difference between the electrolyzer and PV currents is computed as:

$$\Delta I_k(V_k) = \left| I_{k_{PV_{Light}}} - I_{k_{EC}} \right| \quad (\text{B-12})$$

Using this data set, the index $k = k_0$ is identified for the solution of these two curves, as the data point whose $\Delta I_k(V_k)$ is minimum. Consequently, the operating point is given by the data point, $(V_{k_0}, I_{k_0_{PV_{Light}}})$. The corresponding faradaic efficiency is also found at the same index as $FE_{k_0_{EC}}$. Using these values of operating current and FE for this configuration, (n_s, A_l) , its SFE is computed as,

$$SFE(n_s, A_l) = \frac{\mu_{th} \times I_{k_0_{PV_{Light}}} \times FE_{k_0_{EC}}}{A_l \times n_s \times S} \quad (\text{B-13})$$

where S is the solar illumination intensity under standard testing conditions (STC), 100 mW/cm². The SFE's calculated this way for all cell areas from $(A_{min}$ to A_{max}) are tabulated for n_s cells in series, from which the optimum array configuration is picked for an area A_l whose SFE is the largest. This procedure is repeated for arrays with $> n_s$ solar cells in series. However, as more cells are connected in series, the electrolyzer I-V intersects the PV array I-V at voltages farther away from its maximum power point, leading to decreasing SFEs.

B.5.1 Correcting for parasitic resistances:

The load-matching model was modified for the CO₂ electrolyzer (in Chapter 2) for parasitic interconnect resistance encountered in circuit implementation. When there is a non-negligible series resistance in the solar cell or the PV-EC circuit, the lumped

circuit resistance (R_C) is determined by dividing the measured operating voltage ($V_{OP_{meas}}$) with the operating current ($I_{OP_{meas}}$). Load-matching in this case can be modified by incorporating the voltage drop from this resistance either into the PV array or electrolyzer I-V curve. The detailed procedure is described below.

The solar array I-V curve data for all configurations, $(V_{i_{PV}}, I_{i_{PV}_{Light}})(n_s, A_l)$, is modified to incorporate the equivalent circuit resistance by modifying the voltage data points to account for the equivalent series resistance, given by equation () below:

$$V'_{i_{PV}}(n_s, A_l) = V_{i_{PV}} + (I_{i_{PV}} \times R_C) \quad (\text{B-14})$$

Following this, the operating point determination is performed in the same way as was described in the previous section, however, by replacing the PV voltage data $(V'_{i_{PV}}, I_{i_{PV}_{Light}})(n_s, A_l)$ instead of $(V_{i_{PV}}, I_{i_{PV}_{Light}})(n_s, A_l)$. This voltage correction can also be performed with the load I-V curve instead, which would effectively yield the same results. However, only one of the source or load I-V curves should be modified, not both.

In the work presented in chapter 2, this equivalent resistance was determined to be $\sim 0.14 \Omega$. (This is the equivalent resistance value obtained by averaging the same for all 4 configurations, given in Table 2-3). This modeled results modified using this procedure yielded SFE's that matched with measured SFE's within 3% error with the measured values (Table 2-4).

A.4 Implementing Load-Matching Model Using *Origin*[®] Analysis Template

Origin Graphing and Analysis[®] software was used to implement the load-matching model developed in this work. It is a graphing and analysis software capable of performing column operations on large data sets. It allows simple creating analysis templates, enabling easy repetitive processing. A tabulated account of the *Origin*[®]

analysis template made to implement the load matching model for a PV-EC combination is given in Table B-1.

The template columns (A, B, C..) are reproduced here, transposed as table rows. The corresponding column information such as the parameter in its content, units, and the function used, where applicable are given as columns. The comments given for each row (representing the *Origin*[®] column) explain its contents in detail. This table also provides the equations corresponding to the *Origin*[®] function used in some of the columns. The origin columns and their formulae given in this table can be reproduced in an *Origin*[®] spreadsheet (in the same order as given here) to yield similar calculations on a PV-EC whose input data sets are known. The rows given here are color-coded as follows:

- **blue** (rows) represent columns with dataset given as the *input* to this model,
- **purple** rows represent columns used to perform operations on data,
- **green** rows represent columns with the independent parameter, against which the output is being calculated (here, the solar cell area, A_l)
- **red** rows represent columns with the desired final output, which in this case is the $SFE(A_l, n_s)$.

Table B-1: A tabulated account of the *Origin*[®] template used to implement the load matching model for a PV-EC combination. The *Origin*[®] columns are transposed here as the table rows, along with information about its contents: the parameter, its units, the function used to perform operations. Comments given here provide a more detailed description of the parameter, and the equation column provides the corresponding equation pertaining to the *Origin*[®] function used, where applicable

Column	Parameter	Units	<i>Origin</i> [®] Function	Comments	Equation
A	Cell Area	cm ²	N/A	Solar cell area (the independent variable)	A_l
B	$V_{PV, Dark}$	V	N/A	Voltage in $(V_i, I_{iPV_{Dark}})$ dataset	$V_i \in (V_i, I_{iPV_{Dark}})$
C	$I_{PV, Dark}$	A	N/A	Dark current in $(V_i, I_{iPV_{Dark}})$ dataset	$I_i \in (V_i, I_{iPV_{Dark}})$
D	$J_{PV, Dark}$	mA/cm ²	C*1000/153.44	Dark current density calculated from dark current of full cell (153.44 is the full cell area of the SunPower [®] solar cell used)	$J_{PV_{Dark}} = \frac{I_{Dark}}{Cell Area}$
E	J_{Light}	mA/cm ²	6.22*100/154	Solar cell J_{SC}	$J_{SC} = \frac{I_{SC_{rated}}}{Cell Area}$
F	R_S	Ω	1.41	Equivalent circuit resistance	R_S

G	I_{Light}	mA	(E1+D)* A1	Equivalent PV current output in <i>Light</i> (as a function of the solar cell area considered)	$I_{i_{PV}} = (J_{i_{PV_{Dark}}} + J_{SC}) \times A_l$
H	V_{Light}	V	B-G/1000* F1	PV equivalent voltage across PV terminals	$V_{i_{PV}} = (I_{i_{PV}}) \times R_W$
I	I_{Light}	mA	G	PV current in light reproduced here	$I_{i_{PV}}$
J	P	mW	H*I	PV output power	$P_{i_{PV}} = V'_{i_{PV}} \times I_{i_{PV}}$
K	V_{EC}	V	N/A	Voltage from $(V_j, I_{j_{EC}})$	$V_{j_{EC}}$
L	I_{EC}	mA	N/A	Current from $(V_j, I_{j_{EC}})$	$I_{j_{EC}}$
M	FE	%	N/A	Faradaic efficiency from $(V_j, FE_{j_{EC}})$ dataset, <i>Input</i>	$FE_j(V_j)$
N	$I_{EC}(V'_{PV, Light})$	mA	table (K,L,H)	$I_{j_{EC}}$ as a function of $V'_{i_{PV}}$ to rearrange PV, and EC (V, I) against the same voltage range	This function identifies the electrolyzer current values for the voltages from the $(V_{i_{PV}}, I_{i_{PV}})$ dataset

O	ΔI	mA	abs(I-N)	$\Delta I_i \equiv (I_{i_{PV}} - I_{i_{EC}})$ at every $V_{i_{PV}}$ dataset	$\Delta I = I_{i_{PV}} - I_{i_{EC}} $
P	Min (ΔI)	mA	min(O)	Finding minimum value of ΔI for point of intersection	Find $i=k$ for which $\Delta I \approx 0$
Q	V_{OP}	V	table (O,H,P)	Find operating voltage using minimum value of ΔI . This function gives the value of voltage at the index $i=k$ for which ΔI_i is minimum.	$V_{OP} = V_{k_{PV}}$ $k = i$ for which $\Delta I \approx 0$
R	I_{OP}	mA	table (O,N,P)	Operating current, I_{OP} . This function gives the value of electrolyzer current from the $I_{i_{EC}}$ dataset at the index $i=k$ for which ΔI is minimum.	$I_{OP} = I_{k_{EC}}$ $k = i$ for which $\Delta I \approx 0$

S	$I_{OP, PV}$	mA	table (O,I,P)	Operating current taken from PV (V,I) dataset (This should be very close to the value in column R, but is computed to verify how closely the intersection point was determined, which is optional)	$I_{OP} = I_{k_{PV}},$ $k = i$ for which $\Delta I \approx 0$
T	FE (V_{OP})	%	table (K,M,Q)	FE at the operating point, taken at the index $i=k$ for which ΔI_i is minimum	$FE_{OP} = FE_k,$ $k = i$ for which $\Delta I \approx 0$
U	η_{PV}	%	$\max(J)/A$ 1/5	Resulting PV η	$\eta_{PV}(A_l) = \frac{\max(P_{i_{PV}})}{A_l}$
V	SFE	%	$1.34 * R /$ $A1/5 * T / 1$ 00	Resulting SFE	$SFE(A_l) = \frac{\mu_{TH} \times I_{OP}(A_l) \times FE(A_l)}{A_l \times n_s \times P_{Sun}}$

Appendix C

A DETAILED DESCRIPTION OF PV-EC ANNUAL GENERATION MODEL

This chapter describes the *annual generation model* discussed in Chapter 3 and 4 in greater detail and in a generalized form, suitable for application to any PV-EC source-load combination.

C.1 Model Input

This model uses the I-V behavior of the PV source and the electrochemical load (solar array and electrolyzer I-V curves, along with electrolyzer FE curve, if applicable) as its input, as with the load-matching model. Additionally, it uses the hourly solar irradiation and temperature data of a location of choice as its input, for an entire year. For locations in the USA, this weather data can be acquired from NREL's National Solar Radiation Database (NSRDB). [76]

C.2 Model Output

This model is designed to yield the hourly SFE and gas output (in g/hr) from a PV-EC device/system for an entire year, using the weather data of the corresponding location. More specifically, it is designed to calculate the SFE and gas output of a PV-EC for variable irradiation and temperature conditions. In this work, weather data for *Wilmington, DE, USA* was used from which hourly insolation and air temperature data was used to compute PV-EC SFE for every hour with >0 irradiation. This made up for 4,723 data points for which SFE and gas output was computed. The hourly data computed this way can be used in several ways: to integrate and compute yearly PV-EC yield, to assess daily/seasonal fluctuations in PV-EC yield, and to understand its sensitivity to insolation and temperature. This model can also be supplemented with

cost analysis for a more complete assessment of a system. This, however, was not considered within the scope of this work.

C.3 Model Assumptions

The annual generation model discussed here uses the dark I-V curve of a solar cell/ solar panel and computes the light I-V curves for changing solar insolation and temperatures, given by the translation equations in Chapter 3. (equation (3-2) to (3-6)). To that end, it assumes that the light I-V curves of a solar cell/panel/array can be computed from its dark I-V curve by superposition with short circuit current density, as shown in equations (B-1) and (B-2), with series resistance incorporated where necessary. However, in the presence of significant non-idealities in the photovoltaic device, such as voltage-dependent collection losses, [103] similar to those arising from deep defects, the model cannot compute the I-V curves accurately. Considering that commercially-available high-performance single crystalline silicon solar cells were used for PV source, this model provides sufficient accuracy for the results it computed for the PV-EC's discussed in this work. This model also assumes a constant electrolyzer performance that does not vary over time, which might be not applicable for lab-scale devices that do not exhibit stability over the entirety of its operation.

C.4 Computing PV Array Output Using PV 'Translation' Equations

The PV-'translation' equations provided in Chapter 3 were used to implement the annual generation model by computing the PV-EC SFE for a given 'operating point', determined by a solar illumination intensity, S , and ambient temperature, T . The solar cell/panel operating temperature is determined by using the normal operating cell temperature (NOCT) parameter, provided in its spec sheet, using equation (3-2). The

dark solar array I-V curve, measured at standard testing conditions (STC) is given as $(V_{i_{PV}}^0, I_{i_{PV}}^0)$.

$$(V_{i_{PV}}^0, I_{i_{PV}}^0) \equiv (V_{i_{PV}}, I_{i_{PV}})(STC) \quad (C-1)$$

Using this data set, the array voltage is calculated for each insolation, temperature data point, (S, T) , by using the PV module temperature coefficient, β for voltage (obtained from its spec sheet), as:

$$V'_{i_{PV}}(S, T) = V_{i_{PV}}^0 \times \{1 - \beta(T - 25^\circ C)\} \quad (C-2)$$

Similarly, using the temperature coefficient for current, the current for (S, T) is determined as:

$$I_{i_{PV}}(S, T) = I_{i_{PV}}^0 - I_{SC} + \frac{I_{SC}}{\{1 + \alpha(T - 25^\circ C)\}} \times \frac{S}{1000 \frac{W}{m^2}} \quad (C-3)$$

where I_{SC} is the short-circuit current from the solar array at STC. Following this, the array voltage, $V'_{i_{PV}}(S, T)$ is corrected for solar panel equivalent lumped circuit series resistance, R_S as follows:

$$V_{i_{PV}}(S, T) = V'_{i_{PV}}(S, T) - I_{i_{PV}}(S, T) \times R_S \dots (C-4)$$

Using these values of voltage and current computed for the operating condition (S, T) , the new solar array I-V curve, $(V_{i_{PV}}, I_{i_{PV}})(S, T)$, is computed. For each data point, the PV power, $P_{i_{PV}}$, is computed and the maximum power point on the solar cell, $P_{Max_{PV}}$, is determined as follows:

$$P_{i_{PV}}(S, T) = V_{i_{PV}}(S, T) \times I_{i_{PV}}(S, T) \quad (C-5)$$

$$P_{Max_{PV}}(S, T) = Max (P_{i_{PV}}) \quad (C-6)$$

C.5 Incorporating Wiring Resistance

PV array wiring is typically designed for wiring-related voltage losses to be <2% of array maximum power voltage at STC, $V_{MP_{STC}}$. Consequently, wiring losses can be incorporated in the annual generation model as a single resistance value, R_w , in the array I-V curve computation, calculated as given below:

$$R_w = \frac{V_{MP_{STC}}}{I_{MP_{STC}}} \times \frac{r_w}{100} \quad (C-7)$$

where r_w is the percentage voltage drop that the array wiring is designed for, and $I_{MP_{STC}}$ is the array maximum power current. Using this value of equivalent wiring resistance, the I-V curves can be recomputed in the presence of a non-negligible wiring resistance by replacing R_S in equation (C-4) with $R_{Total} = R_S + R_w$.

C.6 Calculating PV-EC Operating Point

C.6.1 Direct coupling

The I-V and FE(V) curve of the electrolyzer are given as $(V_{i_{EC}}, I_{i_{EC}})$ and $(V_{i_{EC}}, FE_i)$, respectively. The I-V dataset of the solar array, $(V_{i_{PV}}, I_{i_{PV}})(S, T)$, is interpolated to the same voltage dataset as that of the electrolyzer, $V_{i_{EC}}$, (or vice versa) to give $(V_{i_{EC}}, I_{i_{PV}}(V_{i_{EC}}))(S, T)$. The resulting PV and electrolyzer I-V curves are solved to determine the PV-EC operating point for the operating condition given by (S, T) . The solution is obtained numerically by first computing the parameter $\Delta I_i \equiv |I_{i_{EC}} - I_{i_{PV}}(V_{i_{EC}})|$ at each data index i and identifying the data index, $k = i$, for which ΔI_i is minimum. Consequently, the operating point is given as $(V_{k_{EC}}, I_{k_{EC}})$. In this manner,

the operating points for each hour of varying solar insolation and temperature are computed for a *directly-coupled* PV-EC, from which the SFE and gas output are determined from equations (3-7) and (3-8). Wiring resistance in this model is implemented in the same way as described in Section B.4.1.

C.6.2 DC power optimizer coupling

The annual generation model developed in this work is also designed to compute annual yield from a PV-EC that is equipped with ‘*DC power optimizer*’ discussed in Section 3.3.1. This is achieved by finding the $P_{MaxPV}(S, T)$ at each operating condition and converting this power into a voltage-current product with voltage and current values that belong to the electrolyzer I-V data set. The detailed procedure is discussed below.

The electrolyzer I-V curve, $(V_{i_{EC}}, I_{i_{EC}})$, is used to compute the operating power for each voltage $P_{i_{EC}} = V_{i_{EC}} \times I_{i_{EC}}$. Next, the data index $k = i$ is identified for which $P_{k_{EC}} \approx \eta_{MPPT} \times P_{MaxPV}(S, T)$, where η_{MPPT} represents the power conversion efficiency of the DC power-optimizer. The operating point for a PV-EC equipped with DC power optimizer at this operating condition, (S, T) , is then given by the data index k as $(V_{OP_{MPPT}}, I_{OP_{MPPT}}) = (V_{k_{EC}}, I_{k_{EC}})$. The corresponding faradaic efficiency, $FE_{OP_{MPPT}}$, is then picked as the FE value at the same index k , as $(V_{k_{EC}}, FE_k)$. Using these parameters, the SFE (referred to here as ‘ SFE_{MPPT} ’) and hourly gas output are calculated from equations (3-7) and (3-8).

C.6.3 Inverter Coupling

In this work, the inverter coupling is incorporated in a more nuanced way as opposed to the incorporation of DC-power-optimizer devices. While DC power optimizer device was modeled for a constant power conversion efficiency, η_{MPPT} , in

the case of inverter coupling, the power conversion efficiency was considered to be variable with changing PV array output (as is the case with real solar inverters). [120] The efficiency curve $\eta_{inverter}$ of a Hitachi® *NP215i Series* inverter as a function of the ratio of the PV power at its input to its rated operating power, r_p , (η_{c_i}, r_{p_i}), was obtained from its spec sheet [120] and was used in the model to compute the yield of an inverter-coupled PV-EC. This procedure is explained as follows:

In the model, the inverter's rated power is assumed to be equal to the STC output power of the PV system, since this is close to how inverters are chosen for the design of real PV arrays. [122] The inverter efficiency for each operating point (S, T) is thus determined by computing the ratio of PV output power to rated power, r_p , for the operating condition (S, T) as:

$$r_p(S, T) = \frac{P_{MaxPV}(S, T)}{P_{MaxPV}(STC)} \quad (C-8)$$

where $P_{MaxPV}(STC)$ is the STC power output from the solar array. The inverter efficiency for this value of R_p is determined using the (η_{c_j}, r_{p_j}) dataset as $\eta_c(S, T)$. Using this value of inverter power conversion efficiency, the PV output power is derated to $\eta_{inverter}(S, T) \times P_{MaxPV}(S, T)$ and the corresponding operating point is computed in a similar way as shown in Section C.6.1 for the DC power optimizer coupling for every (S, T) .

The PV-EC operating points are computed this way for direct, DC power-optimizer, and inverter coupling for changing insolation and temperature conditions for every hour, (S_j, T_j) , for which $S_j > 0 \frac{W}{m^2}$. The resulting hourly data can be used in several ways as described in Section C.2. In this work, the results from annual generation model were used to compute annual-average SFE and total gas output, using

which the different coupling strategies were explored. Daily fluctuations in SFE were also explored for the 2.1 MW H₂O PV-EC discussed in Chapter 4.

C.7 Implementing Annual Generation Model for Direct-, Power Optimizer- and Inverter- Coupling Using *Origin*[®]

Origin Graphing and Analysis[®] software was used to implement the annual generation model developed in this work. A tabulated account of the *Origin*[®] analysis template made to implement the load matching model for a PV-EC combination is given in Table C-1.

The template columns (A, B, C..) are reproduced here, transposed as table rows. The corresponding column information such as the parameter in its content, units, and the function used, where applicable are given as columns. The comments given for each row (representing the *Origin*[®] column) explain its contents in detail. This table also provides the equations corresponding to the *Origin*[®] function used in some of the columns. The origin columns and their formulae given in this table can be reproduced in an *Origin*[®] spreadsheet (in the same order as given here) to yield similar computation for a PV-EC provided with appropriate input parameters. The rows given here are color-coded as follows:

- **blue** (rows) represent columns with dataset given as the *input* to this model,
- **purple** rows represent columns used to perform operations on data,
- **green** rows represent columns with the independent parameter, against which the output is being calculated (here, the solar cell area, A_l)
- **red** rows represent columns with the desired final output, which in this case is the $SFE(A_l, n_s)$.

Table .C-1: A tabulated account of the *Origin*[®] template used to implement the annual generation model for a PV-EC combination with direct-, dc power optimizer-, and inverter-coupling. The *Origin*[®] columns are transposed here as the table rows, and information about its contents are given as adjacent table columns. The ‘parameter’ column gives the name of the variable, the ‘units’ column gives the respective units, the ‘function’ column shows the exact function as used in the *Origin*[®] template to perform respective column operations. Comments given here provide a more detailed description of the parameter, and the equation column provides the corresponding equation pertaining to the *Origin*[®] function used, where applicable

Column	Parameter	Units	Comments	<i>Origin</i> [®] Function	Equation
A	Month	N/A	Month of the year from Weather data	N/A	N/A
B	Day	N/A	Day of the month from weather data	N/A	N/A
C	Hour	N/A	Hour of the day from weather data	N/A	N/A
D	S	W/m ²	Solar insolation		$S_l \in (S_l, T_l)$
E	T _{air}	°C	Air temperature, T		$T_l \in (S_l, T_l)$
F	T _{PV}	°C	Solar cell/panel temperature for the given air temperature	$E+(45-20)*D/800$	$T = T_{module} = T_{air} + \frac{NOCT-20^{\circ}C}{80} \times S$
G	V _{PV, Dark}	V	Voltage point taken from single-cell/module dark I-V		$V_{iPV_{Dark}}$

			measureme nt of the solar cell		
H	$I_{PV, Dark}$	A	Current point taken from single- cell/module dark I-V measureme nt of the the solar cell		$I_{i_{PV_{Dark}}}(V_{i_{PV_{Dark}}})$
I	I_{EC}	A	Current point taken from I-V measureme nt of the electrochem ical cell (its voltammogr am). Note that this is plotted against the same voltage dataset as that of the dark I-V data of the solar cell		$I_{i_{EC}}(V_{i_{PV_{Dark}}})$

J	FE		Faradaic efficiency of electrolyzer, as a function of its voltage (if applicable)		$FE_{i_{EC}}(V_{i_{PV_{Dark}}})$
K	Solar cell/panel individual area	m ²	Individual area of the photovoltaic component (solar cell/panel) used		A_{PV}
L	n_s		Number of solar panels in series (determined using load matching model)		n_s
M	n_p		Number of strings (of solar panels) in parallel (determined using load matching model)		n_p

N	$\Delta V_{PV}(T)$	V	Voltage drop for this corresponding data point (of index i) due to temperature variation from STC temperature of 25°C	$0.435*(F1-25)*626$	$\Delta V_i(T_l) = \beta(T_l - 25^\circ C)$
O	$I_{SC}(S,T)$	A	Rated short circuit current of the solar cell (panel), corrected here for operating temperature	$(6.45*64/1000*D)+(2.6/1000*64*(F1-25))$	$I_{SC}(S_l, T_l) = \frac{I_{SC,STC}}{[1+\alpha(T_l-25^\circ C)]} \times \frac{S_l}{1000 \frac{W}{cm^2}}$
P	$I_{PV, Light}(S)$	A	Operating current for the given voltage point (of index i), as a function of insolation and temperature	H+O1	$I_{i_{PV}}(S_l, T_l) = I_{i_{PV}dark} + I_{SC}(S_l, T_l)$
Q	$V_{PV}(S,T)$	V	Operating voltage for the corresponding index (i), corrected for temperature, and series resistance R_s	$G-N1-(P/64*0.5804*626)$	$V_{i_{PV}Light} = V_{i_{PV}Dark} - \Delta V_i(T_l) - V_{i_{PV}Dark} \times R_s$

R	$P_{PV}(S,T)$	W	Power calculated for this corresponding index i	$P*Q$	$P_{iPV_{Light}} = V_{iPV_{Light}} \times I_{iPV_{Light}}$
S	$P_{PV, max}$	W	Maximum power output from the solar cell/module/array for this operating temperature and insolation	$\max(R)$	$P_{PV_{Max}} = \max(P_{iPV_{light}})$
T	V_{MP}	V	Maximum power voltage extracted from the maximum power point, of index $i=k$ where $P_k = \max(P_i)$	table (R,Q,S)	$V_{MP} = V_{kPV_{Light}}$, where $k = i$, given by $P_{PV_{Max}} = \max(P_{iPV_{light}})$
U	I_{MP}	A	Maximum power current extracted from the maximum power point, of index $i=k$ where $P_k = \max(P_i)$	table (R,P,S)	$I_{MP} = I_{kPV_{Light}}$, where $k = i$, given by $P_{PV_{Max}} = \max(P_{iPV_{light}})$

V	$I_{EC} (V_{PV})$	A	I_{EC} , picked for voltage dataset $V_{PV, Light}$, as given in column Q	table (G,I,Q)	$I_{j_{EC}} (V_{j_{PV_{Light}}})$
W	ΔI	A	ΔI computed to find the intersection point between the electrolyzer and the solar array I-V curves computed for this insolation and temperature	abs(P-V)	$\Delta I_j = \left I_{j_{PV_{Light}}} - I_{j_{EC}} (V_{j_{PV_{Light}}}) \right $
X	ΔI_{min}	A	Identifying minimum value of ΔI to find the intersection point between the solar array and electrolyzer I-V curves	Min(W)	$\Delta I_{min} = \min(\Delta I_j)$
Y	V_{OP}	V	Identifying the operating voltage by finding the voltage at index i where $\Delta I=0$	table (W,Q,X)	$V_{OP} = V_{k_{PV_{Light}}}$ for k=j for which $\Delta I_j = \Delta I_{min}$

Z	I_{OP}	A	Operating current of the directly connected PV-EC setup, computed by identifying the intersection point between the solar array and electrolyzer I-V curves, as described in Appendix B	table (W,P,X)	$I_{OP} = I_{k_{PV}Light}$ for k=j for which $\Delta I_j = \Delta I_{min}$
AA	P_{OP}	W	Operating Power	Y*Z	$P_{OP}(S_l, T_l) = V_{OP} \times I_{OP}$
AB	FE_{OP}	%	Faradaic efficiency at the operating point, identified using the intersection point between the solar cell/module/array and electrolyzer I-V curves	table (G,M,Y)	$FE_{OP} = FE(V_{OP})$

AC	SFE _{Direct}	%	Corresponding SFE for this operating conditions-insolation and temperature with <i>direct coupling</i>	$1.34 \cdot Z/K/L/M \cdot Y/D \cdot 10^0$	$SFE(S, T) = \frac{\mu_{th} \times I_{OP}(S, T)}{S \times A_{PV} \times n_s \times n_p} \times FE_{OP}(S, T)$, as given in equation (3-7)
AD	g _{Direct}	g/hr	Corresponding gas output for this operating conditions-insolation and temperature with <i>direct coupling</i>	$Z^* AB/100/2/(1.602E-19)/(6.022140857E23) \cdot 3600 \cdot 28.01$	$g(S, T) = \frac{I_{OP}(S, T) \times 3,600 \times FE(S, T) \times M}{q \times N \times A}$ given in equation (3-8)
AE	η_{MPPT}	%	Power conversion efficiency of DC power Optimizer	100	η_{MPPT}
AF	P _{PV,MPPT}	W	Corresponding input power delivered to electrolyzer	R*AE	$P_{INEC} = P_{PVMax} \times \eta_{MPPT}$
AG	P _{EC}	W	Current-voltage product of electrolyzer from its voltammogram data	I*G	$P_{iEC} = V_{iEC} \times I_{iEC}$

AH	$V_{OP, MPPT}$	V	Operating voltage with DC power optimizer connection (referred to in this code as ‘MPPT’), identified by finding the power point in PEC column that is equal to PPV,MPPT	table (AG,G,AF)	$V_{OP_{MPPT}} = V_{i_{PV_{Dark}}}$ given by i, for which $P_{IN_{EC}} = P_{i_{EC}}$
AI	$I_{OP, MPPT}$	A	Operating current under ‘MPPT’ coupling	table (AG,I,AF)	$I_{OP_{MPPT}} = I_{i_{PV_{Dark}}}$ given by i, for which $P_{IN_{EC}} = P_{i_{EC}}$
AJ	$FE_{OP, MPPT}$	%	Faradaic efficiency under MPPT coupling	table (AG,J,AF)	$FE_{OP_{MPPT}} = FE_{i_{EC}}$ given by i, for which $P_{IN_{EC}} = P_{i_{EC}}$
AK	SFE_{MPPT}	%	Resulting SFE with MPPT coupling	$1.34 * AI * AJ / K / L / M * Y / D * 100$	$SFE_{MPPT}(S, T) = \frac{\mu_{th} \times I_{OP_{MPPT}}(S, T)}{S \times A_{PV} \times n_s \times n_p} \times FE_{OP_{MPPT}}(S, T)$, as given in equation (3-7)
AL	g_{MPPT}	g/hr	Resulting gas output for an hour with MPPT coupling	$AI * AJ / 100 / 2 / (1.602E-19) / (6.0221409E23) * 3600 * 28.01$	$g_{MPPT}(S, T) = \frac{I_{OP_{MPPT}}(S, T) \times 3,600s \times FE_{OP_{MPPT}}(S, T) \times M}{q \times N \times A}$ given in equation (3-8)

AM	$R_{Inverter}$		Ratio of PV output power to inverter rated power, taken from Inverter efficiency curve given in its spec sheet		$R_{inverter} \epsilon(R_i, \eta_i)$
AN	$\eta_{Inverter}$	%	Inverter efficiency as a function of its input power to rated power ratio		$\eta_{inverter} \epsilon(R_i, \eta_i)$
AO	P_{Rated}	W	Power rating of the inverter, ideally equal to STC power output of the PV array		$P_{Rated_{inverter}}$
AP	$R_{Inverter}(S,T)$		Ratio of PV power output to inverter power rating	S/AO	$R_{inverter} = \frac{P_{PVMax}}{P_{Rated_{inverter}}}$
AQ	$\eta_{Inverter}(S,T)$	%	Inverter efficiency corresponding to this operating condition (S,T)	table (AM,AN, AP)	$\eta_{inverter}(S,T)$

AR	$P_{PV, Inverter}$	W	Resulting power delivered to the electrolyzer from PV+inverter connection	$S \cdot AQ/100$	$P_{PVinverter}(S, T) = \eta_{inverter}(S, T) \times P_{PVMax}(S, T)$
AS	$V_{OP, Inverter}$	V	Operating voltage with inverter coupling, computed by identifying the power in the PEC column that is equal to $P_{PV, Inverter}$	table (AG,H,AR)	$V_{OPInverter} = V_{i_{PVDark}}$ given by i, for which $P_{PVinverter} = P_{i_{EC}}$
AT	$I_{OP, Inverter}$	A	Operating current with inverter coupling	table (AG,I,AR)	$I_{OPinverter} = I_{i_{PVDark}}$ given by i, for which $P_{PVinverter} = P_{i_{EC}}$
AU	$FE_{Inverter}$	%	Operating faradaic efficiency with inverter coupling	table (AG,J,AR)	$FE_{OPinverter} = FE_{i_{EC}}$ given by i, for which $P_{PVinverter} = P_{i_{EC}}$

AV	$SFE_{Inverter}$	%	Resulting SFE with inverter coupling	$1.34 \cdot AT \cdot A$ $J/K/L/M \cdot Y/D \cdot 100$	$SFE_{Inverter}(S, T)$ $\mu_{th} \times$ $\frac{I_{OP_{Inverter}}(S, T)}{S \times A_{PV} \times n_s \times n_p} \times$ $FE_{OP_{Inverter}}(S, T)$, as given in equation (3-7)
AW	$M_{Inverter}$	g/hr	Resulting gas output for inverter coupling, for the given insolation and temperature	$AT \cdot$ $AU/100/2/($ $1.602E-$ $19)/(6.0221$ $40857E23) \cdot$ $3600 \cdot 28.01$	$g_{Inverter}(S, T) =$ $\frac{I_{OP_{Inverter}}(S, T) \times$ $3,600s \times$ $FE_{OP_{Inverter}}(S, T)$ $\times M}{q \times N \times A}$ given in equation (3-8)

Appendix D

COPYRIGHT FOR PREVIOUSLY PUBLISHED MATERIAL

Certain portions of text and graphics in this dissertation are also presented as already published journal articles, the copyright forms of which are given here.

D.1 MRS Advances copyright form pertaining to the article in ref. [59]:



The screenshot shows the Cambridge University Press website. The top navigation bar includes links for Academic, Cambridge English, Education, Bibles, Digital Products, and About Us. A search bar is located in the top right corner. Below the navigation bar, there is a secondary menu with links for Who We Are, What We Do, Rights & Permissions, Community & Environment, and Our. The main content area features a breadcrumb trail: Home / About Us / Rights & Permissions / Permissions / Permissions Requests From Our Authors. The title of the page is 'Permissions Requests From Our Authors'.

To re-use material from their works.

In certain circumstances, permissions requests are not required from authors who wish to re-use original material they have written for a Cambridge publication, provided that the subsequent use includes a full acknowledgement of the original publication, together with the copyright notice and the phrase 'Reprinted with permission'.

Permissions requests are waived if:

- The author of the work wishes to reproduce a single chapter (not exceeding 20 per cent of his/her work), journal article or shorter extract in a subsequent work (i.e. with a later publication date) of which he or she is to be the author, co-author or editor.
- The author wishes to photocopy a single chapter (not exceeding 20 per cent of his/her work as a whole), journal article or shorter extract for his/her own teaching.
- The author wishes to reproduce a book chapter or journal article on their personal website or other website in accordance with our Green Open Access and social sharing policies. Enquires can be sent to openaccess@cambridge.org.

D.2 ACS Sustainable Chemistry and Engineering Copyright form for the article in ref. [60]:



RightsLink®

Home

Create Account

Help



ACS Publications
Most Trusted. Most Cited. Most Read.

Title: Toward a Practical Solar-Driven CO₂ Flow Cell Electrolyzer: Design and Optimization
Author: Gowri M. Sriramagiri, Nuha Ahmed, Wesley Luc, et al
Publication: ACS Sustainable Chemistry & Engineering
Publisher: American Chemical Society
Date: Nov 1, 2017

Copyright © 2017, American Chemical Society

LOGIN

If you're a [copyright.com](#) user, you can login to RightsLink using your [copyright.com](#) credentials. Already a RightsLink user or want to [learn more?](#)

PERMISSION/LICENSE IS GRANTED FOR YOUR ORDER AT NO CHARGE

This type of permission/license, instead of the standard Terms & Conditions, is sent to you because no fee is being charged for your order. Please note the following:

- Permission is granted for your request in both print and electronic formats, and translations.
- If figures and/or tables were requested, they may be adapted or used in part.
- Please print this page for your records and send a copy of it to your publisher/graduate school.
- Appropriate credit for the requested material should be given as follows: "Reprinted (adapted) with permission from (COMPLETE REFERENCE CITATION). Copyright (YEAR) American Chemical Society." Insert appropriate information in place of the capitalized words.
- One-time permission is granted only for the use specified in your request. No additional uses are granted (such as derivative works or other editions). For any other uses, please submit a new request.

D.3 Sustainable Energy and Fuels permissions note pertaining to article in ref. [61]:

Contents of Chapters 3 and 4 were published in the journal of *Sustainable Energy and Fuels*, the copyright to which is given below.

Computation and assessment of solar electrolyzer field performance: comparing coupling strategies

Gowri M. Sriramagiri, W. Luc, F. Jiao, K. Ayers, K. D. Dobson and S. S. Hegedus, *Sustainable Energy Fuels*, 2018, Advance Article, DOI: 10.1039/C8SE00399H

If you are not the author of this article and you wish to reproduce material from it in a third party non-RSC publication you must [formally request permission](#) using Copyright Clearance Center. Go to our [Instructions for using Copyright Clearance Center page](#) for details.

Authors contributing to RSC publications (journal articles, books or book chapters) do not need to formally request permission to reproduce material contained in this article provided that the correct acknowledgement is given with the reproduced material.

Reproduced material should be attributed as follows:

- For reproduction of material from NJC:
Reproduced from Ref. XX with permission from the Centre National de la Recherche Scientifique (CNRS) and The Royal Society of Chemistry.
- For reproduction of material from PCCP:
Reproduced from Ref. XX with permission from the PCCP Owner Societies.
- For reproduction of material from PPS:
Reproduced from Ref. XX with permission from the European Society for Photobiology, the European Photochemistry Association, and The Royal Society of Chemistry.
- For reproduction of material from all other RSC journals and books:
Reproduced from Ref. XX with permission from The Royal Society of Chemistry.